Metabolic Imaging of Pediatric Brain Tumors Using High-Field MRI

^{31}P-Magnetic Resonance Spectroscopy

TM30004: Master Thesis

Hilde Roording

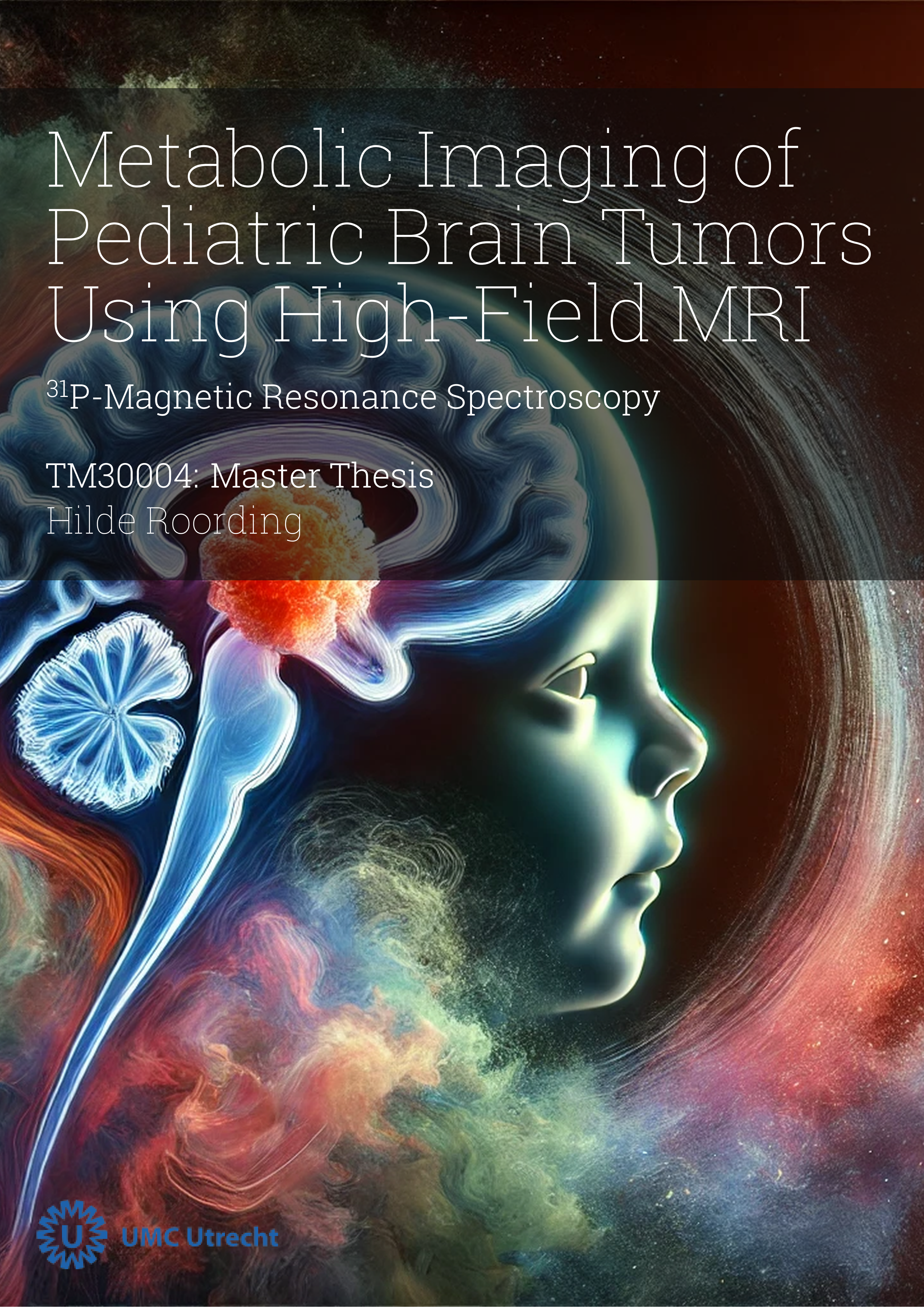

UMC Utrecht

Metabolic Imaging of Pediatric Brain Tumors Using High-Field MRI

^{31}P-Magnetic Resonance Spectroscopy

by

Hilde Roording
Student number: 4827821
03-03-2025

Thesis in partial fulfilment of the requirements for the joint degree of Master of Science in

Technical Medicine

Leiden University   Delft University of Technology   Erasmus University Rotterdam

Master thesis project (TM30004 ; 35 ECTS)
Dept. of Biomechanical Engineering, TUDELFT
26-08-2024 TM30004 – 21-03-2025 TM30004

Supervised by
dr.ir. J.P. Wijnen
MD. dr. W.P. Nieuwenhuis
dr. ir. C.F. Najac
dr.ir. E.C. Wiegers

Thesis committee members:
Dr. J. Veenland (Chair)
dr.ir. J.P. Wijnen
MD. dr. W.P. Nieuwenhuis
dr. ir. C.F. Najac

Preface

I would like to take this opportunity to express my gratitude to everyone who has contributed to the completion of this master's thesis and supported me throughout this project.

This thesis represents my research on metabolic imaging in pediatric brain tumors, a topic that has both challenged and inspired me. Conducting this research has allowed me to merge technical knowledge with clinical applications. From data analysis to patient-centered perspectives, I have gained a deeper appreciation for the complexities of pediatric neuro-oncology and the evolving role of non-invasive imaging in improving patient care. Working with children facing serious illness has shaped my perspective, reminding me of the real impact of medical research and the importance of advancing non-invasive imaging techniques.

I would like to express my gratitude to my supervisors and colleagues for their invaluable guidance and encouragement. Jannie and Chloe, I am incredibly grateful for the time you dedicated to me despite your busy schedules, always finding a moment to meet with me, answer my emails, ask insightful critical questions, and patiently explain concepts multiple times when needed. Evita, I appreciate your support after returning from your paternity leave, always making time for my questions. Wouter, thank you for providing a medical perspective that enriched my understanding of the clinical application.

I would also like to thank the High-Field MRI group for their warm welcome and for creating a stimulating environment that encouraged learning, curiosity, and collaboration. I am grateful to my fellow students for the enjoyable coffee breaks and post-lunch games.

Additionally, I want to extend my gratitude to the Princess Máxima Center and Sabine for introducing me to the world of pediatric oncology and deepening my understanding of the challenges these children and their families face daily.

Finally, I am deeply grateful to my family and friends for their unwavering support, patience, and belief in me throughout this journey. Your encouragement from the very first day has meant the world to me.

I hope this thesis contributes to the ongoing efforts to refine metabolic imaging and inspires further research in this field.

Hilde Roording
March 2025

Summary

Introduction
Pediatric brain tumors are the most common solid tumors in children and a leading cause of cancer-related mortality. Magnetic resonance imaging (MRI) is the primary tool for assessing tumor progression and treatment response. However, distinguishing treatment effects from tumor progression remains a challenge, complicating clinical decision-making. Phosphorus-31 Magnetic Resonance Spectroscopic Imaging (^{31}P-MRSI) is a non-invasive technique that provides spatially resolved metabolic information by detecting phosphorus-containing metabolites, such as phosphocreatine (PCr), adenosine triphosphate (ATP), and phosphomonoesters (PME). These metabolites offer insights into energy metabolism, cell membrane turnover, and intracellular pH regulation, which could help differentiate tumor progression from treatment-related changes. A major challenge in ^{31}P-MRSI is its low signal-to-noise ratio (SNR), due to the relatively low gyromagnetic ratio and the low concentration of phosphorus metabolites in tissues. This necessitates large voxel sizes, leading to partial volume effects, where a voxel contains signals from multiple tissue types (e.g., tumor and normal-appearing white matter (NAWM)). To address this, post-processing regridding techniques can be applied to recalculate the spatial position of the ^{31}P-MRSI signal and improve grid alignment with anatomical structures.

Aim
This study investigates post-processing regridding techniques to optimize spatial localization in ^{31}P-MRSI and evaluates longitudinal metabolic changes in pediatric brain tumors and NAWM.

Methods
Phantom and in vivo clinical data were acquired using a 7T MRI scanner. In the phantom experiment, a spherical phantom with inorganic phosphate (Pi) was scanned with different MRSI grid configurations. Two post-processing regridding techniques were evaluated by comparing regridded data to a reference: 1) K-space phase adjustment, which applies a phase shift before Fourier transformation, and 2) Interpolation-based regridding, which estimates spectral data at shifted voxel positions. Correlation analysis was performed with Pearsons correlation. Following phantom validation, the best-performing regridding technique was applied to in vivo pediatric brain tumor data. The impact of regridding was assessed by analyzing metabolic ratio changes (PE/GPE, PCr/γATP, pH, Pi/ATP) in tumors and NAWM, alongside spectral quality metrics such as SNR and linewidth. Additionally, longitudinal data from eight pediatric patients with low-grade glioma were analyzed to assess metabolic ratio changes over time. Patients underwent different chemotherapy regimens, enabling an evaluation of therapy-related metabolic alterations.

Results
K-space phase adjustment performed superior compared to the spatial interpolation, evidenced by higher correlations and more accurate peak intensities in voxels near the Pi bead. In in vivo data, regridding improved voxel alignment with tumor regions, increasing tumor contribution within individual voxels. Spectral quality (SNR and linewidth) remained stable after regridding, and metabolic ratios were not significantly altered. Longitudinal analysis revealed metabolic changes in tumors and NAWM over time. However, normalizing tumor metabolic ratios to NAWM did not produce consistent trends across patients.

Conclusion
Regridding enhances spatial localization in ^{31}P-MRSI without degrading spectral quality, making it a viable post-processing approach. While metabolic alterations in tumors and NAWM were observed, they did not reach statistical significance. Further validation in larger cohorts is required to assess the clinical significance of these metabolic changes.

Contents

Nomenclature

Abbreviations

Abbreviation	Definition
1H	Proton (Hydrogen-1)
31P	Phosphorus-31
ADP	Adenosine Diphosphate
AP	Anterior–Posterior
APT-CEST	Amide Proton Transfer Chemical Exchange Saturation Transfer
ATP	Adenosine Triphosphate
BL	Baseline
CSI	Chemical Shift Imaging
Cr	Creatine
DLGNT	Diffuse Leptomeningeal Glioneuronal Tumor
DPG	Diphosphoglycerate
DWI	Diffusion-Weighted Imaging
FID	Free Induction Decay
FOV	Field of View
FWHM	Full Width at Half Maximum
FU1	Follow-Up 1
FU2	Follow-Up 2
GPC	Glycerophosphocholine
GPE	Glycerophosphoethanolamine
LGG	Low-Grade Glioma
LR	Left–Right
MITCH	Metabolic Imaging of Tumors in Children
MRSI	Magnetic Resonance Spectroscopic Imaging
NAWM	Normal-Appearing White Matter
NADH	Nicotinamide Adenine Dinucleotide
NSA	Number of Single Averages
PC	Phosphocholine
PCr	Phosphocreatine
PE	Phosphoethanolamine
Pi	Inorganic Phosphate
PME	Phosphomonoesters
PDE	Phosphodiesters
ppm	Parts Per Million
PSF	Point Spread Function
RAPNO	Response Assessment in Pediatric Neuro-Oncology
RF	Radiofrequency
RL	Right–Left
ROI	Region of Interest
SNR	Signal-to-Noise Ratio
TE	Echo Time
TR	Repetition Time
UDPG	Uridine Diphosphoglucose
VOI	Volume of Interest

1 Introduction

An introduction to the clinical background of this research

1.1. Pediatric brain tumors

Brain cancer is the most prevalent solid cancer in children and one of the leading causes of cancer-related death in both children and adults worldwide [1, 2]. Brain tumors vary widely in terms of morbidity and mortality depending on the type, size, location, and rate of tumor growth. For example, pilocytic astrocytoma, a low-grade glioma, has a 10-year survival rate exceeding 95% [1], whereas diffuse midline glioma has a very poor prognosis, with only 10% of the patients surviving beyond two years [3]. Despite advances in diagnosis and treatment, including surgery, radiation therapy, and chemotherapy, brain tumors remain a major clinical challenge [4, 5].

Pediatric brain tumors differ from adult tumors in terms of histopathology, tumor location, and genetic alterations, influencing treatment strategies and prognosis [1]. Given these differences, research on pediatric brain tumors is essential to improve diagnosis and treatment strategies tailored to this population. The most common malignant pediatric brain tumors include gliomas, embryonal tumors, and germ-cell tumors [1]. Symptoms vary based on the tumor location; for instance, cortical tumors may cause seizures, optic pathway tumors can impair vision. Other common symptoms include nausea, headache, ataxia, and hemiparesis [6].

The gold standard for diagnosing tumors is magnetic resonance imaging (MRI) in combination with histopathology [7]. Complete surgical resection offers the best prognosis, but is often infeasible due to the location and invasive nature, necessitating adjuvant chemotherapy and/or radiotherapy [4]. Regular MRI scans are essential to monitor treatment response and disease progression [7].

1.2. MRI assessment

A diagnostic brain MRI typically includes a T1-weighted scan for anatomical assessment; a T2-weighted scan to evaluate the ventricular system, subdural spaces, and edema; a FLAIR sequence to detect white-matter tumor involvement and edema; and diffusion-weighted imaging (DWI) to assess tumor cellularity and cytotoxic edema [8, 9]. In addition, post-contrast T1-weighted images are used to evaluate vascularity and blood-brain barrier disruption [10]. These conventional MRI sequences also provide an initial assessment of tumor composition, such as the identification of cystic components, calcifications, hemorrhagic products, fibrin deposits, or melanin accumulation [9].

The response to therapy for pediatric patients can be evaluated in studies using the response assessment in pediatric neuro-oncology (RAPNO). It evaluates the response of tumors according to different criteria such as the size of the lesion, contrast enhancement pattern, new lesions, and clinical parameters [11, 12]. However, these criteria may be inconclusive in distinguishing true tumor progression from pseudoprogression, which is a therapy-induced contrast-enhanced T2 and/or FLAIR hyperintense region that mimics progression [13, 14, 15, 16]. Tumor progression may require modification of treatment, while pseudoprogression is a sign of response to treatment. Thus, accurately differentiating the effects of treatment from the effects of progression is critical to ensure timely treatment adjustments and prevent unnecessary therapeutic escalation. From a diagnostic perspective, we lack a tool that can non-invasively identify tumor activity and indicate the aggressiveness of that part of the tumor.

Advanced metabolic imaging techniques are evolving rapidly and are increasingly helpful in understanding tumor biology, tumor characterization, guiding treatment, and predicting patient outcomes, thereby facilitating more personalized care in cancer treatment [17, 18]. Key methods include ^{1}H and ^{31}P magnetic resonance spectroscopic imaging (MRSI) of various metabolites, chemical exchange-dependent saturation transfer (CEST), and positron emission tomography (PET) [17]. While the MRI techniques are noninvasive, PET requires the administration of radioactive tracers that expose patients to ionizing radiation. In clinical practice, ^{1}H-MRSI has been widely employed [19, 20], whereas ^{31}P-MRSI is less commonly applied but offers novel insights into phospholipid and energy metabolism, particularly at higher magnetic field strengths where enhanced spectral resolution and improved signal-to-noise ratio further augment metabolite detection [21, 22]. Each modality, therefore, presents unique advantages and limitations regarding sensitivity, spatial resolution, metabolic specificity, and clinical feasibility.

1.3. Aim

This study aims to address key challenges in ^{31}P-MRSI at 7T, focusing on the validation of post-processing techniques for realigning the spectral grid of ^{31}P-MRSI and analyzing in vivo spectra of pediatric patients with brain tumors. By evaluating the accuracy and impact of these realignment techniques, this study seeks to optimize spatial localization, reduce partial volume effects, and ultimately enhance ^{31}P-MRSI for metabolic imaging applications.

2

^{31}P-MRSI Background

An introduction to the technical background of this research

2.1. MRI in general

MRI is an imaging technique that uses a strong static magnetic field,time-varying gradient fields, and radiofrequency (RF) pulses to generate high-resolution images of tissues and organs. Conventional MRI primarily exploits the magnetic properties of hydrogen nuclei (^{1}H), which are abundant in water and fat molecules [23]. Each nucleus has a unique gyromagnetic ratio γ, representing the ratio of its magnetic moment to its angular momentum. When placed in a static magnetic field (B_0), nuclei align with the magnetic field and resonate at a specific frequency known as the Larmor frequency f, equation 2.1.

$$f = \gamma B_0 \tag{2.1}$$

The application of an RF pulse at this resonance frequency temporarily disrupts the alignment, causing protons to displace their magnetization from equilibrium. As the nuclei return to equilibrium, they emit signals characterized by two relaxation processes: T_1 (spin-lattice) and T_2 (spin-spin). Tissue contrast in MRI arises from differences in these relaxation properties (T1 and T2 relaxation time) [23].

Spatial encoding is achieved through gradient fields, which introduce frequency and phase variations across the imaging volume. The acquired signals are sampled in k-space, which is a frequency-domain representation of the MRI signal, and reconstructed into spatial images using an inverse Fourier transform, enabling MRI to provide detailed soft tissue contrast [23].

2.2. Phosphorus magnetic resonance imaging

Although MRI predominantly relies on ^{1}H due to its high natural abundance and strong signal intensity, other nuclei, such as phosphorus-31 (^{31}P), can also be studied using MR techniques [21]. Nuclei resonating at higher frequencies generate stronger signals. At 7T, ^{1}H resonates at approximately 300 MHz, whereas ^{31}P resonates at around 121 MHz, making detection of ^{31}P challenging. However, this sensitivity limitation can be partially mitigated by higher magnetic field strengths, which enhance signal intensity and improve spectral resolution. To acquire ^{31}P signals, an RF pulse must be applied at its specific resonance frequency [21]. Additionally, since standard MRI coils are optimized for ^{1}H, a dedicated ^{31}P receive coil is required for efficient signal detection.

However, the exact resonance frequency of a nucleus is not solely determined by B_0; it also depends on its local electronic environment, an effect known as the chemical shift. This phenomenon arises from electron shielding, where surrounding electron clouds generate an opposing magnetic field (B_e), reducing the local field strength ($B_n = B_0 - B_e$). The extent of this shielding depends on the electronegativity of nearby atoms, leading to small variations in resonance frequency [21]. As a result, different ^{31}P-containing molecular groups, even within the same molecule, can exhibit distinct resonance frequencies.

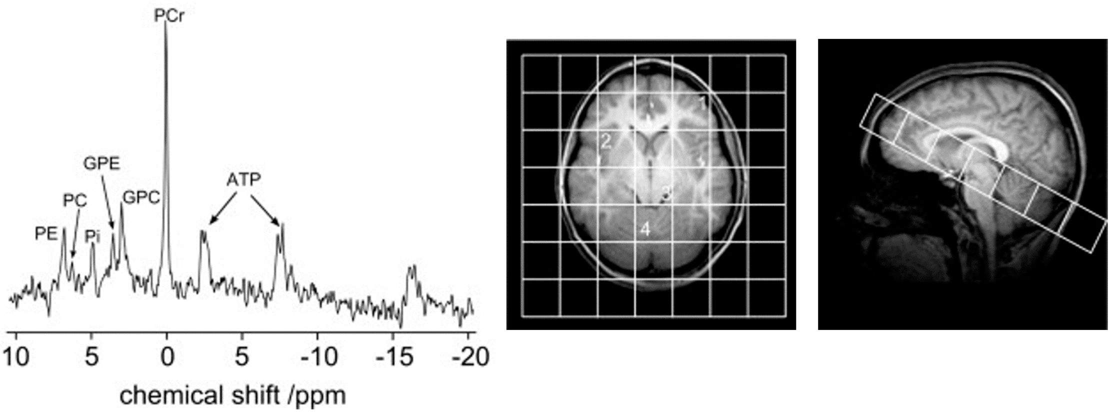

Figure 2.1: ^{31}P-MRSI spectrum obtained from a healthy volunteer. The orientation of the grid is shown on the right. The orientation of the MRSI grid allowed simultaneous metabolic profiling of various regions of the brain [25].

In ^{31}P magnetic resonance spectroscopic imaging (MRSI), this effect allows differentiation of phosphorus-containing metabolites based on their distinct chemical environments [21]. Key metabolites such as phosphocreatine (PCr), adenosine triphosphate (ATP), and inorganic phosphate (Pi) exhibit characteristic chemical shifts, enabling their quantification [24]. Chemical shifts are typically expressed in parts per million (ppm) relative to a reference compound, such as PCr (0.00 ppm) in muscle or brain spectroscopy, an example spectrum is visualized in Figure 2.1. This ppm scale normalizes the resonance frequency differences across different magnetic field strengths, ensuring consistent metabolite identification [21].

2.3. Phosphorus in the human body

Phosphorus plays a central role in cellular function, serving as a key component of energy metabolism, intracellular signaling, and structural integrity.

2.3.1. Cellular energetic state

Phosphorus is essential for maintaining cellular energy homeostasis through ATP and PCr [26, 27, 28, 29]. These molecules enable rapid ATP regeneration to meet fluctuating energy demands (Figure 2.2), particularly in high-energy-consuming tissues such as muscle and brain. The reversible reaction between PCr and creatine (Cr), catalyzed by creatine kinase, facilitates ATP regeneration by transferring a phosphate group from PCr to adenosine diphosphate (ADP) to regenerate ATP (Equation 2.2) [30].

$$\mathrm{ATP} + \mathrm{Cr} \rightleftharpoons \mathrm{PCr} + \mathrm{ADP} \tag{2.2}$$

Dysregulated ATP metabolism can disrupt the cellular energy balance, which is particularly relevant in disease conditions such as cancer. The Pi/ATP ratio is used as an indicator of ATP turnover, while the PCr/ATP ratio reflects the overall energetic state of a tissue [31]. Furthermore, the PCr/Pi ratio represents oxidative capacity [32, 33], and the Pi/ATP ratio provides insight into the dynamics of ATP turnover [33].

Beyond energy metabolism, phosphorus also contributes to pH regulation. Intracellular pH homeostasis is maintained through buffering systems and ATP-driven ion transport mechanisms, with inorganic phosphate (Pi) acting as a key regulator [34]. Alterations in pH influence enzyme activity, cell proliferation, and metabolic function [35, 34].

2.3.2. Phospholipid Metabolism

Phosphorus plays a fundamental role in cell membrane integrity, forming the backbone of phospholipids such as phosphatidylcholine (PC) and phosphatidylethanolamine (PE). In ^{31}P-MRSI, phospho-

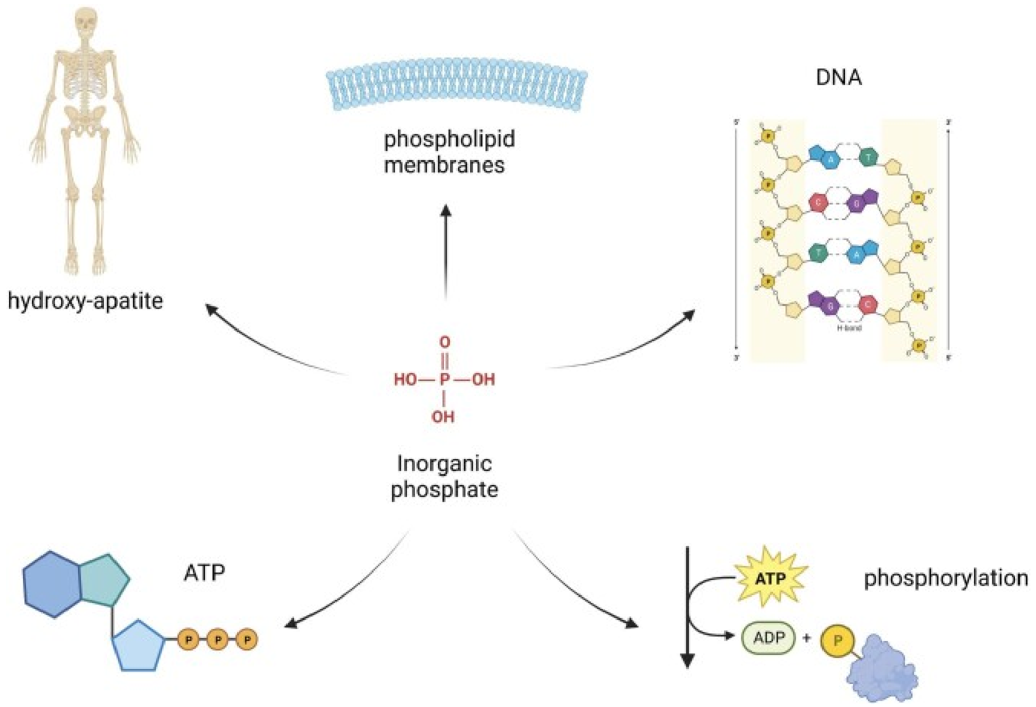

Figure 2.2: Functions of phosphate inside the human body. Inorganic phosphate is a building block for phospholipids in biological membranes, for nucleotides in DNA and RNAs, to form ATP, is involved in intracellular signaling events, and is critical for the stability of bone under the form of hydroxyapatite [26].

monoesters (PME), including PE and PC, serve as markers in phospholipid biosynthesis. Their breakdown products, phosphodiesters (PDEs), such as glycerophosphoethanolamine (GPE) and glycerophosphocholine (GPC), reflect membrane degradation and turnover [36].

2.3.3. Brain tumors

Alterations in phosphorus metabolism reflect high metabolic demands, rapid proliferation, and adaptation to hypoxic conditions characteristic of malignant brain tumors [35, 37, 36]. These metabolic disruptions, including dysregulated energy metabolism, pH imbalance, and abnormal phospholipid turnover, drive tumor growth and aggressiveness [35, 34]. Non-invasive metabolic imaging techniques, such as ^{31}P-MRSI, provide a unique opportunity to assess these alterations in vivo. By quantifying phosphorus-containing metabolites, ^{31}P-MRSI enables the evaluation of tumor bioenergetics (PCr/ATP, Pi/ATP), hypoxia-related acidosis (intracellular pH), and membrane turnover (PME/PDE, PE/GPE), offering insight into tumor physiology beyond conventional imaging.

From the literature review on metabolic imaging in response to therapy (Appendix A), key phosphorus-containing metabolic markers relevant to brain tumors include:

- Cellular energetic state: PCr, PCr/ATP, PCr/Pi, PDE/ATP
- ATP turnover: Pi/ATP
- Hypoxia markers: pH
- Cell membrane metabolism: PME/PDE, PE/GPE, PME/PCr, GPE

These markers have been used to assess treatment response in glioblastoma patients receiving bevacizumab and temozolomide, with reductions in hypoxia markers and improved energy metabolism observed post-therapy [35, 38].

2.4. ^{31}P-MRSI challenges

Despite the promising potential of ^{31}P-MRSI in brain cancer, its clinical application remains limited by the variability in study designs and inconsistent findings across different studies.

A challenge with ^{31}P MRSI is the inherently low signal-to-noise ratio resulting from the relatively low gyromagnetic ratio and the low concentration of phosphorus-containing metabolites. This necessitates large voxel sizes that may introduce partial volume effects where tissue boundaries, such as those around tumors, span multiple voxels, Figure 2.3 [39, 22]. This leads to a mixture of metabolic signals from the tumor and adjacent normal tissue [40].

Reducing voxel size improves spatial resolution thus minimizing the partial volume effect, but it requires increased field strength or prolonged acquisition times. As an alternative, post-processing techniques, such as k-space phase correction and interpolation-based regridding, can mitigate these effects [41].

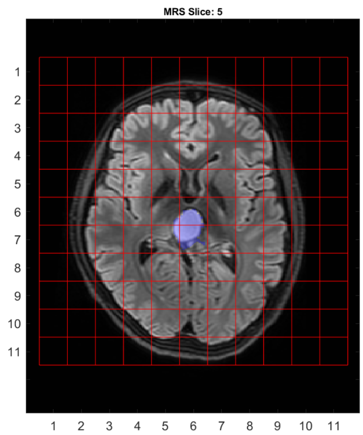

Figure 2.3: Pediatric brain MRI showing a tumor (purple) and a ^{31}P-MRSI grid (red). The tumor spans two voxels, leading to a partial volume effect where each voxel contains signals from both tumor and normal brain tissue.

3

Experiment

3.1. Introduction

Post processing methods can be used to recalculate ^{31}P-MRSI data A challenge with ^{31}P-MRSI is the inherently low signal-to-noise ratio due to a relatively low gyromagnetic ratio, and a low concentration of phosphorus-containing metabolites in tissues necessitating large voxel sizes [39]. These larger voxel sizes may introduce a partial volume effect where tissue boundaries, such as those around tumors, span across multiple voxels, leading to a mixture of metabolic signals from tumor and adjacent normal tissues [42]. To address this, post-processing methods can help to realign the MRSI grid to align more precisely with tissue structures. Here we evaluate two methods to recalculate the spatial position of the MRSI signal (1) k-space domain based phase adjustment, and (2) spatial domain based spectral interpolation in a phantom model.

Aim

This experiment examines two post-processing regridding methods —k-space-based using phase-encoding adjustment and spatial-based using linear interpolation— to reduce partial volume effects in ^{31}P-MRSI.

3.2. Methods

Phantom experiments were performed on a 7 Tesla MRI scanner (Achieva, Philips Healthcare, The Netherlands) to assess two post-processing techniques for regridding. The scan parameters are provided in Table 3.1. A spherical phantom containing a bead with 200 mM inorganic phosphate (Pi) was used. Seven datasets were acquired, two references with different resolutions, and five datasets where the grid was repositioned at a shifted location compared to the reference:

1. **Reference**:

Table 3.1: Scan parameters for a phantom experiment to assess two regridding techniques with FID=Free Induction Decay, MRSI=Magnetic Resonance Spectroscopic Imaging, TR= Repetition Time, TE=Echo Time, NSA=Number of Single Averages

Scan Parameters	Image Sequence	Coil	Acquisition pattern	TR	TE	Flip angle	Matrix size	Voxel size	NSA
Normal resolution	3D-FID-MRSI sequence	Custom quadrature TxRx 1H/31P head coil	Hamming-weighted k-space acquisition	100 ms	0.42 ms	11.4°	11x11x9	20x20 x20mm^3	28
Higher resolution	3D-FID-MRSI sequence	Custom quadrature TxRx 1H/31P head coil	Hamming-weighted k-space acquisition	100 ms	0.42 ms	11.4°	12x9x12	10x10x 10mm^3	20

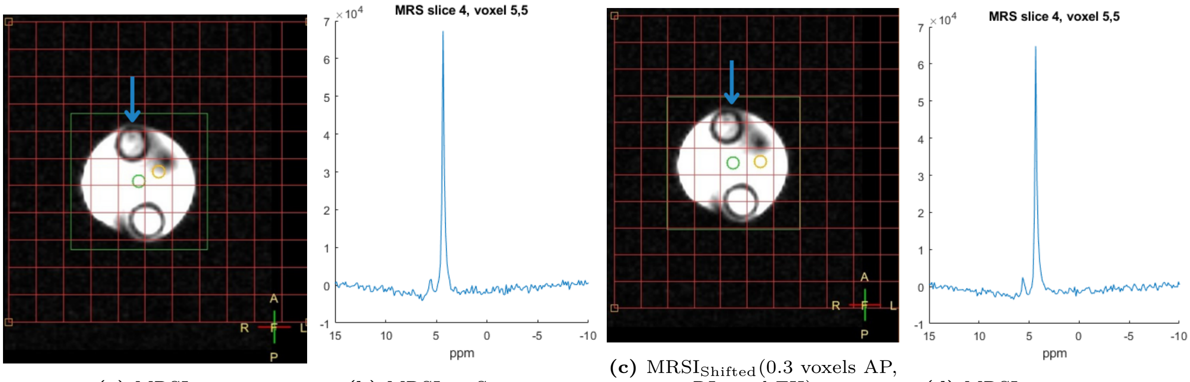

(a) $\mathrm{MRSI_{ref}}$ **(b)** $\mathrm{MRSI_{Ref}}$ Spectrum **(c)** $\mathrm{MRSI_{Shifted}}$(0.3 voxels AP, RL, and FH) **(d)** $\mathrm{MRSI_{Shifted}}$ spectrum

Figure 3.1: Phantom with the inorganic phosphate (Pi) bead, annotated with the arrow, and the MRSI grid superimposed for $\mathrm{MRSI_{Ref}}$ where the Pi bead is entered inside a voxel (A) and for (B) $\mathrm{MRSI_{Shifted}}$ where the grid is shifted 0.3 voxel in Anterior-Posterior (AP), Right-Left (RL), and Feet-Head (FH) directions. For both cases, the 31P spectrum of the MRSI voxel containing the Pi bead is displayed as well.

(a) **$\mathbf{MRSI_{Ref}}$**: The MRSI grid was positioned so that a voxel was centered on the Pi bead along the anterior-posterior (AP), left-right (LR) and feet-head (FH) axes (Figure 3.1a) for two different resolutions: $20 \times 20 \times 20$ mm^3, and $10 \times 10 \times 10$ mm^3.

2. **Shifted Datasets**:

(a) **$\mathbf{MRSI_{Shifted}}$**: The MRSI grid from $\mathrm{MRSI_{Ref}}$ was shifted in the AP, LR, and/or FH directions, simulating misalignment (Figure 3.1c). Four different grid configurations were acquired for the low resolution: shift of 0.3 voxels (i.e., 6 mm) in the AP, RL, and FH directions, shift of 0.3 voxels (i.e. 6 mm) in the RL direction, shift of 0.1 voxels (i.e. 2 mm) in AP direction, shift of 0.5 voxels (i.e. 10 mm) in FH direction. One shifted grid configuration was acquired for the high resolution: shift of 0.3 voxels (i.e., 6 mm) in the AP, RL, and FH directions.

Two post-processing methods were implemented to recalculate the spatial position of the MRSI signal so that the positions of the voxel coincide more closely with the region of interest and applied to $\mathrm{MRSI_{Shifted}}$. The first method is based on the shift theorem [40]. A phase shift, $e^{-i\Delta rk}$ is applied to the k-space data, $f(k,t)$ in different directions (AP, RL and/or FH) prior to the Fourier transformation, $F(r,t)$ where Δr represents the spatial shift and k represents a spatial location in the grid (equation 3.1) [40].

$$F(r + \Delta r_{AP}, \Delta r_{RL}, \Delta r_{FH}, t) = FT\Big[f(k_{AP}, k_{RL}, k_{FH}, t)e^{i(\Delta rk_{AP}, \Delta rk_{RL}, \Delta rk_{FH})}\Big] \tag{3.1}$$

The second method is a linear interpolation of the spectral data in the spatial domain, equation 3.2. For this technique, frequency and phase alignment of the MRSI data across voxels was performed prior to interpolation. Linear interpolation is used to estimate the value of spectral data in a shifted location $(r + \Delta r, t)$ by taking a weighted average (equation 3.3, where f is the fractional shift) of a spectral data point (r,t) and its spatial neighbor.

$$F(r + \Delta r_{AP}, \Delta r_{RL}, \Delta r_{FH}, t) = \sum_{a=0}^{1}\sum_{b=0}^{1}\sum_{c=0}^{1} w_{abc} F(r_{i+a,j+b,k+c}, t) \tag{3.2}$$

$$w_{abc} = (1 - a + (-1)^a f_{AP})(1 - b + (-1)^b f_{RL})(1 - c + (-1)^c f_{FH}) \tag{3.3}$$

The recalculated MRSI datasets are referred to as $\mathrm{MRSI_{PhaseShift}}$ and $\mathrm{MRSI_{Interpolated}}$, respectively.

^{31}P-MRSI data were reconstructed using custom MATLAB software with the pipeline described in Appendix B. The Pi signal was fitted as a single Lorentzian line-shape peak with AMARES [43]. The fitted area under the curve (AUC) of the Pi peak of $\mathrm{MRSI_{Shifted}}$, $\mathrm{MRSI_{PhaseShift}}$, and $\mathrm{MRSI_{Interpolated}}$

Table 3.2: Correlation coefficients for ^{31}P-MRSI post-processing techniques—$MRSI_{phase\ shift}$ and $MRSI_{interpolated}$—are presented for conventional and high-resolution data. Four grid shift configurations were applied: a shift of 0.3 in the anterior–posterior (AP), right–left (RL), and feet–head (FH) directions, and individual shifts of 0.3 (RL), 0.1 (AP), and 0.5 (FH).

Correlation coefficient	0.3 AP, RL, FH	0.3 RL	0.1 AP	0.5 FH
$MRSI_{phase\ shift}$	0.960	0.960	0.963	0.960
$MRSI_{phase\ shift\ high\ resolution}$	0.915			
$MRSI_{Interpolated}$	0.939	0.957	0.958	0.954
$MRSI_{Interpolated\ high\ resolution}$	0.935			

was compared voxel-wise to the AUC of $MRSI_{Ref}$ with Pearson's correlation coefficient. The correlation coefficients were interpreted as follows[44]: <0.5 indicates a weak correlation, 0.5–0.7 moderate, 0.7–0.9 strong, and >0.9 excellent.

3.3. Results

Figure 3.2 (large voxel) and 3.3 (small voxel) display heatmaps for $MRSI_{ref}$ and the results after correcting $MRSI_{shifted}$, which was repositioned with 0.3 voxels in the AP, RL, and FH direction, (i.e., $MRSI_{PhaseShift}$ and $MRSI_{Interpolated}$). The heatmaps for all the different grid positions can be found in Appendix C. For all grid positions, phase adjustment in k-space ($MRSI_{PhaseShift}$) yielded values closer to $MRSI_{Ref}$ compared to spectral interpolation ($MRSI_{Interpolated}$). The correlation coefficients for the AUC between the shifted spectra and $MRSI_{Ref}$ can be found in Table 3.2, demonstrating an excellent correlation (>0.9) for both methods. However, k-space phase adjustment consistently yielded higher agreement with $MRSI_{Ref}$. The full width at half maximum (FWHM) of the shifted spectra was similar to $MRSI_{Ref}$.

3.4. Discussion

This study evaluated two post-processing MRSI-regridding methods —k-space domain based using phase-encoding adjustment and spatial domain based using linear interpolation —to address partial volume effects in ^{31}P-MRSI. Both techniques demonstrated strong correlations with the baseline; however, k-space phase adjustment performed better compared to spatial interpolation, evidenced by higher correlations and more accurate peak intensities in voxels near the Pi bead. The lower peak intensities at interpolation are probably due to signal averaging around the peak that diminishes peak height.

Alternatively, interpolation could have been applied to the AUC maps after peak fitting, rather than directly to the spectra, potentially yielding different results. Neither regridding technique achieved a perfect correlation of 1 with the baseline, which was not expected, as repeated ^{31}P acquisitions on the same scanner can exhibit measurement variability. In a previous study on the repeatability of ^{31}P-MRSI in the healthy brain at 7T, the covariance for Pi was 16.2% [45].

In the small-voxel image, both post-processing techniques resulted in higher AUC deviations from the reference compared to the large-voxel images. However, these images exhibited higher noise, which could have arisen due to differences in scan parameters such as the number of single averages.

Although the phantom experiment allowed for controlled comparisons between true and post-processed regridding, it may not fully reflect the complexity of in vivo tumor imaging, where heterogeneous tissue characteristics can impact spectral properties. In the future, the focus should be on implementing the k-space phase adjustment method in clinical data.

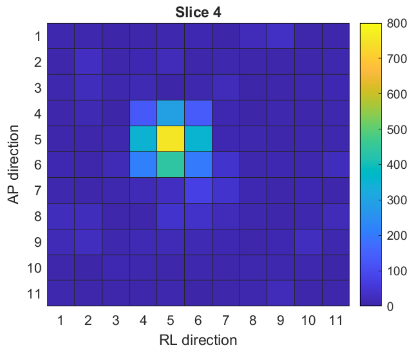

(a) $\mathrm{MRSI_{ref}}$

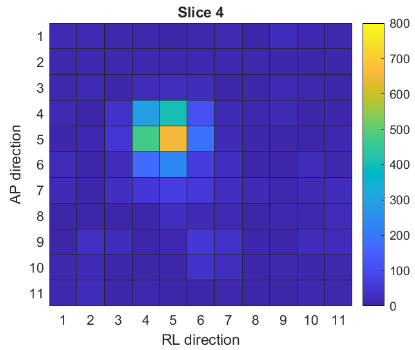

(b) $\mathrm{MRSI_{Shifted}}$

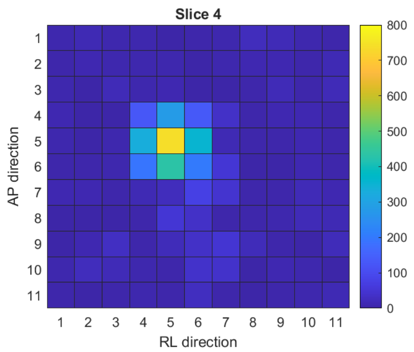

(c) $\mathrm{MRSI_{Phase\ Shift}}$ (-0.3 voxels AP, RL, and FH)

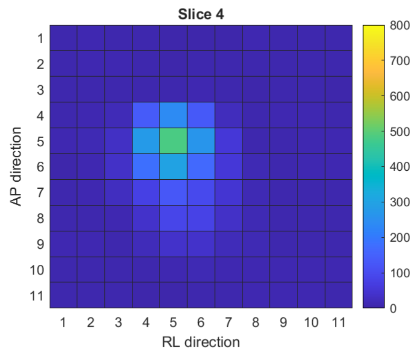

(d) $\mathrm{MRSI_{Interpolated}}$ (-0.3 voxels AP, RL, and FH)

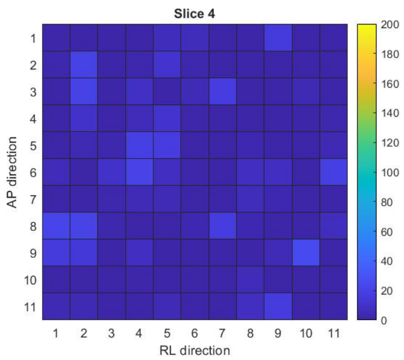

(e) $\mathrm{MRSI_{Ref}}$ - $\mathrm{MRSI_{PhaseShift}}$

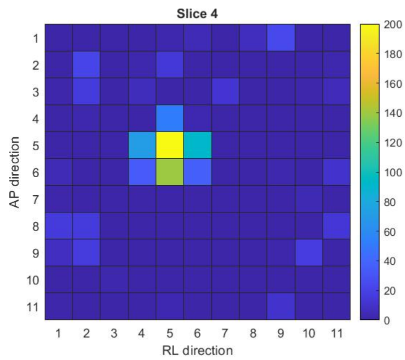

(f) $\mathrm{MRSI_{Ref}}$ - $\mathrm{MRSI_{Interpolated}}$

Figure 3.2: Heatmaps of the area under the curve (AUC) of the signal of inorganic phosphate (Pi) in the phantom experiment. Where (a) shows the AUC of $\mathrm{MRSI_{Ref}}$, (b) shows the AUC of $\mathrm{MRSI_{Shifted}}$, (c) shows the AUC of $\mathrm{MRSI_{Shifted}}$ after phase adjustment in k-space by -0.3 voxels in the Anterior-Posterior (AP), Right-Left (RL), and Feet-Head (FH) directions ($\mathrm{MRSI_{PhaseShift}}$), (d) shows the AUC of $\mathrm{MRSI_{Shifted}}$ after spatially based interpolation by -0.3 in AP, RL, and FH direction ($\mathrm{MRSI_{Interpolated}}$), (e) and (f) depict the differences between the shifted AUCs and the $\mathrm{MRSI_{Ref}}$ for k-space phase adjustment and spatial-based interpolation, respectively.

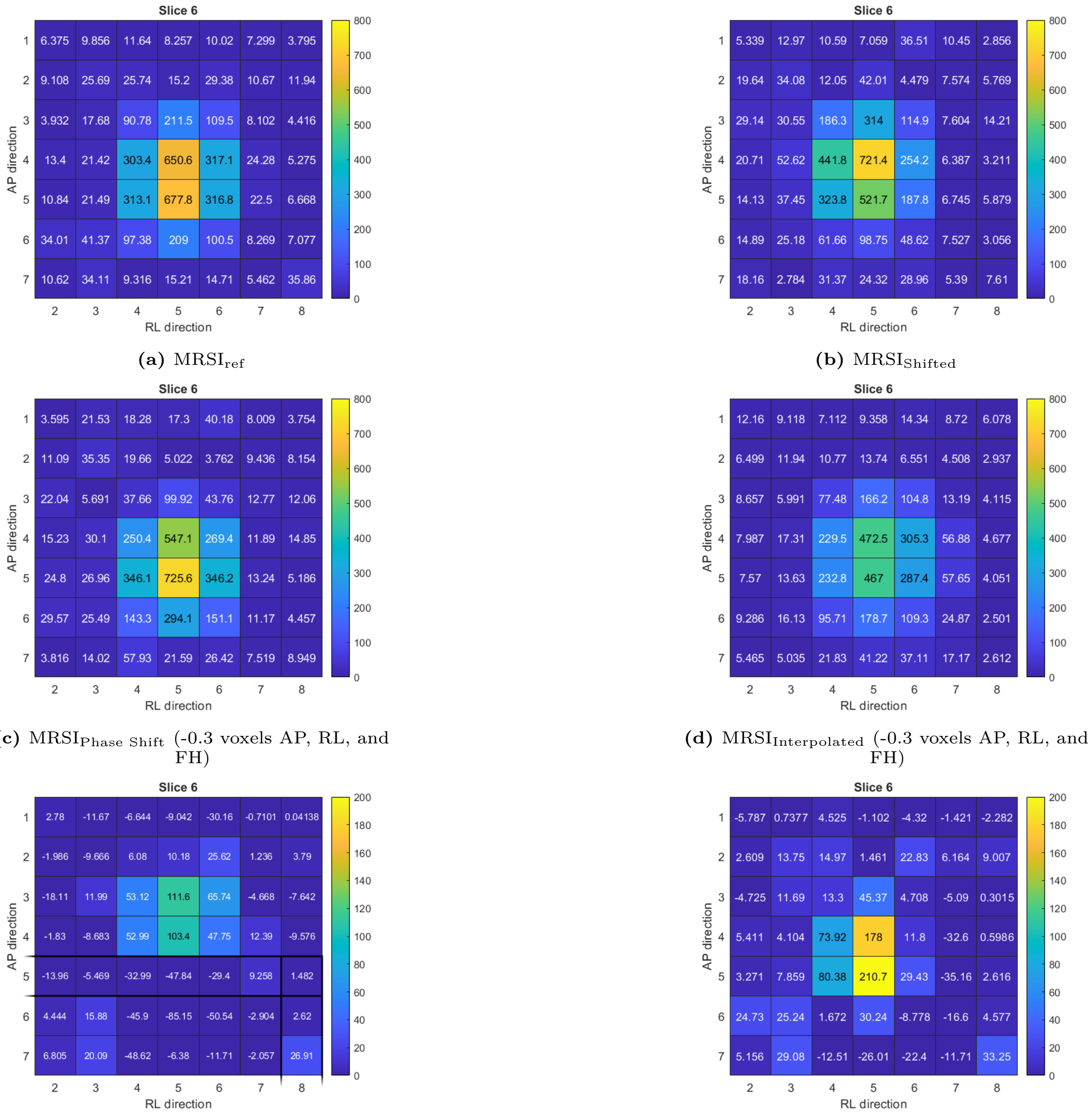

(a) $\mathrm{MRSI_{ref}}$

(b) $\mathrm{MRSI_{Shifted}}$

(c) $\mathrm{MRSI_{Phase\ Shift}}$ (-0.3 voxels AP, RL, and FH)

(d) $\mathrm{MRSI_{Interpolated}}$ (-0.3 voxels AP, RL, and FH)

(e) $\mathrm{MRSI_{Ref}}$ - $\mathrm{MRSI_{PhaseShift}}$

(f) $\mathrm{MRSI_{Ref}}$ - $\mathrm{MRSI_{Interpolated}}$

Figure 3.3: Heatmaps of the area under the curve (AUC) of the signal of inorganic phosphate (Pi) in the phantom experiment with the higher resolution voxels. Where (a) shows the AUC of $\mathrm{MRSI_{Ref}}$, (b) shows the AUC of $\mathrm{MRSI_{Shifted}}$, (c) shows the AUC of $\mathrm{MRSI_{Shifted}}$ after phase adjustment in k-space by -0.3 voxels in the Anterior-Posterior (AP), Right-Left (RL), and Feet-Head (FH) directions ($\mathrm{MRSI_{PhaseShift}}$), (d) shows the AUC of $\mathrm{MRSI_{Shifted}}$ after spatially based interpolation by -0.3 in AP, RL, and FH direction ($\mathrm{MRSI_{Interpolated}}$), (e) and (f) depict the differences between the shifted AUCs and the $\mathrm{MRSI_{Ref}}$ for k-space phase adjustment and spatial-based interpolation, respectively.

4
Regridding in vivo

4.1. Introduction

As established in chapter 3, ^{31}P-MRSI data can be spatially shifted during post-processing by k-space phase adjustment [42]. Optimizing the spatial location of the grid can enhance tumor content within a voxel and reduce partial volume effects, thus improving the accuracy of metabolic analysis. However, this has not yet been evaluated in in-vivo data.

This study assesses k-space phase adjustment in vivo, using data from the Metabolic Imaging of Tumors in Children (MITCH) study. The MITCH study focuses on metabolic imaging of pediatric brain tumors using 7T MRI. Two different coils are used for metabolic imaging: a custom quadrature TxRx ^{1}H/^{31}P head coil, specifically designed to acquire ^{31}P-MRSI data, and a Multix Nova head coil, used to acquire amide proton transfer chemical exchange saturation transfer (APT-CEST), a high-resolution FLAIR, and a T1 image. The FLAIR and T1 images serve as an anatomical reference for tumor delineation. Due to patient repositioning between acquisitions, image registration is required to align the different datasets.

Previous projects established methods for registering the low-resolution anatomical ^{31}P-MRSI image with the FLAIR image. However, no method has been developed to quantitatively determine the spatial shift required to maximize tumor coverage within a voxel or to calculate the percentage of tumor inclusion before and after regridding.

4.2. Aim

This study aims to evaluate regridding in k-space in in-vivo scans by: 1) determining the optimal spatial shift to improve tumor alignment within a voxel, 2) quantifying the percentage of tumor inclusion within a voxel before and after regridding, 3) assessing the impact of voxel shifting on the spectrum and metabolic ratio measurements in tumors and NAWM.

4.3. Methods

Twelve registered FLAIR images and ^{31}P-MRSI datasets from the MITCH study were used for regridding and metabolite analysis. Data were acquired using a 7 Tesla MRI scanner (Achieva, Philips Healthcare, The Netherlands). The scan parameters are provided in Table 4.1. Tumors were delineated on FLAIR images by a pediatric neuroradiologist with over ten years of experience using ITK-SNAP (v4.0.1). A control region in normal-appearing white matter (NAWM) was defined superior to the lesion, at least 2 cm away from the tumor, in an area without observable pathology.

The FLAIR grid overlay was used to determine the new grid position in the axial and sagittal views using custom Matlab software R2021a [46]. The exact code can be found in Appendix D. The new grid position was calculated by manually selecting the center of the tumor in the FLAIR image at the voxel with the highest tumor content. The $Displacement_{AP,RL,FH}$ between the center of the tumor

Table 4.1: Scan parameters for the in-vivo protocol to acquire 31-Phosphorus Magnetic Resonance Spectroscopic Imaging (^{31}P-MRSI) data with FID=Free Induction Decay, TR= Repetition Time, TE=Echo Time, NSA=Number of Single Averages

Image Sequence	Coil	Acquisition pattern	TR	TE	Flip angle	Matrix size	Voxel size	NSA
3D-FID-MRSI sequence	Custom quadrature TxRx 1H/31P head coil	Hamming-weighted k-space acquisition	100 ms	0.42 ms	11.4°	11x11x9	20x20 x20mm^3	28

$TumorCenter$ and the center of the nearest MRSI voxel, $VoxelCenter$ was calculated for each direction Anterior-Posterior (AP), Right-Left (RL), and Feet-Head (FH) using equation 4.1.

$$Displacement_{AP,RL,FH} = \frac{(TumorCenter - VoxelCenter)_{AP,RL,FH}}{ResolutionMRSI_{AP,RL,FH}} \tag{4.1}$$

The displacement values were initially determined in the resolution of the FLAIR image and converted to the MRSI resolution. The selection process was iterated until a satisfactory tumor voxel alignment was achieved.

Spectral quality was assessed by the SNR, defined as signal amplitude of PCr divided by the standard deviation of the noise, full width at half maximum (FWHM) of the PCr peak, and the presence of artifacts. Spectra were exluded if the FWHM>25Hz, the SNR<10 or if there were large artifacts assessed by an expert.

^{31}P-MRSI data were and frequency corrected using custom MATLAB software, which fitted the PCr signal as a single Lorentzian peak with AMARES [43]. The spectrum was subsequently corrected with the fitted frequency and phase offset before performing a full AMARES fit for the following metabolites: PCr, ATP, nicotinamide adenine dinucleotide (NAD), GPC, GPE, PC, PE, inorganic phosphate (Pi), extracellular Pi (ePi), uridine di-phosphoglucose (UDPG), membrane phospholipids (MPL), and diphosphoglycerate (DPG).

The following metabolic ratios were calculated for analysis: PE/GPE (cell membrane metabolism), PCr/γATP (energetic state), pH (hypoxia), Pi/ATP (ATP turnover) [Appendix A]. A Wilcoxon signed rank test was performed to evaluate the significance between before and after regridding, with statistical significance set at $p<0.05$. A Pearson's correlation was performed to evaluate the correlation between metabolic change and the increase of tumor inside a voxel. The correlation coefficients were interpreted as follows[44]: <0.5 indicates a weak correlation, 0.5–0.7 moderate, 0.7–0.9 strong, and >0.9 excellent.

4.4. Results

One scan was excluded due to a low SNR (7.4) and excessive linewidth (46 Hz), leaving 11 scans for analysis. Before regridding, the average SNR was 56.78 ± 19.86, and the average linewidth was 9.62 ± 2.83 Hz. After regridding, the average SNR was 58.78 ± 19.41, and the average linewidth was 10.44 ± 4.39 Hz. Changes varied across scans, with SNR and linewidth either increasing, decreasing, or remaining unchanged depending on the scan.

Figure 4.1 presents an example of the initial and shifted grid positions for patient 891_{FU2}, along with the corresponding spectra for the tumor and NAWM voxels. The grid was shifted by 0.63 MRSI-voxel in the AP direction, -0.047 MRSI-voxel in the RL direction, and 0.34 MRSI-voxel in the FH direction. Table 4.4 summarizes the percentage of tumor inclusion within the voxel of interest before and after regridding. In all cases, regridding increased the tumor content within the voxel.

Figure 5.2 illustrates the metabolic ratios (PE/GPE, PCr/γATP, and Pi/ATP) before and after regridding. Although regridding caused some changes in metabolite ratios, none were statistically significant.

The changes in metabolic ratios are plotted against the change in tumor volume in Figure 4.2. The correlation between changes in metabolic ratios and tumor content within the voxel was weak for

PCr/ATP (0.18), Pi/ATP (0.56), and PE/GPE (0.36), and moderate for pH (0.64).

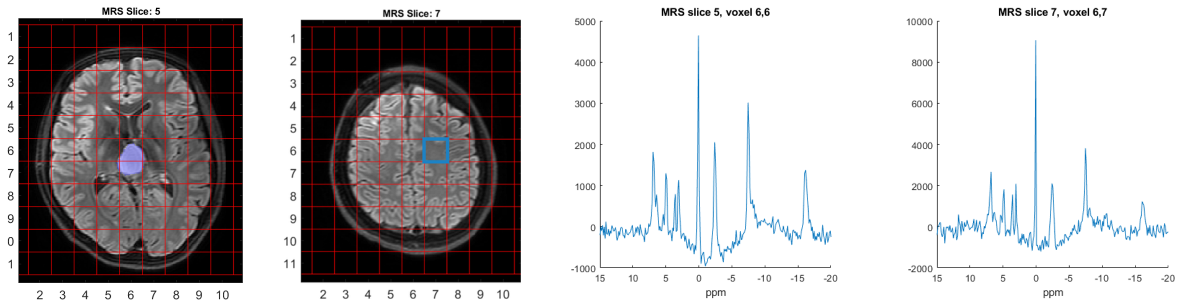

(a) Original grid position with in purple marked the tumor

(b) Original grid position with in blue marked NAWM

(c) Spectrum of slice 5, voxel 6,6 with most tumor present

(d) Spectrum of slice 7, voxel 6,7 with NAWM

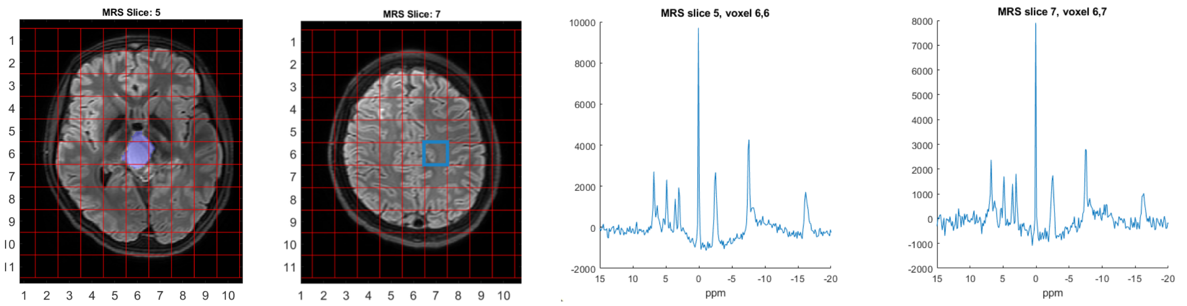

(e) Shifted grid position with in purple marked the tumor

(f) Shifted grid position with in the blue square marked NAWM

(g) Spectrum of slice 5, voxel 6,6 with most tumor present

(h) Spectrum of slice 7, voxel 6,7 with NAWM

Figure 4.1: Grid position over the brain and normal-appearing white matter (NAWM), along with the corresponding ^{31}P-MRSI spectra before (a–d) and after (e–h) regridding. The tumor is marked in purple, and NAWM is marked in blue. Panels (c) and (g) show the spectrum from slice 5, voxel (6,6), where the tumor is most present. Panels (d) and (h) show the spectrum from slice 7, voxel (6,7), representing NAWM.

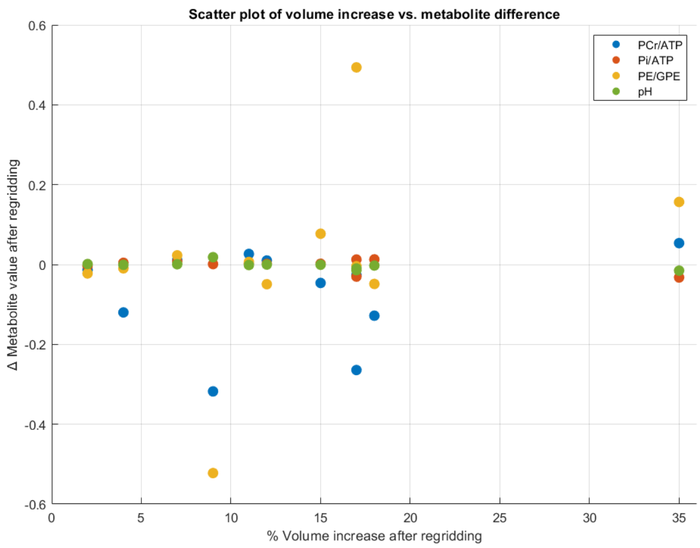

Figure 4.2: Scatter plot showing the relationship between tumor volume increase due to regridding (horizontal axis) and metabolic ratio changes after regridding (vertical axis) for phosphocreatine (PCr) to γ-adenosine triphosphate (ATP), inorganic phosphate (Pi) to ATP, phosphomonoesters (PE) to glycerophosphoethanolamine (GPE), and pH. No correlation is observed between the percentage increase in tumor volume and changes in metabolic ratios. Data points represent all patients at baseline, follow-up 1, and follow-up 2.

4.5. Discussion

A method was developed to reposition the grid to maximize tumor content within a voxel. This approach was applied to in vivo data, leading to changes in metabolic ratios (pH, PE/GPE, PCr/γATP, Pi/ATP) in both tumor and NAWM. Increasing the tumor fraction within the voxel aimed to minimize partial volume effects. However, these effects were not entirely eliminated, as the tumor often remained smaller than the voxel size.

In addition to partial volume effects, other confounding factors influence metabolic ratios and spectral quality. B0 inhomogeneities introduce local variations in resonance frequency. These can be mitigated by shimming, which optimizes magnetic field homogeneity, or by applying localized B0 correction during post-processing [21] Another factor is voxel bleeding, which results from the Fourier transformation properties described by the point spread function (PSF), leading to signal contamination from adjacent voxels [40]. Voxel bleeding can be eliminated using single-voxel spectroscopy or reduced by increasing phase encoding steps. K-space weighting and filtering (e.g., a Hamming filter already applied in this study) further minimize its impact [47].

Spectral quality, assessed by noise levels and linewidth, remained largely unchanged after regridding, suggesting no significant spectral degradation.

Metabolic changes before and after regridding showed a weak to moderate correlation with the increase in tumor volume in the voxel.

Chapter 3 demonstrated that k-space regridding is possible in phantom data. Although metabolic ratios changed in vivo, their clinical significance remains uncertain due to the small sample size (n=11) and the lack of ground truth for tumor and NAWM metabolite levels. This limitation underscores the challenge of confirming the accuracy of voxel-shifting approaches in patient scans.

Future research should focus on systematically comparing the evolution of tumor and NAWM metabolic ratios in pediatric patients. Monitoring these metabolic changes could provide valuable insights into tumor biology and behavior. Expanding the cohort size will be crucial to further evaluate these metabolic changes.

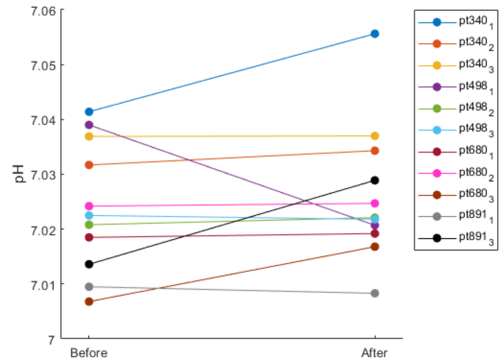

(a) pH in tumor before and after regridding, showing no significant differences (p=0.25)

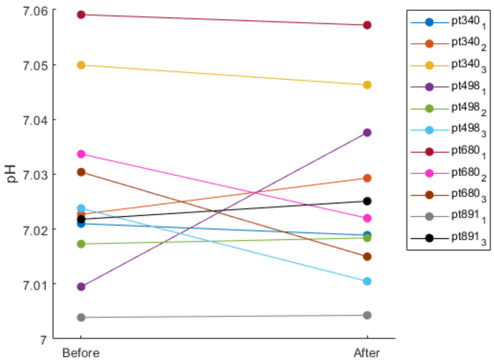

(b) pH in NAWM before and after regridding, showing no significant differences (p=0.53)

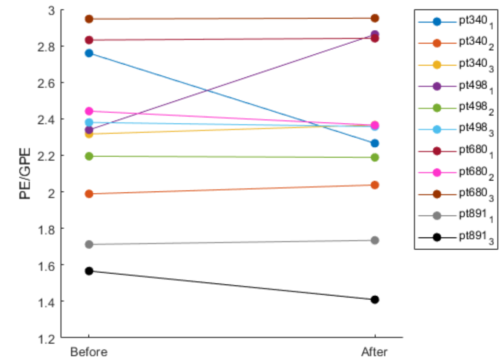

(c) PE/GPE in tumor before and after regridding, showing no significant differences (p=0.93)

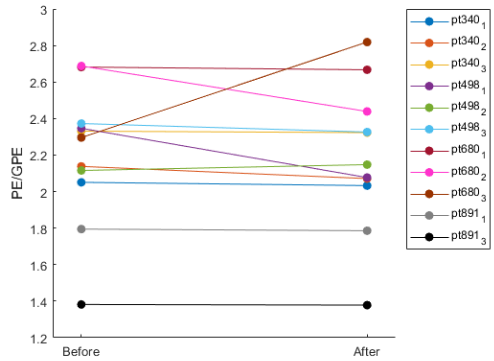

(d) PE/GPE in NAWM before and after regridding, showing no significant differences (p=0.16)

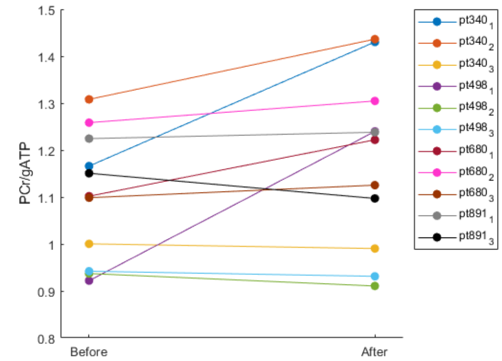

(e) PCr/γATP in tumor before and after regridding, showing no significant differences (p=0.09)

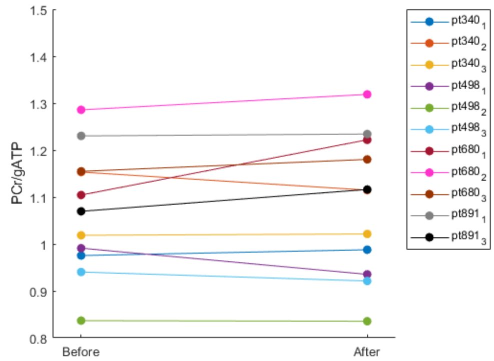

(f) PCr/γATP in NAWM before and after regridding, showing no significant differences (p=0.42)

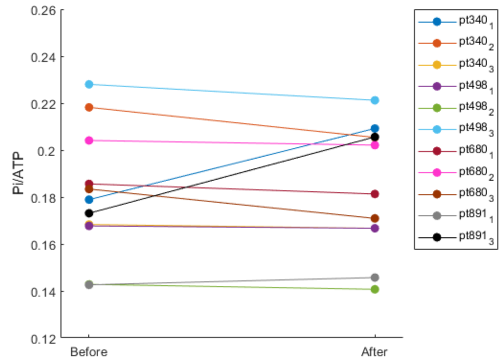

(g) Pi/ATP in tumor before and after regridding, showing no significant differences (p=0.53)

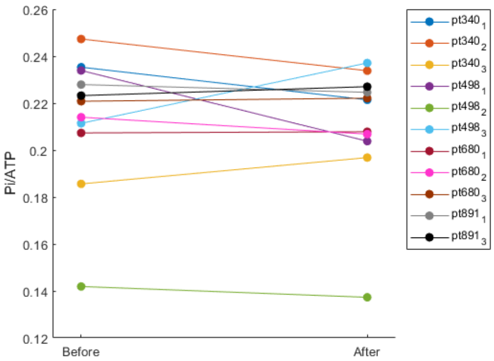

(h) Pi/ATP in NAWM before and after regridding, showing no significant differences (p=0.21)

Figure 4.3: Metabolic ratios in tumor and normal-appearing white matter (NAWM) before and after regridding. The analyzed ratios include pH, phosphomonoesters to glycerophosphoethanolamine (PE/GPE), phosphocreatine to γ-adenosine triphosphate (PCr/γATP), and inorganic phosphate to ATP (Pi/ATP). No significant differences were observed before and after regridding ($p > 0.05$).

5

31P MRSI in clinical setting

5.1. Introduction

As mentioned in Chapter 1, we lack a tool to non-invasively identify tumor activity. ^{31}P-MRSI provides metabolic insight by detecting phosphorus-containing compounds involved in energy metabolism and cell membrane turnover, which are often dysregulated in malignant tumors [35, 38]. Key metabolic markers in ^{31}P-MRSI, focus on PE/GPE as indicators of membrane turnover, PCr/ATP to assess energy homeostasis, Pi/ATP as a marker of ATP turnover, and intracellular pH to reflect tumor microenvironment acidity. These parameters provide crucial information about tumor metabolism.

5.2. Aim

This study aimed to evaluate ^{31}P-MRSI metabolic ratios in pediatric patients with low-grade glioma over multiple time points to assess treatment response or monitor tumor progression in cases managed with a wait-and-scan approach. By analyzing metabolic changes over time, we sought to assess potential biomarkers for tumor progression and treatment response.

5.3. Methods

5.3.1. Patient Selection

For this study data was used from nine patients included in the MITCH study in which children (6-18 years old) diagnosed with a brain tumor underwent metabolic research scans in addition to their standard clinical imaging protocol. 7 Tesla MRI scans (Achieva, Philips Healthcare, The Netherlands) were performed at three time points: baseline (BL), follow-up 1 (FU-1), and follow-up 2 (FU-2). The baseline scan did not necessarily align with the diagnosis but was acquired at any point during the patient's oncological follow-up. During the research period, patients could receive chemotherapy, radiation therapy, or remain untreated.

This study was approved by the local ethics committee of the UMC Utrecht, and written informed consent was obtained from all patients and their legal guardians. Disease progression was assessed by a multidisciplinary tumor board consisting of at least one oncologist, neurologist, ophthalmologist, surgeon, and radiologist based on clinical and imaging findings. These specialists were blinded to the acquired ^{31}P-MRSI data.

5.3.2. ^{31}P-MRSI Acquisition

^{31}P-MRSI was acquired on a home-build quadrature TxRx ^{31}H/^{31}P head coil. The MRSI protocol employed a 3D chemical shift imaging (CSI) sequence with a matrix size of [11, 11, 9], a nominal isotropic resolution of 20x20x20 mm^3, a repetition time (TR) of 100 ms and a flip angle (α) of 11.4 degrees. Hamming-weighted k-space sampling was applied to improve the signal-to-noise ratio (SNR). The number of signal averages (NSA) was set to 28.

5.3.3. MRSI Data Processing and Quantification

^{31}P MRSI datasets were processed and evaluated using in-house MATLAB software [46]. K-space regridding was performed according to the methods described in Chapters 3 & 4, focusing on the voxel with the largest tumor content. Spectral quantification was conducted in the time domain using a home-built MATLAB implementation of the AMARES algorithm [28]. Quantification was performed in two steps:

- Prefitting: Estimation of the local B_0 shift and zero-order phase correction (ϕ_0) by fitting the phosphocreatine (PCr) resonance as a singlet with a variable frequency range of $[-0.5, +0.5]$ ppm [28].
- Main Quantification: Performed on the phase-corrected MRSI dataset with frequency constraints adapted to the local B_0 estimated in the prefitting step. Residual phase errors were compensated by allowing ϕ_0 to vary within $[-0.09\times\pi, +0.09\times\pi]$ [28].

Twelve metabolites were quantified, including PCr, ATP, NAD, GPC, GPE, PC, PE, Pi, ePi, UDPG, MPL, and DPG. UDPG is a sugar nucleotide underlying PE and PC. It was modeled as a pseudo-doublet with a fixed frequency spacing of $\Delta f = 1.6$ ppm following methods described in [28].

Spectral quality was assessed by the SNR, defined as the signal amplitude of PCr divided by the standard deviation of the noise, FWHM of the PCr peak, and the presence of artifacts. Spectra were excluded if the FWHM >25Hz, the SNR <10, or if there were large artifacts assessed by an expert. Patients were excluded from the analysis if they had only one timepoint available for evaluation, as no metabolic change could be evaluated.

5.3.4. Tumor and Normal-Appearing White Matter (NAWM) Region of Interest (ROI) Analysis

Tumors were delineated on FLAIR images by a pediatric neuroradiologist with over ten years of experience using ITK-SNAP (v4.0.1). A control region in normal-appearing white matter (NAWM) was defined superior to the lesion, at least 2 cm away from the tumor ROI, in an area without observable pathology. The follow-up ROI was chosen at the same anatomical location as the baseline scan ROI.

5.3.5. Analysis

The following metabolic ratios were calculated for the analysis representing different processes: PE/GPE (cell membrane metabolism), PCr/γATP (energetic state), pH (hypoxia), Pi/ATP (ATP turnover) [Appendix A]. To assess whether changes in tumor tissue differed from those in NAWM, relative metabolite ratios were calculated. For each patient, the metabolite value in the tumor voxel at each time point was divided by the corresponding NAWM voxel value. To focus on changes over time, these ratios were further normalized to their baseline value. Metabolite ratios between the tumor and NAWM ROIs were compared. Changes between consecutive time points were analyzed separately for progressors and non-progressors. Comparisons between metabolic ratios of tumors and NAWM were performed using the Wilcoxon signed-rank test, accounting for the non-independence of paired measurements. A significance threshold of $p<0.05$ was applied.

5.4. Results

Eight patients (six males and two females) with a median age of 7 years were included in this study, patient information can be found in Table 5.1. Two spectra were excluded because of low SNR and large linewidth, leading to the exclusion of one patient because it had only one timepoint available for evaluation. Patient characteristics are summarized in Table 5.1. All patients had a low-grade glioma (LGG), including optic pathway glioma, pilocytic astrocytoma, and diffuse leptomeningeal glioneuronal tumor (DLGNT). The treatment regimens at each time point are detailed in Table 5.2.

Four patients completed the full follow-up, while four had data available only for baseline and the first follow-up. One patient did not receive treatment throughout the study, while the remaining patients underwent various chemotherapy regimens, including bevacizumab, irinotecan, vincristine, and carboplatin.

In patients 340, 498, 224, and 962, the tumor volume within the analyzed voxel remained below 52%. The average metabolic values and their standard deviation for tumors and NAWM in all scans are

Variable	**n**
Total Patients	8
Age (years)	
Median	7
Range	6-14
Sex	
Male	6
Female	2
Tumor Type	
Low-Grade Glioma	8
Histological Subtype	
Optic Pathway Glioma	5
Pilocytic Astrocytoma	2
Diffuse Leptomeningeal Glioneuronal Tumor	1
Tumor Location	
Optic Chiasm	4
Optic Chiasm + Basal Ganglia + Thalamus + Brainstem	1
Mesencephalon	1
Right Mesiotemporal Lobe	1
Supratentorial and Infratentorial Regions	1

Table 5.1: Summary of patient demographics, including total number of patients, median and range of age, sex distribution, tumor type, histological subtype, and tumor location.

Patient	**Baseline (BL)**		**First Follow-up (FU1)**		**Second Follow-up (FU2)**	
	Treatment at time of the scan	% Tumor volume	Treatment at time of the scan	% Tumor volume	Treatment at time of the scan	% Tumor volume
340	Bevacizumab + irinotecan	27	Bevacizumab + irinotecan	30	Bevacizumab	18
498	Vincristine + carboplatin	13	Vinblastine + bevacizumab	20	Vinblastine + bevacizumab	15
680	No treatment	93	Vinblastine	89	Vinblastine	87
891	No treatment	74	-	–	No treatment	81
162	No treatment	67	Vinblastine	59	Vinblastine	72
224	Bevacizumab	51	Bevacizumab	46	Bevacizumab	–
276	Vinblastine	94	Vinblastine	95	–	–
962	Vincristine + carboplatin	40	Vincristine + carboplatin	45	–	–

Table 5.2: Overview of patient treatments and tumor volume progression at different time points. Treatments administered at the time of each MRI scan are listed along with the percentage of the voxel occupied by the tumor at baseline (BL), first follow-up (FU1), and second follow-up (FU2). Missing values indicate unavailable data.

summarized in Table 5.3. No significant differences were observed between tumors and NAWM for all metabolites.

5.4.1. Tumor metabolite ratios

Figure 5.2 illustrates the changes in the metabolite ratios for tumor and NAWM—pH (a-b), PE/GPE (d-e), PCr/γATP (g-h), and Pi/ATP (j-k)—at different time points for each patient. Panels (c-f-i-l) show normalized differences relative to NAWM and baseline. The multidisciplinary board conclusions are color-coded: red for disease progression, green for response to therapy, and orange for stable disease.

At baseline, three patients (498, 680, and 162) showed progression, leading to a therapeutic switch to vinblastine, with additional bevacizumab for patient 498. Following treatment adjustments, these patients remained stable. During follow-up, minimal pH changes were observed. PE/GPE initially decreased but later increased, PCr/γATP remained largely stable, and Pi/ATP showed minimal changes. When normalizing tumor metabolite changes to NAWM and baseline, no consistent metabolic changes were observed across these patients.

Among patients with stable or responding disease at baseline, treatment regimens remained unchanged. One patient (340) responded to bevacizumab and irinotecan at FU-1, showing decreased pH and PE/GPE, while PCr/γATP and Pi/ATP remained stable, also reflected in the relative NAWM-normalized changes.

Disease progression was observed in two patients (340 and 276) at FU-2 and FU-1, respectively. In both cases, pH and PE/GPE increased, while PCr/γATP and Pi/ATP decreased. The absolute metabolic changes for patient 340 were ΔpH = 0.0027, ΔPE/GPE = 0.33, ΔPCr/γATP = -0.45, and ΔPi/ATP = -0.034, while for patient 276, these changes were: ΔpH = 0.034, ΔPE/GPE = 0.36, ΔPCr/γATP = -0.23, and ΔPi/ATP = -0015. When normalizing tumor metabolite changes to NAWM and baseline, pH

	pH	p	PE/GPE	p	PCr/γATP	p	Pi/ATP	p
Tumor	6.999 ± 0.105		2.115 ± 0.434		1.156 ± 0.214		0.191 ± 0.052	
NAWM	7.021 ± 0.016	0.18	2.098 ± 0.354	0.74	1.105 ± 0.167	0.79	0.212 ± 0.032	0.08

Table 5.3: Metabolite ratios and pH values for tumor and normal-appearing white matter (NAWM). Values are presented as mean ± standard deviation over all patients and timepoints. p-values are calculated between tumor and NAWM, none showed statistical significance ($p<0.05$)

remained the only consistent trend in these patients. Patient 276, diagnosed with DLGNT, continued to progress rapidly after FU-1 and could not complete the study due to disease-related mortality.

5.4.2. NAWM metabolite ratios

In patient 891, who did not receive therapy, NAWM showed an increase in pH, a decrease in PE/GPE and PCr/γATP, and stable Pi/ATP levels. When tumor metabolite changes were normalized to NAWM, no additional consistent metabolic changes emerged.

Among the two patients who exhibited disease progression, metabolic alterations in NAWM mirrored those in the tumor, leading to inconsistent relative differences. One patient switched to bevacizumab after discontinuing irinotecan before progression, while the other continued with vinblastine.

No clear metabolic trends in metabolite changes emerged across different therapy types. The most stable NAWM metabolite ratio was PCr/γATP.

5.5. Discussion

This study investigated metabolic changes in pediatric LGG's over time using ^{31}P-MRSI, focusing on tumor response to therapy and potential biomarkers of disease progression. Our findings highlight metabolic alterations in tumors and NAWM, however no trends in metabolite changes were observed when normalizing tumor metabolic ratios to their NAWM.

5.5.1. Metabolic Alterations in Tumor and NAWM

Tumor comparison was challenging due to anatomical variations and differences in treatment regimens. In half of the patients, the tumor was smaller than an MRSI voxel, and even after regridding, it did not fully occupy the MRSI voxel. This led to partial volume effects, where tumor and NAWM signals were mixed, complicating the interpretation of metabolic changes.

The two patients with disease progression exhibited similar metabolic alterations, including increased energy metabolism (pH and Pi/ATP), reduced ATP synthesis (PCr/γATP), and altered phospholipid turnover (PE/GPE). Furthermore, patients with stable disease or response to therapy showed a decrease in phospholipid turnover (PE/GPE) and stable ATP levels (PCr/γATP). These changes align with previous studies on the effects of therapy on phosphorus metabolites in brain tumors [33, 36, 37]. However, none of the changing metabolic ratios remained consistent after normalization to NAWM and baseline, suggesting that they may reflect normal biological variation, incidental findings, or treatment effects that influence both tumor and NAWM metabolism.

To determine whether the observed metabolic changes fall within the expected biological range, we compared our findings with values reported in the literature. While reference values for adult NAWM are available, data for the pediatric population remain limited. However, pediatric comparisons are essential, as Raz et al. [48] reported significant metabolic differences between children and adults at 3T. The study included 48 children (age 10.6 ± 2.4) and 80 adults (age 69.1 ± 7.3) and they found significantly higher PME, γATP, and pH levels in children compared to adults, while PDE and Pi levels were lower. A study by Albers et al. [49] provided absolute values, acquired with a 1.5T MRI scanner, for eight patients (age 7.4 ± 5.1) with aggressive tumors (e.g., primitive neuroectodermal tumors, ependymoma, anaplastic astrocytoma) and six healthy controls (age 6.3 ± 5.3):

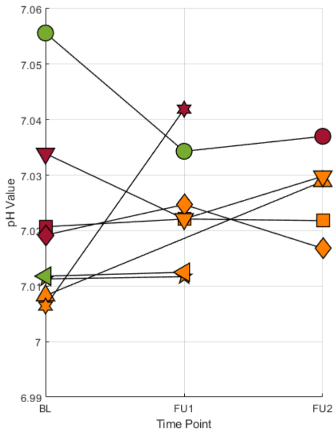

(a) pH in tumor over time

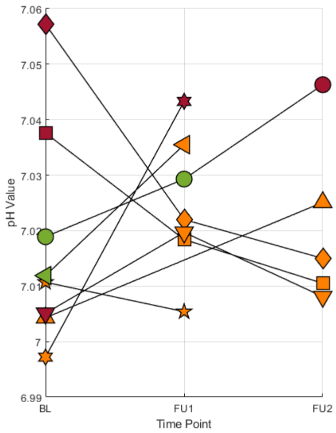

(b) pH in NAWM over time

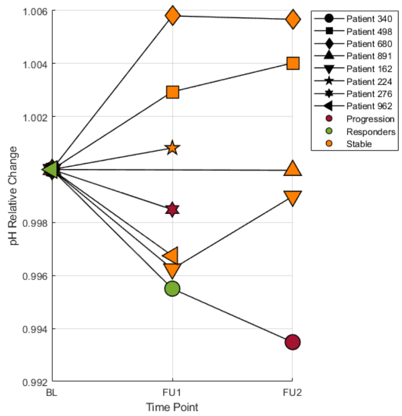

(c) pH tumor relative change

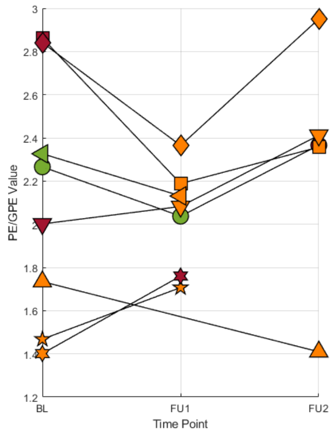

(d) PE/GPE in tumor over time

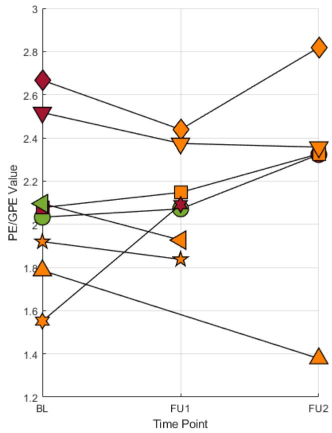

(e) PE/GPE in NAWM over time

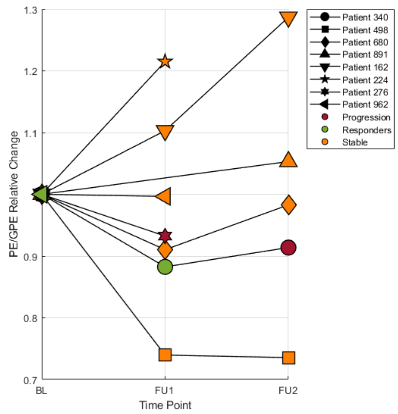

(f) PE/GPE tumor relative change

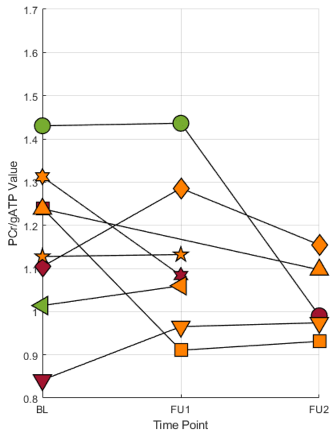

(g) PCr/γATP in tumor over time

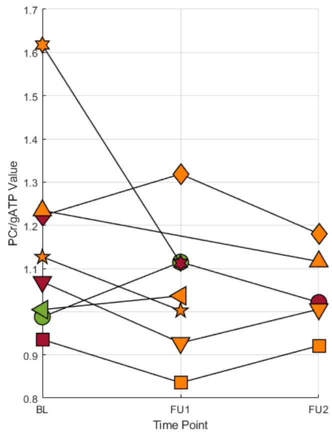

(h) PCr/γATP in NAWM over time

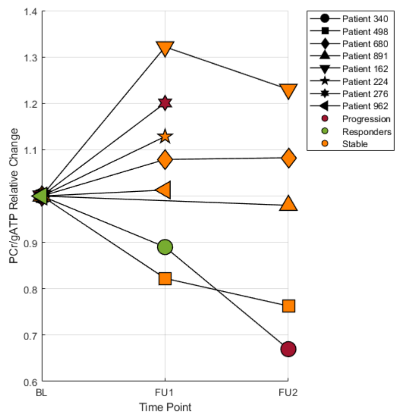

(i) PCr/γATP tumor relative change

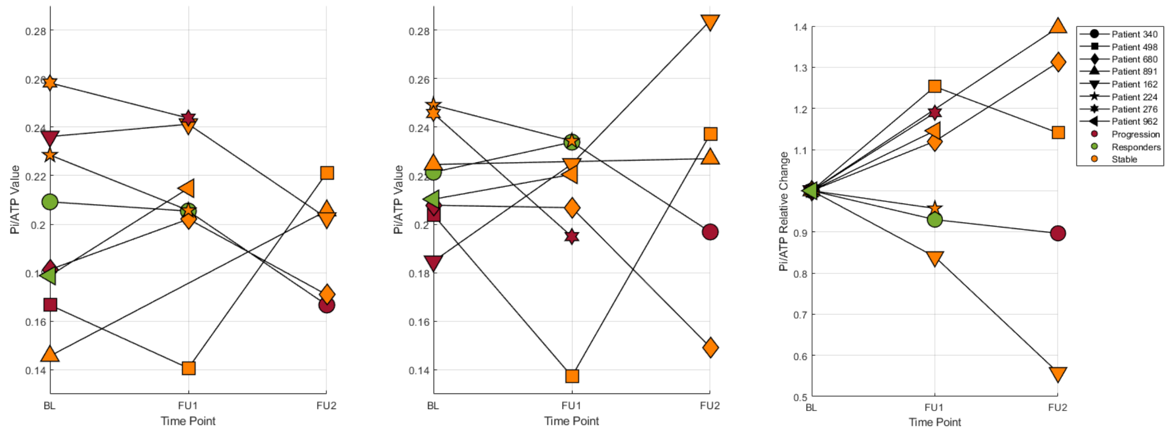

(j) Pi/ATP in tumor over time (k) Pi/ATP in NAWM over time (l) Pi/ATP tumor relative change

Figure 5.2: Longitudinal changes in tumor and normal appearing white matter (NAWM) metabolism and the relative tumor changes normalized to NAWM for pH (a–c) PE/GPE (d–f) PCr//γATP (g–i). The multidisciplinary board conclusions are color-coded: red indicates disease progression, green indicates a response to therapy, and orange represents a stable scan.

- **Tumors:** PCr/ATP = 1.22 ± 0.54, PE/GPE = 9.23 ± 7.78, Pi/ATP = 0.39 ± 0.14, pH = 7.06 ± 0.03.
- **NAWM healthy controls:** PCr/ATP = 2.07 ± 0.17, PE/GPE = 3.42 ± 1.62, Pi/ATP = 0.40 ± 0.14, pH = 6.98 ± 0.03.

The differences between tumor and NAWM in the literature and in our data are small, with large confidence intervals. In our study, tumor and NAWM values fall largely within the standard deviation of pediatric NAWM, except for Pi/ATP, which was slightly lower. Similarly, Novak et al. [25] found slightly lower Pi/ATP values in both tumor and NAWM in three patients with LGG. Given that pediatric LGGs are slow-growing and have a favorable prognosis, with a 10-year survival rate exceeding 95% [1], their metabolic profile may not differ substantially from NAWM, supporting the hypothesis that observed metabolic differences may not exceed normal inter-individual variation.

Furthermore, normalizing the metabolic ratios of the tumor to NAWM did not yield distinct differences, raising the question whether the treatment has an effect on both the tumor and NAWM. Previous studies in adults indicate that therapies such as temozolomide and bevacizumab affect phosphorus metabolites in NAWM [36, 50, 37], potentially contributing to the observed variability. In our study, metabolic changes in NAWM were detected in both treated and untreated patients. In patients with tumor progression, NAWM metabolic alterations resembled those in tumor tissue, leading to inconsistent relative differences. No clear metabolic changes were associated with specific therapies, which could be due to the small sample size and the distinct molecular targets of treatments in this cohort. The therapies studied pathways related to angiogenesis, DNA synthesis, and cell division [51], which may explain the absence of a uniform metabolic response across patients.

Finally, another consideration is the repeatability of ^{31}P-MRSI at 7T in vivo. Lagemaat et al. [45] assessed the within-session reliability of a 3D-^{31}P-MRSI sequence in healthy adults and reported coefficients of variation for different metabolites and brain regions reporting coefficients of variation of <6% for PCr and ATP, <12% for PE, GPE, and GPC, and <20% for PC and PE [45]

5.5.2. Clinical Implications and Future Directions

Patient 680 exhibited metabolic changes similar to those observed in progressive cases, including increased PE/GPE and decreased PCr/γATP and Pi/ATP at FU-2, along with slight tumor growth on clinical imaging. However, the multidisciplinary tumor board classified the patient as stable, as no neurological or visual deterioration was observed. This underscores that tumor growth and metabolic alterations alone may not be sufficient indicators of disease progression when assessed in a clinical context, where functional measures such as vision, motor function, reflexes, coordination, sensation, and gait pattern are also considered [11].

The metabolic changes observed in this study warrant further investigation as potential biomarkers for disease monitoring. Early metabolic alterations in tumors could aid in treatment planning. If an early biomarker were identified for progression, it could justify initiating treatment before clinical symptoms emerge. However, given the subtlety of metabolic changes and their overlap with normal NAWM variation, the clinical feasibility of such an approach remains uncertain.

Higher-grade gliomas may provide a better model for identifying metabolic differences, as these tumors are metabolically more active they might exhibit more pronounced metabolic alterations [49]. However, the clinical impact of these findings is uncertain. In high-grade tumors, treatment decisions are often guided by the aggressive nature of the disease, and additional metabolic biomarkers may not substantially change clinical management.

Distinguishing between different pediatric brain lesions, such as LGGs, germinomas, or neurofibromatosis type 1 (NF1)-associated lesions, remains a challenge in pediatric radiology. It would be highly valuable if metabolic information from ^{31}P-MRSI could aid in this distinction, potentially reducing the need for invasive biopsies, particularly in cases where surgical intervention poses significant risks.

Similarly, differentiating between active tumor growth and treatment-related effects, such as pseudoprogression or radiation necrosis, is a major challenge in pediatric radiology. More non-invasive methods to assess tumor viability would be highly beneficial, as distinguishing viable tumor tissue from post-treatment changes has significant implications for therapy planning and prognosis. More research is needed to determine whether phosphorus metabolites could provide useful markers in this context.

Imaging was conducted on a 7T MRI scanner, providing high spectral and spatial resolution that is not typically available in clinical settings. While this limits the immediate clinical applicability, it also allows for the most detailed metabolic assessment currently possible. If successful, these findings could inform future studies exploring the feasibility of translating this approach to more widely available 3T scanners.

5.5.3. Limitations

This study has some limitations. The small sample size limits the generalizability of the findings, and the relatively large voxel size increases the likelihood of partial volume effects. Additionally, only a single MRSI voxel was analyzed for NAWM, making it susceptible to contamination of other structures. Future studies could improve accuracy by averaging metabolic values across multiple white matter MRSI voxels for a more representative measure of NAWM metabolism.

5.6. Conclusion

This study found metabolic changes in pediatric low-grade gliomas and normal appearing white matter over time using ^{31}P-MRSI. However, their clinical relevance requires further investigation.

6 Conclusion

In this study, we demonstrate that applying a phase shift as a post-processing step in ^{31}P-MRSI improves spatial localization by incorporating a greater proportion of tumor tissue within MRSI voxels while preserving spectral quality. Additionally, metabolic ratio analyses over time in pediatric patients with low-grade brain tumors revealed variations in metabolite profiles, which may reflect tumor-specific metabolic activity, normal cerebral fluctuations, or treatment effects. Overall, our findings highlight the potential of ^{31}P-MRSI at 7T, combined with regridding techniques, to enhance spatial localization and mitigate partial volume effects. Further research is needed to validate the clinical utility of ^{31}P-MRSI in pediatric brain tumors.

References

[1] Quinn T Ostrom, Stephen S Francis, and Jill S Barnholtz-Sloan. "Epidemiology of brain and other CNS tumors". en. In: *Curr. Neurol. Neurosci. Rep.* 21.12 (Nov. 2021), p. 68.

[2] GBD 2016 Brain and Other CNS Cancer Collaborators. "Global, regional, and national burden of brain and other CNS cancer, 1990-2016: a systematic analysis for the Global Burden of Disease Study 2016". en. In: *Lancet Neurol.* 18.4 (Apr. 2019), pp. 376–393.

[3] Lindsey M Hoffman et al. "Clinical, radiologic, pathologic, and molecular characteristics of long-term survivors of Diffuse intrinsic pontine glioma (DIPG): A collaborative report from the international and European society for pediatric oncology DIPG registries". en. In: *J. Clin. Oncol.* 36.19 (July 2018), pp. 1963–1972.

[4] M. L. Bondy et al. "Brain tumor epidemiology: consensus from the Brain Tumor Epidemiology Consortium". In: *Cancer* 113.7 Suppl (2008), pp. 1953–68. ISSN: 0008-543X (Print) 0008-543x. DOI: 10.1002/cncr.23741.

[5] I. Ilic and M. Ilic. "International patterns and trends in the brain cancer incidence and mortality: An observational study based on the global burden of disease". In: *Heliyon* 9.7 (2023), e18222. ISSN: 2405-8440 (Print) 2405-8440. DOI: 10.1016/j.heliyon.2023.e18222.

[6] Jackson Lanphear and Syana Sarnaik. "Presenting symptoms of pediatric brain tumors diagnosed in the emergency department". en. In: *Pediatr. Emerg. Care* 30.2 (Feb. 2014), pp. 77–80.

[7] Rachmat Hidayat. "Effectiveness of MRI in detecting and diagnosing brain tumors in children: A meta-analysis". In: *sjrir* 2.1 (Apr. 2024), pp. 150–156.

[8] Kai Kallenberg et al. "Magnetic resonance imaging evidence of cytotoxic cerebral edema in acute mountain sickness". en. In: *J. Cereb. Blood Flow Metab.* 27.5 (May 2007), pp. 1064–1071.

[9] Javier E Villanueva-Meyer, Marc C Mabray, and Soonmee Cha. "Current clinical brain tumor imaging". en. In: *Neurosurgery* 81.3 (Sept. 2017), pp. 397–415.

[10] Marco Essig, Julien Dinkel, and Juan E. Gutierrez. "Use of Contrast Media in Neuroimaging". In: *Magnetic Resonance Imaging Clinics of North America* 20.4 (2012). MR Contrast Agents, pp. 633–648. ISSN: 1064-9689. DOI: https://doi.org/10.1016/j.mric.2012.08.001. URL: https://www.sciencedirect.com/science/article/pii/S1064968912000931.

[11] Craig Erker et al. "Response assessment in paediatric high-grade glioma: recommendations from the Response Assessment in Pediatric Neuro-Oncology (RAPNO) working group". en. In: *Lancet Oncol.* 21.6 (June 2020), e317–e329.

[12] Jason Fangusaro et al. "Response assessment in paediatric low-grade glioma: recommendations from the Response Assessment in Pediatric Neuro-Oncology (RAPNO) working group". en. In: *Lancet Oncol.* 21.6 (June 2020), e305–e316.

[13] M. C. de Wit et al. "Immediate post-radiotherapy changes in malignant glioma can mimic tumor progression". In: *Neurology* 63.3 (2004), pp. 535–7. ISSN: 0028-3878. DOI: 10.1212/01.wnl.0000133398.11870.9a.

[14] D. Brandsma et al. "Clinical features, mechanisms, and management of pseudoprogression in malignant gliomas". In: *Lancet Oncol* 9.5 (2008), pp. 453–61. ISSN: 1470-2045. DOI: 10.1016/s1470-2045(08)70125-6.

[15] J. G. Cairncross et al. "Postoperative contrast enhancement in patients with brain tumor". In: *Ann Neurol* 17.6 (1985), pp. 570–2. ISSN: 0364-5134 (Print) 0364-5134. DOI: 10.1002/ana.410170607.

[16] M. C. Chamberlain et al. "Early necrosis following concurrent Temodar and radiotherapy in patients with glioblastoma". In: *J Neurooncol* 82.1 (2007), pp. 81–3. ISSN: 0167-594X (Print) 0167-594x. DOI: 10.1007/s11060-006-9241-y.

[17] Fulvio Zaccagna et al. "Imaging and treatment of brain tumors through molecular targeting: Recent clinical advances". en. In: *Eur. J. Radiol.* 142.109842 (Sept. 2021), p. 109842.

[18] Catherine Coolens et al. "Transformational role of medical imaging in (radiation) oncology". en. In: *Cancers (Basel)* 13.11 (May 2021), p. 2557.

[19] Roberto Liserre, Lorenzo Pinelli, and Roberto Gasparotti. "MR spectroscopy in pediatric neuroradiology". en. In: *Transl. Pediatr.* 10.4 (Apr. 2021), pp. 1169–1200.

[20] Laiz Laura de Godoy et al. "Non-invasive assessment of isocitrate dehydrogenase-mutant gliomas using optimized proton magnetic resonance spectroscopy on a routine clinical 3-Tesla MRI". en. In: *Cancers (Basel)* 15.18 (Sept. 2023), p. 4453.

[21] R.A. Graaf. "Magnetic Resonance Imaging". In: *In Vivo NMR Spectroscopy.* John Wiley & Sons, Ltd, 2019. Chap. 1, pp. 211–252. ISBN: 9781119382461. DOI: `https://doi.org/10.1002/9781119382461.ch4`. eprint: `https://onlinelibrary.wiley.com/doi/pdf/10.1002/9781119382461.ch4`. URL: `https://onlinelibrary.wiley.com/doi/abs/10.1002/9781119382461.ch4`.

[22] A. Korzowski et al. "Mapping an Extended Metabolic Profile of Gliomas Using High-Resolution (31)P MRSI at 7T". In: *Front Neurol* 12 (2021), p. 735071. ISSN: 1664-2295 (Print) 1664-2295. DOI: `10.3389/fneur.2021.735071`.

[23] R.H. Hashemi, W.G. Bradley, and C.J. Lisanti. *MRI: The Basics.* The Basics Series. Lippincott Williams & Wilkins, 2010. ISBN: 9781608311156. URL: `https://books.google.nl/books?id=v4LFgAHxNz4C`.

[24] Y. Liu, Y. Gu, and X. Yu. "Assessing tissue metabolism by phosphorous-31 magnetic resonance spectroscopy and imaging: a methodology review". In: *Quant Imaging Med Surg* 7.6 (2017), pp. 707–726. ISSN: 2223-4292 (Print) 2223-4306. DOI: `10.21037/qims.2017.11.03`.

[25] J. Novak et al. "Clinical protocols for ^{31}P MRS of the brain and their use in evaluating optic pathway gliomas in children". In: *Eur J Radiol* 83.2 (2014), e106–12. ISSN: 0720-048X (Print) 0720-048x. DOI: `10.1016/j.ejrad.2013.11.009`.

[26] Carsten A Wagner. "The basics of phosphate metabolism". en. In: *Nephrol. Dial. Transplant* 39.2 (Jan. 2024), pp. 190–201.

[27] C. Mirkes et al. "(31)P CSI of the human brain in healthy subjects and tumor patients at 9.4 T with a three-layered multi-nuclear coil: initial results". In: *Magma* 29.3 (2016), pp. 579–89. ISSN: 0968-5243. DOI: `10.1007/s10334-016-0524-9`.

[28] A. Korzowski et al. "Volumetric mapping of intra- and extracellular pH in the human brain using (31) P MRSI at 7T". In: *Magn Reson Med* 84.4 (2020), pp. 1707–1723. ISSN: 0740-3194. DOI: `10.1002/mrm.28255`.

[29] F. Podo. "Tumour phospholipid metabolism". In: *NMR Biomed* 12.7 (1999), pp. 413–39. ISSN: 0952-3480 (Print) 0952-3480. DOI: `10.1002/(sici)1099-1492(199911)12:7<413::aid-nbm587>3.0.co;2-u`.

[30] D F Cain and R E Davies. "Breakdown of adenosine triphosphate during a single contraction of working muscle". en. In: *Biochem. Biophys. Res. Commun.* 8.5 (Aug. 1962), pp. 361–366.

[31] Meinrad Beer et al. "Absolute concentrations of high-energy phosphate metabolites in normal, hypertrophied, and failing human myocardium measured noninvasively with 31P-SLOOP magnetic resonance spectroscopy". en. In: *J. Am. Coll. Cardiol.* 40.7 (Oct. 2002), pp. 1267–1274.

[32] Britton Chance et al. "Skeletal muscle energetics with PNMR: personal views and historic perspectives". en. In: *NMR Biomed.* 19.7 (Nov. 2006), pp. 904–926.

[33] G J Kemp. "Non-invasive methods for studying brain energy metabolism: what they show and what it means". en. In: *Dev. Neurosci.* 22.5-6 (Sept. 2000), pp. 418–428.

[34] Johanna Chiche, M Christiane Brahimi-Horn, and Jacques Pouysségur. "Tumour hypoxia induces a metabolic shift causing acidosis: a common feature in cancer". en. In: *J. Cell. Mol. Med.* 14.4 (Apr. 2010), pp. 771–794.

[35] D. H. Ha et al. "Application of 31P MR spectroscopy to the brain tumors". In: *Korean J Radiol* 14.3 (2013), pp. 477–86. ISSN: 1229-6929 (Print) 1229-6929. DOI: `10.3348/kjr.2013.14.3.477`.

[36] A. E. Grams et al. “Changes in Brain Energy and Membrane Metabolism in Glioblastoma following Chemoradiation”. In: *Current oncology (Toronto, Ont.)* 28.6 (2021), pp. 5041–5053. ISSN: 1718-7729 (Electronic). DOI: 10.3390/curroncol28060424. URL: https://pubmed.ncbi.nlm.nih.gov/34940063/.

[37] E. Hattingen et al. “Bevacizumab impairs oxidative energy metabolism and shows antitumoral effects in recurrent glioblastomas: a 31P/1H MRSI and quantitative magnetic resonance imaging study”. In: *Neuro Oncol* 13.12 (2011), pp. 1349–63. ISSN: 1522-8517 (Print) 1522-8517. DOI: 10.1093/neuonc/nor132.

[38] N Bulakbasi et al. “Efficacy of in vivo 31Phosphorus magnetic resonance spectroscopy in differentiation and staging of adult human brain tumors”. en. In: *Neuroradiol. J.* 20.6 (Dec. 2007), pp. 646–655.

[39] H. J. Hoekstra et al. “Clinical applicability of human in vivo localized phosphorus-31 magnetic resonance spectroscopy of bone and soft tissue tumors”. In: *Ann Surg Oncol* 1.6 (1994), pp. 504–11. ISSN: 1068-9265 (Print) 1068-9265. DOI: 10.1007/bf02303616.

[40] R.A. Graaf. “Spectroscopic Imaging and Multivolume Localization”. In: *In Vivo NMR Spectroscopy*. John Wiley & Sons, Ltd, 2019. Chap. 7, pp. 335–373. ISBN: 9781119382461. DOI: https://doi.org/10.1002/9781119382461.ch7. eprint: https://onlinelibrary.wiley.com/doi/pdf/10.1002/9781119382461.ch7. URL: https://onlinelibrary.wiley.com/doi/abs/10.1002/9781119382461.ch7.

[41] R.A. Graaf. “Spectral Quantification”. In: *In Vivo NMR Spectroscopy*. John Wiley & Sons, Ltd, 2019. Chap. 9, pp. 439–471. ISBN: 9781119382461. DOI: https://doi.org/10.1002/9781119382461.ch9. eprint: https://onlinelibrary.wiley.com/doi/pdf/10.1002/9781119382461.ch9. URL: https://onlinelibrary.wiley.com/doi/abs/10.1002/9781119382461.ch9.

[42] R.A. Graaf. “Magnetic Resonance Imaging”. In: *In Vivo NMR Spectroscopy*. John Wiley & Sons, Ltd, 2019. Chap. 4, pp. 211–252. ISBN: 9781119382461. DOI: https://doi.org/10.1002/9781119382461.ch4. eprint: https://onlinelibrary.wiley.com/doi/pdf/10.1002/9781119382461.ch4. URL: https://onlinelibrary.wiley.com/doi/abs/10.1002/9781119382461.ch4.

[43] Lucian A B Purvis et al. “OXSA: An open-source magnetic resonance spectroscopy analysis toolbox in MATLAB”. en. In: *PLoS One* 12.9 (Sept. 2017), e0185356.

[44] Haldun Akoglu. “User’s guide to correlation coefficients”. en. In: *Turk. J. Emerg. Med.* 18.3 (Sept. 2018), pp. 91–93.

[45] Miriam W Lagemaat et al. “Repeatability of 31 P MRSI in the human brain at 7 T with and without the nuclear Overhauser effect”. en. In: *NMR Biomed.* 29.3 (Mar. 2016), pp. 256–263.

[46] The MathWorks Inc. *MATLAB version: 9.10 (R2021a)*. Natick, Massachusetts, United States, 2021a. URL: https://www.mathworks.com.

[47] Antonin Skoch, Filip Jiru, and Jürgen Bunke. “Spectroscopic imaging: Basic principles”. In: *European Journal of Radiology* 67.2 (2008). Clinical 1H MR Spectroscopy, pp. 230–239. ISSN: 0720-048X. DOI: https://doi.org/10.1016/j.ejrad.2008.03.003. URL: https://www.sciencedirect.com/science/article/pii/S0720048X08001459.

[48] Naftali Raz et al. “Mapping age differences in brain energy metabolites and metabolic markers of cellular membrane production and degradation with 31P magnetic resonance spectroscopy”. en. In: *Hum. Brain Mapp.* 45.14 (Oct. 2024), e70039.

[49] M. J. Albers et al. “Proton-decoupled 31P MRS in untreated pediatric brain tumors”. In: *Magn Reson Med* 53.1 (2005), pp. 22–9. ISSN: 0740-3194 (Print) 0740-3194. DOI: 10.1002/mrm.20312.

[50] Lisa Maria Walchhofer et al. “Phosphorous magnetic resonance spectroscopy to detect regional differences of energy and membrane metabolism in naïve glioblastoma multiforme”. en. In: *Cancers (Basel)* 13.11 (May 2021), p. 2598.

[51] *National cancer institute (.Gov)*. en. https://www.cancer.gov/about-cancer/treatment/drugs. Accessed: 2025-2-20. Jan. 2012.

A

Literature Review

A literature review for the course TM30003

Evaluating APT-CEST and ^{31}P MRSI Imaging in Brain Tumors: A Literature Review of Diagnostic Performance, Repeatability, and Therapy Response

H.Roording, MSc student

[a]*University Medical Center Utrecht, Division of Image and Oncology*, the Netherlands [b]Delft University of Technology, the Netherlands

Abstract

Introduction Brain cancer poses significant challenges despite advances in treatment. Advanced imaging techniques, amide proton transfer chemical exchange saturation transfer (APT-CEST), and phosphorus-31 magnetic resonance spectroscopy imaging (^{31}P MRSI) offer potential insights into tumor metabolism. This review updates the role of APT-CEST and ^{31}P MRSI in brain cancer diagnosis and therapy monitoring.

Methods In June 2024, a systematic search of PubMed, Embase, and Scopus was conducted for studies on brain cancer, APT-CEST, and ^{31}P MRSI. Abstracts were screened, and data on imaging parameters, therapy schemas, and patient demographics were extracted.

Results Thirteen studies were included—nine on APT-CEST (229 patients) and four on ^{31}P MRSI (63 patients), all prospective. APT-CEST showed consistent within and between-session repeatability and effective tumor differentiation. It identified therapy response with higher baseline magnetization transfer ratio asymmetry (MTRasym) values predicting early progression. ^{31}P MRSI demonstrated consistent repeatability and metabolic differences between tumors and normal-appearing white matter (NAWM). Changes in pH and metabolite ratios during therapy were noted.

Conclusion This review highlights the potential of APT-CEST and ^{31}P MRSI imaging techniques to enhance brain tumor diagnosis and monitoring, emphasizing the need for standardized protocols and further research to address technical challenges and optimize clinical application.

Keywords: APT-CEST Imaging, ^{31}P MRSI, Brain Tumor, Diagnostic Performance, Therapy Response Monitoring

1. Introduction

Brain cancer remains a major clinical challenge due to its high morbidity and mortality rates despite advances in diagnosis and treatment strategies such as surgery, radiation therapy, and chemotherapy (13, 14). Conventional assessment of diagnosis, resection results, and therapy response relies on structural magnetic resonance imaging (MRI) scans. For example, therapy response can be evaluated using the response assessment in neuro-oncology (RANO) criteria, which categorizes outcomes based on lesion size, new lesions, and clinical parameters (17). However, differentiating true tumor progression from pseudoprogression –therapy-induced contrast-enhanced or T2/FLAIR hyperintense regions that mimic progression– remains a significant challenge (18-21).

Advanced imaging techniques are increasingly helpful in understanding tumor biology, guiding treatment, and predicting patient outcomes (22). Two modalities, amide proton transfer chemical exchange saturation transfer (APT-CEST) and phosphorus-31 magnetic resonance spectroscopy imaging (^{31}P

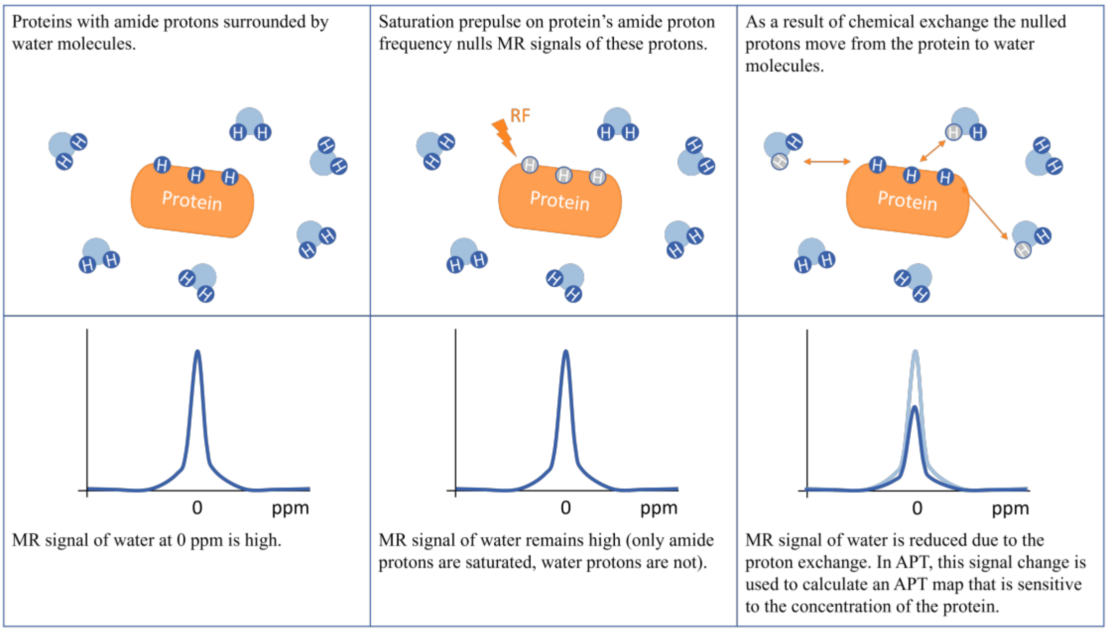

Figure 1: A visual representation of the general principle of chemical exchange saturation transfer (CEST). The bottom row shows the effect of the saturation and magnetization transfer on the proton spectrum (11).

MRSI) offer promising new ways to evaluate brain tumors.

APT-CEST is an MRI technique that detects proton exchanges between endogenous amide groups in mobile proteins and peptides and the surrounding water, enabling visualization of protein concentration and pH changes in tissue (11, 23-25). Using a selective radiofrequency (RF) saturation pulse targeted at 3.5 ppm for APT, a CEST signal is generated by transferring saturated protons to free water protons resulting in a measurable reduction in the water signal amplitude, as explained in Figure 1 (23, 24). This method is sensitive to microenvironmental changes, such as increased protein synthesis and acidity, which are common in malignancies (24, 26-29). APT-CEST has demonstrated potential in differentiating tumor grades, distinguishing tumor recurrence from treatment-related changes, and assessing therapy response (25, 26, 30-33).

^{31}P MRSI, on the other hand, offers unique insights into tumor metabolism by measuring phosphorus-containing metabolites, such as phosphocreatine (PCr), adenosine triphosphate (ATP), phosphomonoesters (PME), inorganic phosphate (Pi), glycerophosphoethanolamine (GPE), phosphoethanolamine (PE), phosphocholine (PC), glycerophosphocholine (GPE), and phosphodiesters (PDE), which are involved in energy production, cell membrane synthesis, and cellular pH regulation (34-36). This technique utilizes the magnetic resonance properties of the phosphorus-31 nucleus to detect the chemical shifts of these metabolites in tissues (37). By applying specific RF pulses, ^{31}P MRSI generates a spectrum (Figure 2) reflecting metabolite concentrations, offering potential in differentiating tumor types, assessing treatment response, and distinguishing recurrent tumors from radiation necrosis (37-45).

Despite the promising potential of APT-CEST and ^{31}P MRSI in brain cancer, their clinical application remains limited by variability in study designs, imaging protocols, and inconsistent findings across studies. A systematic review by Okuchi et al. (46) highlighted the potential of CEST imaging in brain tumor diagnosis and therapy response assessment but noted the need for more evidence to resolve technical challenges and enhance clinical utility. Additionally, an umbrella review by Dagher et al. (47) found promising results for APT-CEST MRI in differentiating tumor progression from

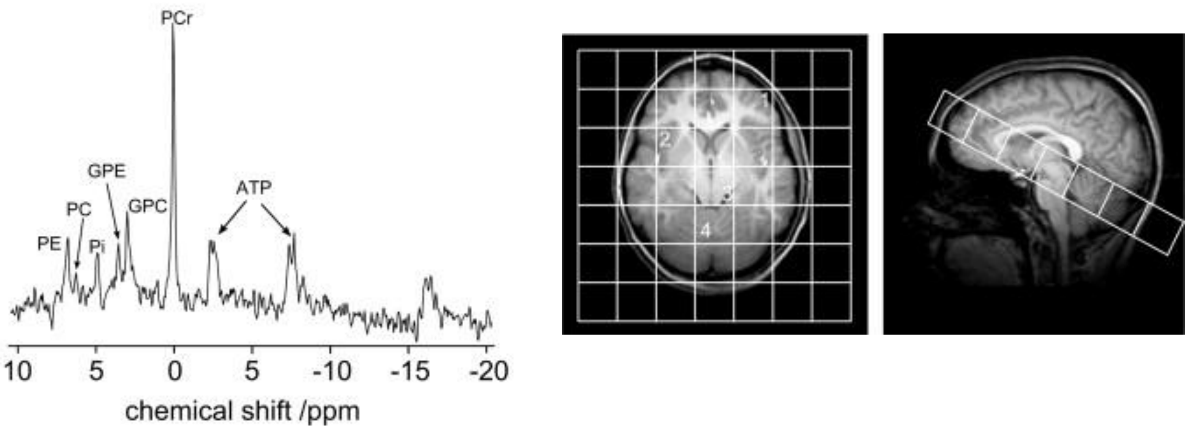

Figure 2: ^{31}P Magnetic Resonance Spectroscopic Imaging (MRSI) spectrum obtained from a healthy volunteer. The orientation of the grid is shown on the right. The orientation of the MRSI grid allowed simultaneous metabolic profiling of various regions of the brain (12).

pseudoprogression and radionecrosis. However, since 2018, no systematic reviews have focused on therapy response assessment with APT-CEST despite significant new research advances.

Likewise, no comprehensive systematic reviews exist on ^{31}P MRSI across various brain tumors and treatments. The limited evaluation by El-Abtah et al. (48) only covered one specific tumor type following chemotherapy; they identified metabolite changes associated with survival outcomes.

The current literature review provides an updated overview of APT-CEST and ^{31}P MRSI in brain cancer patients, focusing on monitoring therapy response. Additionally, it assesses repeatability and diagnostic performance.

2. Methods

2.1 Search Methodology

In June 2024, a systematic search was conducted using PubMed, Embase, and Scopus. The search terms focused on brain cancer, APT-CEST imaging, and ^{31}P MRSI imaging. Further details of the search strategy are provided in Appendix A. For studies involving APT-CEST imaging, only articles published after 2018 were reviewed because of a systematic review that had already covered studies before 2018 on a similar topic (46).

2.2 Selection criteria

Abstracts were screened by one reviewer based on predefined inclusion and exclusion criteria. Studies were included if they involved the ^{31}P MRSI or APT-CEST technique on at least two occasions in patients with brain cancer. Exclusion criteria were: (a) animal or laboratory studies; (b) review articles, case reports with fewer than five cases, letters, commentaries, or conference proceedings; (c) non-English full text; (d) studies utilizing different MRI scanners or field strengths for a single patient. Rayyan, a tool for study selection, was used for the selection (49). Duplicates were extracted using partially automated methods, and manual abstract and full-text screening was performed.

2.3 Data extraction

The extracted data from the included studies encompassed CEST and ^{31}P parameter values, scan intervals, therapy details, country of origin, patient demographics (including age), tumor histologic features, response assessment, MRI field strength, type of CEST contrast, acquisition schemes, acquisition parameters, and the definition of the region of interest (ROI).

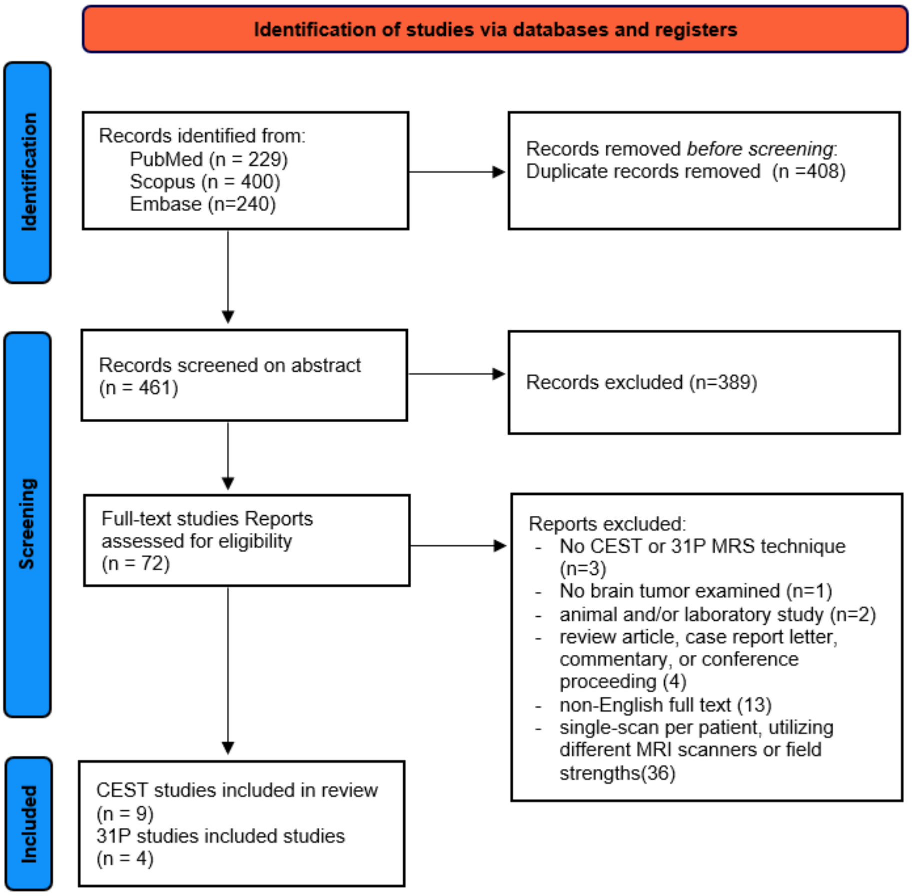

Figure 3: PRISMA flow diagram of the study selection process

3. Results

3.1 Study selection

The systematic search of PubMed, Scopus, and Embase databases yielded 461 unique studies. After screening abstracts, 72 studies met the initial inclusion criteria. Full-text review led to the final inclusion of 13 studies: nine utilizing APT-CEST imaging, involving 229 patients, and four employing ^{31}P MRSI, involving 63 patients (Figure 3). All studies were prospective and observational in design.

3.2 APT-CEST

Three studies assessed the repeatability of APT-CEST on 3T MRI scans, while six studies evaluated therapy responses to chemotherapy (bevacizumab or temozolomide) with or without concurrent radiation therapy across various MRI field strengths (1.5T, 3T, and 7T) (3-10, 50). Most patients included had glioblastoma (WHO grade IV; 181/229). The scanning parameters varied, including saturation strength (0.5 to 6 μT), saturation time (1 to 3 seconds), and frequency offset range, see Table 1. Detailed information is provided in Appendix B.

Repeatability: Three studies evaluated repeatability across different tumor types and WHO grades (5, 8, 50), all reporting high intersession and intrasession intraclass correlation coefficients (ICC) and low coefficients of variation (COV) for tumors (ICC=0.97; 95% CI, 0.82–1.00 (8), COV within session = 2.64 [1.35–7.00] (50)) and normal appearing white matter (NAWM) (0.99; 95% CI, 0.92–1.00 (8); COV within session = 2.62 [0.94–7.08](50)). However, Lee et al. (5) noted greater session variability in pontine lesions, and both Lee et al. (5) and Wu et al. (50) observed better reproducibility within sessions than between sessions.

Diagnostic performance: Six studies found that before starting therapy MTRasym values were significantly higher and MTRamide and MTRnoe values were lower in tumors compared to NAWM (3-8). Chan et al. (2020-2) (4) identified higher MTRnoe and MTRamide values in high-grade tumors than in low-grade tumors, though this distinction was absent when excluding necrotic or resected regions.

Therapy response: Six studies assessed therapy. Three studies with almost all glioblastomas (80/82 patients) reported higher baseline MTRasym values in early progressors compared to responders or late progressors receiving radiation therapy and temozolomide (3, 6, 7). This is consistent with findings from Yao et al. (10) showing higher baseline MTRasym indicative of shorter progression-free survival (PFS) for patients receiving bevacizumab. Early progression was defined as progression within seven months following therapy. Mehrabian et al. (6) also reported increased baseline MTRnoe, MTRamide, MT, and CESTnoe values in progressors, which was not observed in the other studies (3, 7). No significant differences between progression and non-progression groups were observed immediately after therapy (3, 6, 7, 9). Significant increases in MTRnoe and MTRamide were noted in responders to radiation and chemotherapy during early treatment within 2 weeks (4, 6), with a stable or slight increase in MTRnoe at therapy end (7). Park et al. (9) and Yao et al. (10) observed significant decreases in MTRasym in responders to bevacizumab, correlating with longer PFS.

3.3 ^{31}P MRSI

One study evaluated repeatability (15), while three studies assessed therapy response to either temozolomide or bevacizumab (1, 2, 16). Detailed information is provided in Appendix B, with key scanner parameters listed in Table 2. All studies used consistent scanning parameters but with varying voxel sizes (ranging from 5x15x12.5 mm³ to 30x30x25 mm³). All studies focused on glioblastomas (WHO grade IV).

Repeatability: Alcicek et al. (15) found consistent repeatability by comparing scans taken before and after 72 hours of fasting, with consistent full spectral linewidth at the half amplitude of maximum signal (FWHM >0.1 ppm) and no significant differences in relative standard deviation or signal-to-noise ratio.

Diagnostic performance: All studies reported differences in metabolite parameters between tumor and NAWM, with variations in the significant metabolites reported in Table 3. Three studies (2, 15, 16) reported elevated pH values in tumors compared to NAWM.

Therapy response: Three studies assessed changes in metabolites during therapy. Two studies found decreased pH values after bevacizumab treatment (2, 16), with Wenger et al. (16) also noting increased pH during disease progression and no significant changes in NAWM. Hattingen et al. (2) observed increased GPE levels in responders, with no changes in other metabolites. Grams et al. (1) reported increases in PCr/ATP, PCr/Pi, and PDE/ATP ratios, along with decreases in PME/PDE and PME/PCr ratios in tumor tissue after therapy initiation with temozolomide, along with significant metabolic changes in adjacent and contralateral NAWM.

Table 1: MRI protocol details and imaging parameters for different studies of amide proton transfer (APT) chemical exchange saturation transfer (CEST)

		Acquisition	Saturation		Sampling			
Article	**MRI scanner**	**Sequence**	**uT**	**s**	**Steps**	**Range, equal steps**	**Nr of slices**	**Voxel size in mm³**
Chan, 2021 (3)	1,5T Philips	2D imaging pulse sequence	2.5	1.13	64	±6 ppm Yes	1	2.5x2.5x5
Chan 2021-2 (4)	1,5T Philips	2D imaging pulse sequence	2.5	1.13	67	±3,5 ppm No	1	2.5x2.5x5
Lee, 2020 (5)	3T Philips	3D turbo spin echo sequence	2	2.00	7	±4.3 and -1560 No	15	1.8x1.8x5
Mehrabian, 2018(6)	3T Philips	2D fast field echo with multi-shot turbo field echo	0.5	0.97	60	±5.9 ppm Yes	1	1.3x1.3x3
Meissner, 2019 (7)	7T Siemens	2D gradient echo CEST sequence	0.6 & 1.0	2.25	59	± 300 ppm No	3	1.72x1.72x5
Park, 2020 (9)	3T Philips	3D turbo spin-echo sequence	2	2.00	?	?	15	1.11x1.11x5
Wamelink, 2023 (8)	3T Siemens	3D turbo spin echo SPACE APT CEST	2	1.00	7	± 4.0, and 1560 No	85	2.8x2.8x2.8
Wu, 2023 (50)	3T GE	A 3D snapshot CEST image acquisition	1.5	1.60	43	±100 ppm No	14	1.7x1.7 x 3
Yao, 2019 (10)	3T Siemens	2D CEST-EPI or CEST- SAGE-EPI sequence	6	3.00	29	±3,5 ppm No	1	1.9x1.9x4

Table 2: MRI protocol details and imaging parameters for different studies of ³¹P MRSI

Article	Sequence	MRI field strength	TR ms	TE ms	Flip angle (*)	Nr of slices	Thickness mm	Voxel size mm3	Coil
Alcicek, 2024 (15)	3D ³¹P FID CSI sequence WALTZ4 1H decoupling	3T Siemens	2000	2.3	60	multi	12.5	5 x15x12.5	Double-tuned 1H/31P volume head coil
Grams, 2021 (1)	3D sequence with WALTZ 4 proton decoupling	3T Siemens	2000	2.3	60	multi	25	30×30x25	Double-tuned 1H/31P volume head coil
Hattingen, 2011 (2)	3D ³¹P MRSI; WALTZ4 proton decoupling	3T Siemens	2000	2.3	60	multi	25	15×15x25	Double-tuned 1H/31P volume head coil
Wenger, 2017 (16)	3D ³¹P MRSI; WALTZ4 proton decoupling shift imaging (CSI)	3T Siemens	2000	2.3	60	multi	25	15x15x25	Double-tuned 1H/31P volume head coil

Table 3: Metabolite parameters and their values for tumor tissue and normal-appearing white matter (NAWM), with standard deviation.

Study	Tumor value ± SD	NAWM value ± SD
Alcicek, 2024 (15)	pH=7.08 ± 0.05	pH=7.03 ± 0.01
	PME/PDE=0.71 ± 0.41	PME/PDE=0.51 ± 0.16
Grams, 2021 (1)	No absolute values available	No absolute values available
Hattingen, 2011 (2)	pH= 7.11 ± 0.56	pH= 7.04 ± 0.02
	PE/GPE = 2.14 ± 0.75	PE/GPE = 1.75 ± 0.31
	Pi/ATP = 0.94 ± 0.43	Pi/ATP = 0.79 ± 0.26
	PCr = 1.69 ±0.29	PCr = 1.88 ± 0.34
	GPE = 0.24 ± 0.24	GPE = 0.28 ± 0.10
Wenger, 2017 (16)	pHi= 7.110 ± 0.053	pHi = 7.017 ± 0.026

Tumor before therapy compared to NAWM

Difference between MTRamide and MTRnoe removing direct water saturation and magnetization transfer effects

- ↑ MTRasym (3-8)

Sum of all saturation effects at 3.5ppm amide proton

- ↓ MTRamide (3-8)

Sum of all saturation effects at -3.5 ppm nuclear Overhauser effect

- ↑ MTRnoe (3-8)

Responding tumors post-therapy compared to the baseline

Difference between MTRamide and MTRnoe removing direct water saturation and magnetization transfer effects

- ↓ MTRasym (9, 10)

Sum of all saturation effects at 3.5ppm amide proton

- ↑ MTRamide(4, 6, 7)

Sum of all saturation effects at -3.5 ppm nuclear Overhauser effect

- ↑ MTRnoe (4, 6, 7)

Tumor before therapy compared to NAWM

Cell membrane metabolism

- ↑ PME/PDE (1, 2)
- ↑ PE/GPE (2)
- ↑ PME/PCr (1)
- ↓ GPE (2)

Hypoxia markers

- ↑ pH (2, 15, 16)

Energetic state of the cell

- ↓ PCr/ATP (1)
- ↓ PCr/Pi (1)
- ↓ PDE/ATP (1)
- ↓ PCr (2)

ATP turnover

- ↑ Pi/ATP (1, 2)

Responding tumors post-therapy compared to the baseline

Cell membrane metabolism

- ↓ PME/PDE (1)
- \- PE/GPE (2)
- ↓ PME/PCr (1)
- ↑ GPE (2)

Hypoxia markers

- ↓ pH (2, 16)

Energetic state of the cell

- ↑ PCr/ATP (1)
- ↑ PCr/Pi (1)
- ↑ PDE/ATP (1)
- \- PCr (2)

ATP turnover

- \- Pi/ATP (1, 2)

Figure 4: Left: Comparison of metabolites and metabolite ratios between tumor and normal appearing white matter (NAWM) for APT-CEST top row and 31P MRSI bottom row. Right: Changes in tumor metabolites post-therapy compared to baseline for responding tumors for APT-CEST top row and 31P MRSI bottom row.

5. Discussion

This review highlights the potential clinical utility of APT-CEST and ^{31}P MRSI imaging techniques in brain tumors, focusing on their repeatability, diagnostic performance, and therapy response monitoring. While both modalities offer unique insights into brain tumor biology, they differ in their specific applications and findings.

Conventional MRI is essential for diagnosing and monitoring treatment response, though distinguishing between true tumor progression and pseudoprogression, and obtaining a histological diagnosis, remains challenging (10-13). Metabolic MRI has the potential to refine the differential diagnoses and help to differentiate between true tumor progression and pseudoprogression (47). This may reduce the need for invasive biopsies, prevent overtreatment, and enable earlier intervention (25, 26, 30-33).

5.1 APT-CEST

APT-CEST imaging shows high repeatability across various tumor types and grades, which is essential for reliable tumor monitoring. However, session variability in certain anatomical locations, like pontine lesions, underscores the need for careful region of interest (ROI) placement, consistent with Obdeijn's findings in healthy volunteers at 3T (51). Moreover, all studies in this review evaluated repeatability using 3T MRI scanners, but it is known that higher field strengths, like 7T used in the MITCH study (52), suffer from more B0 and B1 field inhomogeneities that could affect repeatability (53). However, other studies also reported excellent reproducibility of inter- and intrasubject APT-CEST at 7T (54, 55). These studies found increased repeatability after correcting for B1 inhomogeneities.

APT-CEST distinguishes tumors from NAWM through higher MTRasym and lower MTRamide/MTRnoe, though this distinction adds little diagnostic value beyond conventional imaging. The technique holds more promise in distinguishing high-grade from low-grade tumors, as shown by a meta-analysis reporting 88% (95% CI, 77–94%) sensitivity and 91% (95% CI, 82–96%) specificity (3, 56), though standardization in ROI placement is needed to fully leverage these capabilities.

In therapy response monitoring, APT-CEST shows potential as an early biomarker for progression. Baseline imaging parameters, such as MTRasym, MTRnoe, and MTRamide, demonstrated predictive value for early progression, consistent with previous studies (32, 33). However, heterogeneity in study populations, therapy regimens, and imaging parameters complicates comparisons. Differences in frequency offsets, saturation strength, and saturation duration highlight the need for standardized imaging protocols. A paper by Zhou et al. (57) aimed to achieve this by standardizing APT imaging in a clinical setting on 3T focusing on brain tumors.

Differences in MRI field strengths have contributed to varied results; Chan et al. (3, 4) found no significant changes using 1.5T MRI, while Meissner et al. (7) detected significant changes at 7T MRI, likely due to the higher signal-to-noise ratio achievable at 7 Tesla. These factors underscore the need for larger, multicenter studies to validate the clinical utility of APT-CEST across diverse settings and patient populations.

5.2 ^{31}P MRSI

^{31}P MRSI demonstrates the potential in monitoring metabolic changes and therapy response in brain tumors. Alcicek et al. (15) confirmed its repeatability at 3T MRI, and similar studies in other tissues have shown reliable repeatability at 7T MRI (58-61).

The included studies only assessed glioblastoma, a tumor with mitochondrial dysfunction leading to the preference for glycolysis over oxidative phosphorylation and decreased ATP production (62). Key metabolic markers assessed included PME/PDE, Pe/GPE, and PME/PCr, which reflect increased cell membrane metabolism, decreased energetic states (PCr/ATP, PCr/Pi), and heightened ATP turnover (Pi/ATP), summarized in Table 4.

These markers, in response to treatments with bevacizumab and temozolomide, show a reduction in hypoxia markers and an improvement in energetic states, offering a potential window for early therapy monitoring. Additionally, changes in pH during disease progression (2, 16) provide insight into tumor aggressiveness, consistent with findings linking higher pH to more aggressive gliomas (41, 63).

Despite these promising results, variability in the metabolic ratios used across studies complicates direct comparisons, emphasizing the need for standardized approaches. The observed changes in NAWM and areas beyond the tumor region suggest that ^{31}P MRSI may also capture the broader effects of brain tumors and their treatment, providing a more comprehensive picture of the disease process.

However, technical challenges such as low signal-to-noise ratio (SNR), coarse spatial resolution, and long acquisition times, limit its clinical applicability (48). For instance, in Alcicek et al. (15) nine out of 22 patients were excluded due to poor spectral quality.

A limitation of this review is that the most statistically significant results came from Grams et al. (1), who compared multiple regions and metabolites without applying statistical corrections. Additionally, their use of large voxel sizes raises concerns about the reliability of the findings due to the partial volume effect.

While ^{31}P MRSI can offer valuable metabolic insights, the general clinical applicability requires further optimization and validation.

5.3 Potential application in pediatric brain cancer

Pediatric brain cancer, alongside leukemia, is one of the most prevalent and fatal cancers affecting children (64, 65). These tumors differ significantly from those in adults, predominantly occurring in the posterior fossa and presenting distinct molecular subtypes and pathology (66, 67). Most pediatric brain tumors are low-grade gliomas (LGG), classified as WHO grade 1, with a 10-year overall survival rate of 90% (66, 68, 69). In contrast, the majority of tumors reviewed in this study were high-grade, with an overall survival of nine months (70).

APT-CEST imaging offers several advantages for pediatric patients, particularly by eliminating the need for intravenous gadolinium contrast. Obtaining intravenous access is invasive, causing discomfort and posing risks such as phlebitis, occlusion, and infection (71). Gadolinium use carries risks of hypersensitivity reactions, including erythema, exanthema, urticaria, angioedema, and respiratory symptoms such as bronchospasm, though these reactions are infrequent (72).

Preliminary studies, including Zhang et al. (73), suggest that APT-CEST can distinguish between high- and low-grade tumors in pediatric patients, similar to findings in adults (46). Obdeijn (51) also observed differences across various tumor types. Early results from 7T APTw imaging in pediatric brain tumors demonstrate its feasibility, with longitudinal APTw changes exceeding intrasubject variability in several cases (51). APTw imaging shows particular promise for tumors with indolent courses, such as optic pathway gliomas, where conventional MRI might not adequately reflect changes in tumor status (19, 47). Moreover, APT-CEST holds promise for other pediatric CNS diseases, offering non-invasive metabolic insights and potentially reducing the use of contrast agents (67). However, further research is required to validate its efficacy in children and establish standardized imaging protocols.

5.4 APT-CEST and ^{31}P: Clinical, Economic, and Environmental Benefits

Using gadolinium contrast agents is invasive and poses risks related to intravenous access and hypersensitivity reactions (71, 72). Reducing the use of these agents directly benefits patients by minimizing these risks and avoiding potential adverse effects. While APT-CEST and ^{31}P MRSI are not yet ready for routine clinical use and require post-processing and specialized expertise, their application could significantly improve patient quality of life by identifying ineffective therapies early, thereby minimizing exposure to the side effects of unnecessary treatments. Furthermore, this approach could provide substantial economic benefits, as standard therapies can cost between €15,000 and €30,000 per patient, with pediatric cases potentially reaching hundreds of thousands or even millions of euros (74, 75).

Separately, reducing gadolinium usage also offers environmental advantages. Gadolinium is excreted through urine and can accumulate in water bodies, particularly near urban areas, posing risks to aquatic ecosystems due to its toxicity at higher concentrations. Gadolinium is environmentally persistent, raising concerns about its long-term ecological impact and potential effects on human health through water contamination (76)

5.5 Future recommendations

For APT-CEST and ^{31}P MRSI to become clinically viable, several key steps are necessary. First, imaging protocols, post-processing analysis, and signal intensity values need standardization across institutions. This standardization will reduce variability and improve comparability between studies. Second, larger, multicenter studies should be conducted to validate these imaging techniques' findings and establish robust biomarkers for diagnosis, therapy response, and prognosis.

Additionally, research should explore the potential applications of these techniques in pediatric brain cancer, as the unique tumor biology in children may yield different findings from those in adults (66). Given the significant advancements in MRI technology and the increasing understanding of tumor biology, both APT-CEST and ^{31}P MRSI hold substantial promise for the future of brain tumor imaging.

6. Conclusion

This review underscores the potential of APT-CEST and ^{31}P MRSI imaging techniques in enhancing the clinical management of brain tumors. Both modalities offer unique insights into tumor biology, However, challenges such as variability in imaging protocols and technical limitations must be addressed to fully realize their clinical potential. Future research should focus on standardizing imaging procedures, validating findings through larger multicenter studies, and exploring applications in pediatric brain cancer. Advancing these techniques could significantly improve diagnostic accuracy, therapy monitoring, and overall patient outcomes.

7. References

1. Grams AE, Mangesius S, Steiger R, Radovic I, Rietzler A, Walchhofer LM, et al. Changes in Brain Energy and Membrane Metabolism in Glioblastoma following Chemoradiation. Curr Oncol. 2021;28(6):5041-53.
2. Hattingen E, Jurcoane A, Bähr O, Rieger J, Magerkurth J, Anti S, et al. Bevacizumab impairs oxidative energy metabolism and shows antitumoral effects in recurrent glioblastomas: a 31P/1H MRSI and quantitative magnetic resonance imaging study. Neuro Oncol. 2011;13(12):1349-63.
3. Chan RW, Chen H, Myrehaug S, Atenafu EG, Stanisz GJ, Stewart J, et al. Quantitative CEST and MT at 1.5T for monitoring treatment response in glioblastoma: early and late tumor progression during chemoradiation. J Neurooncol. 2021;151(2):267-78.
4. Chan RW, Lawrence LSP, Oglesby RT, Chen H, Stewart J, Theriault A, et al. Chemical exchange saturation transfer MRI in central nervous system tumours on a 1.5 T MR-Linac. Radiotherapy and Oncology. 2021;162:140-9.
5. Lee JB, Park JE, Jung SC, Jo Y, Kim D, Kim HS, et al. Repeatability of amide proton transfer-weighted signals in the brain according to clinical condition and anatomical location. Eur Radiol. 2020;30(1):346-56.
6. Mehrabian H, Myrehaug S, Soliman H, Sahgal A, Stanisz GJ. Evaluation of Glioblastoma Response to Therapy With Chemical Exchange Saturation Transfer. Int J Radiat Oncol Biol Phys. 2018;101(3):713-23.
7. Meissner JE, Korzowski A, Regnery S, Goerke S, Breitling J, Floca RO, et al. Early response assessment of glioma patients to definitive chemoradiotherapy using chemical exchange saturation transfer imaging at 7 T. J Magn Reson Imaging. 2019;50(4):1268-77.
8. Wamelink I, Kuijer JPA, Padrela BE, Zhang Y, Barkhof F, Mutsaerts H, et al. Reproducibility of 3 T APT-CEST in Healthy Volunteers and Patients With Brain Glioma. J Magn Reson Imaging. 2023;57(1):206-15.

9. Park JE, Kim HS, Park SY, Jung SC, Kim JH, Heo HY. Identification of Early Response to Anti-Angiogenic Therapy in Recurrent Glioblastoma: Amide Proton Transfer-weighted and Perfusion-weighted MRI compared with Diffusion-weighted MRI. Radiology. 2020;295(2):397-406.
10. Yao J, Tan CHP, Schlossman J, Chakhoyan A, Raymond C, Pope WB, et al. pH-weighted amine chemical exchange saturation transfer echoplanar imaging (CEST-EPI) as a potential early biomarker for bevacizumab failure in recurrent glioblastoma. J Neurooncol. 2019;142(3):587-95.
11. Sartoretti E, Sartoretti T, Wyss M, Reischauer C, van Smoorenburg L, Binkert CA, et al. Amide proton transfer weighted (APTw) imaging based radiomics allows for the differentiation of gliomas from metastases. Sci Rep. 2021;11(1):5506.
12. Novak J, Wilson M, Macpherson L, Arvanitis TN, Davies NP, Peet AC. Clinical protocols for ^{31}P MRS of the brain and their use in evaluating optic pathway gliomas in children. Eur J Radiol. 2014;83(2):e106-12.
13. Bondy ML, Scheurer ME, Malmer B, Barnholtz-Sloan JS, Davis FG, Il'yasova D, et al. Brain tumor epidemiology: consensus from the Brain Tumor Epidemiology Consortium. Cancer. 2008;113(7 Suppl):1953-68.
14. Ilic I, Ilic M. International patterns and trends in the brain cancer incidence and mortality: An observational study based on the global burden of disease. Heliyon. 2023;9(7):e18222.
15. Alcicek S, Divé I, Thomas DC, Prinz V, Forster MT, Czabanka M, et al. 2D 1H sLASER Long-TE and 3D 31P Chemical Shift Imaging at 3 T for Monitoring Fasting-Induced Changes in Brain Tumor Tissue. Journal of Magnetic Resonance Imaging. 2024.
16. Wenger KJ, Hattingen E, Franz K, Steinbach JP, Bähr O, Pilatus U. Intracellular pH measured by (31) P-MR-spectroscopy might predict site of progression in recurrent glioblastoma under antiangiogenic therapy. J Magn Reson Imaging. 2017;46(4):1200-8.
17. Leao DJ, Craig PG, Godoy LF, Leite CC, Policeni B. Response Assessment in Neuro-Oncology Criteria for Gliomas: Practical Approach Using Conventional and Advanced Techniques. AJNR Am J Neuroradiol. 2020;41(1):10-20.
18. de Wit MC, de Bruin HG, Eijkenboom W, Sillevis Smitt PA, van den Bent MJ. Immediate post-radiotherapy changes in malignant glioma can mimic tumor progression. Neurology. 2004;63(3):535-7.
19. Brandsma D, Stalpers L, Taal W, Sminia P, van den Bent MJ. Clinical features, mechanisms, and management of pseudoprogression in malignant gliomas. Lancet Oncol. 2008;9(5):453-61.
20. Chamberlain MC, Glantz MJ, Chalmers L, Van Horn A, Sloan AE. Early necrosis following concurrent Temodar and radiotherapy in patients with glioblastoma. J Neurooncol. 2007;82(1):81-3.
21. Cairncross JG, Pexman JH, Rathbone MP, DelMaestro RF. Postoperative contrast enhancement in patients with brain tumor. Ann Neurol. 1985;17(6):570-2.
22. da Cruz LCH, Kimura M. Chapter 27 - Diffusion Magnetic Resonance Imaging in Brain Tumors. In: Newton HB, editor. Handbook of Neuro-Oncology Neuroimaging (Second Edition). San Diego: Academic Press; 2016. p. 273-300.
23. Wu B, Warnock G, Zaiss M, Lin C, Chen M, Zhou Z, et al. An overview of CEST MRI for non-MR physicists. EJNMMI Phys. 2016;3(1):19.
24. van Zijl PC, Yadav NN. Chemical exchange saturation transfer (CEST): what is in a name and what isn't? Magn Reson Med. 2011;65(4):927-48.
25. Jones CK, Schlosser MJ, van Zijl PC, Pomper MG, Golay X, Zhou J. Amide proton transfer imaging of human brain tumors at 3T. Magn Reson Med. 2006;56(3):585-92.
26. Park JE, Kim HS, Park KJ, Choi CG, Kim SJ. Histogram Analysis of Amide Proton Transfer Imaging to Identify Contrast-enhancing Low-Grade Brain Tumor That Mimics High-Grade Tumor: Increased Accuracy of MR Perfusion. Radiology. 2015;277(1):151-61.
27. Togao O, Yoshiura T, Keupp J, Hiwatashi A, Yamashita K, Kikuchi K, et al. Amide proton transfer imaging of adult diffuse gliomas: correlation with histopathological grades. Neuro Oncol. 2014;16(3):441-8.
28. Zhao X, Wen Z, Zhang G, Huang F, Lu S, Wang X, et al. Three-dimensional turbo-spin-echo amide proton transfer MR imaging at 3-Tesla and its application to high-grade human brain tumors. Mol Imaging Biol. 2013;15(1):114-22.
29. Zhou J, Zhu H, Lim M, Blair L, Quinones-Hinojosa A, Messina SA, et al. Three-dimensional amide proton transfer MR imaging of gliomas: Initial experience and comparison with gadolinium enhancement. J Magn Reson Imaging. 2013;38(5):1119-28.
30. Jiang S, Yu H, Wang X, Lu S, Li Y, Feng L, et al. Molecular MRI differentiation between primary central nervous system lymphomas and high-grade gliomas using endogenous protein-based amide proton transfer MR imaging at 3 Tesla. Eur Radiol. 2016;26(1):64-71.
31. Mehrabian H, Desmond KL, Soliman H, Sahgal A, Stanisz GJ. Differentiation between Radiation Necrosis and Tumor Progression Using Chemical Exchange Saturation Transfer. Clin Cancer Res. 2017;23(14):3667-75.
32. Park KJ, Kim HS, Park JE, Shim WH, Kim SJ, Smith SA. Added value of amide proton transfer imaging to conventional and perfusion MR imaging for evaluating the treatment response of newly diagnosed glioblastoma. Eur Radiol. 2016;26(12):4390-403.

33. Harris RJ, Cloughesy TF, Liau LM, Prins RM, Antonios JP, Li D, et al. pH-weighted molecular imaging of gliomas using amine chemical exchange saturation transfer MRI. Neuro Oncol. 2015;17(11):1514-24.
34. Podo F. Tumour phospholipid metabolism. NMR Biomed. 1999;12(7):413-39.
35. Korzowski A, Weinfurtner N, Mueller S, Breitling J, Goerke S, Schlemmer HP, et al. Volumetric mapping of intra- and extracellular pH in the human brain using (31) P MRSI at 7T. Magn Reson Med. 2020;84(4):1707-23.
36. Mirkes C, Shajan G, Chadzynski G, Buckenmaier K, Bender B, Scheffler K. (31)P CSI of the human brain in healthy subjects and tumor patients at 9.4 T with a three-layered multi-nuclear coil: initial results. Magma. 2016;29(3):579-89.
37. Liu Y, Gu Y, Yu X. Assessing tissue metabolism by phosphorous-31 magnetic resonance spectroscopy and imaging: a methodology review. Quant Imaging Med Surg. 2017;7(6):707-26.
38. Santos-Díaz A, Noseworthy MD. Phosphorus magnetic resonance spectroscopy and imaging (31P-MRS/MRSI) as a window to brain and muscle metabolism: A review of the methods. Biomedical Signal Processing and Control. 2020;60:101967.
39. Korzowski A, Weckesser N, Franke VL, Breitling J, Goerke S, Schlemmer HP, et al. Mapping an Extended Metabolic Profile of Gliomas Using High-Resolution (31)P MRSI at 7T. Front Neurol. 2021;12:735071.
40. Paech D, Weckesser N, Franke VL, Breitling J, Görke S, Deike-Hofmann K, et al. Whole-Brain Intracellular pH Mapping of Gliomas Using High-Resolution (31)P MR Spectroscopic Imaging at 7.0 T. Radiol Imaging Cancer. 2024;6(1):e220127.
41. Ha DH, Choi S, Oh JY, Yoon SK, Kang MJ, Kim KU. Application of 31P MR spectroscopy to the brain tumors. Korean J Radiol. 2013;14(3):477-86.
42. Albers MJ, Krieger MD, Gonzalez-Gomez I, Gilles FH, McComb JG, Nelson MD, Jr., et al. Proton-decoupled 31P MRS in untreated pediatric brain tumors. Magn Reson Med. 2005;53(1):22-9.
43. Aseel A, McCarthy P, Mohammed A. Brain magnetic resonance spectroscopy to differentiate recurrent neoplasm from radiation necrosis: A systematic review and meta-analysis. J Neuroimaging. 2023;33(2):189-201.
44. Maldonado X, Alonso J, Giralt J, Cucurella MG, del Campo JM, Rovira A, et al. 31Phosphorus magnetic resonance spectroscopy in the assessment of head and neck tumors. Int J Radiat Oncol Biol Phys. 1998;40(2):309-12.
45. Hoekstra HJ, Boeve WJ, Kamman RL, Mooyaart EL. Clinical applicability of human in vivo localized phosphorus-31 magnetic resonance spectroscopy of bone and soft tissue tumors. Ann Surg Oncol. 1994;1(6):504-11.
46. Okuchi S, Hammam A, Golay X, Kim M, Thust S. Endogenous Chemical Exchange Saturation Transfer MRI for the Diagnosis and Therapy Response Assessment of Brain Tumors: A Systematic Review. Radiol Imaging Cancer. 2020;2(1):e190036.
47. Dagher R, Gad M, da Silva de Santana P, Sadeghi MA, Yewedalsew SF, Gujar SK, et al. Umbrella review and network meta-analysis of diagnostic imaging test accuracy studies in Differentiating between brain tumor progression versus pseudoprogression and radionecrosis. J Neurooncol. 2024;166(1):1-15.
48. El-Abtah ME, Talati P, Dietrich J, Gerstner ER, Ratai EM. Magnetic resonance spectroscopic imaging for detecting metabolic changes in glioblastoma after anti-angiogenic therapy-a systematic literature review. Neurooncol Adv. 2022;4(1):vdac103.
49. Ouzzani M, Hammady H, Fedorowicz Z, Elmagarmid A. Rayyan—a web and mobile app for systematic reviews. Systematic Reviews. 2016;5(1):210.
50. Wu Y, Wood TC, Derks S, Pruis IJ, van der Voort S, van Zanten S, et al. Reproducibility of APT-weighted CEST-MRI at 3T in healthy brain and tumor across sessions and scanners. Sci Rep. 2023;13(1):18115.
51. Obdeijn IV. APTw imaging in paediatric brain tumours: no waste of time and energy: University Of Twente; 2021.
52. Utrecht UMC. Onderzoek naar de mogelijkheid om het metabolisme van een hersentumor bij kinderen te karakteriseren met behulp van MRI met een hoge veldsterkte. [Trial]. In press 2020.
53. Pinho Meneses B, Stockmann JP, Arango N, Gapais P-F, Giacomini E, Mauconduit F, et al. Shim coils tailored for correcting B0 inhomogeneity in the human brain (SCOTCH): Design methodology and 48-channel prototype assessment in 7-Tesla MRI. NeuroImage. 2022;261:119498.
54. Benyard B, Nanga RPR, Wilson NE, Thakuri D, Jacobs PS, Swain A, et al. In vivo reproducibility of 3D relayed NOE in the healthy human brain at 7 T. Magn Reson Med. 2023;89(6):2295-304.
55. Mennecke A, Khakzar KM, German A, Herz K, Fabian MS, Liebert A, et al. 7 tricks for 7 T CEST: Improving the reproducibility of multipool evaluation provides insights into the effects of age and the early stages of Parkinson's disease. NMR Biomed. 2023;36(6):e4717.
56. Suh CH, Park JE, Jung SC, Choi CG, Kim SJ, Kim HS. Amide proton transfer-weighted MRI in distinguishing high- and low-grade gliomas: a systematic review and meta-analysis. Neuroradiology. 2019;61(5):525-34.
57. Zhou J, Zaiss M, Knutsson L, Sun PZ, Ahn SS, Aime S, et al. Review and consensus

recommendations on clinical APT-weighted imaging approaches at 3T: Application to brain tumors. Magn Reson Med. 2022;88(2):546-74.
58. Seelen LWF, van den Wildenberg L, Gursan A, Froeling M, Gosselink M, van der Kemp WJM, et al. (31) P MR Spectroscopy in the Pancreas: Repeatability, Comparison With Liver, and Pilot Pancreatic Cancer Data. J Magn Reson Imaging. 2024.
59. van der Kemp WJ, Stehouwer BL, Boer VO, Luijten PR, Klomp DW, Wijnen JP. Proton and phosphorus magnetic resonance spectroscopy of the healthy human breast at 7 T. NMR Biomed. 2017;30(2).
60. van den Wildenberg L, Gursan A, Seelen LWF, van der Velden TA, Gosselink M, Froeling M, et al. In vivo phosphorus magnetic resonance spectroscopic imaging of the whole human liver at 7 T using a phosphorus whole-body transmit coil and 16-channel receive array: Repeatability and effects of principal component analysis-based denoising. NMR Biomed. 2023;36(5):e4877.
61. Jonuscheit M, Wierichs S, Rothe M, Korzekwa B, Mevenkamp J, Bobrov P, et al. Reproducibility of absolute quantification of adenosine triphosphate and inorganic phosphate in the liver with localized (31)P-magnetic resonance spectroscopy at 3-T using different coils. NMR Biomed. 2024;37(8):e5120.
62. Guntuku L, Naidu VG, Yerra VG. Mitochondrial Dysfunction in Gliomas: Pharmacotherapeutic Potential of Natural Compounds. Curr Neuropharmacol. 2016;14(6):567-83.
63. Bulakbasi N, Kocaoglu M, Sanal HT, Tayfun C. Efficacy of in vivo 31Phosphorus Magnetic Resonance Spectroscopy in Differentiation and Staging of Adult Human Brain Tumors. Neuroradiol J. 2007;20(6):646-55.
64. Ostrom QT, Gittleman H, Xu J, Kromer C, Wolinsky Y, Kruchko C, et al. CBTRUS Statistical Report: Primary Brain and Other Central Nervous System Tumors Diagnosed in the United States in 2009-2013. Neuro Oncol. 2016;18(suppl_5):v1-v75.
65. Global, regional, and national burden of brain and other CNS cancer, 1990-2016: a systematic analysis for the Global Burden of Disease Study 2016. Lancet Neurol. 2019;18(4):376-93.
66. Greuter L, Guzman R, Soleman J. Pediatric and Adult Low-Grade Gliomas: Where Do the Differences Lie? Children (Basel). 2021;8(11).
67. Zhang H, Zhou J, Peng Y. Amide Proton Transfer–Weighted MR Imaging of Pediatric Central Nervous System Diseases. Magnetic Resonance Imaging Clinics of North America. 2021;29(4):631-41.
68. Udaka YT, Packer RJ. Pediatric Brain Tumors. Neurol Clin. 2018;36(3):533-56.
69. de Blank P, Bandopadhayay P, Haas-Kogan D, Fouladi M, Fangusaro J. Management of pediatric low-grade glioma. Curr Opin Pediatr. 2019;31(1):21-7.
70. Brown NF, Ottaviani D, Tazare J, Gregson J, Kitchen N, Brandner S, et al. Survival Outcomes and Prognostic Factors in Glioblastoma. Cancers (Basel). 2022;14(13).
71. Indarwati F, Mathew S, Munday J, Keogh S. Incidence of peripheral intravenous catheter failure and complications in paediatric patients: Systematic review and meta analysis. International Journal of Nursing Studies. 2020;102.
72. Gracia Bara MT, Gallardo-Higueras A, Moreno EM, Laffond E, Muñoz Bellido FJ, Martin C, et al. Hypersensitivity to Gadolinium-Based Contrast Media. Front Allergy. 2022;3:813927.
73. Zhang H, Yong X, Ma X, Zhao J, Shen Z, Chen X, et al. Differentiation of low- and high-grade pediatric gliomas with amide proton transfer imaging: added value beyond quantitative relaxation times. Eur Radiol. 2021;31(12):9110-9.
74. Nederland Z. Veelbelovende zorg - Op de zorglocatie geproduceerde CD19 CAR T-celtherapie bij patiënten met een recidief of refractair DLBCL 2020 [Available from: https://www.zorginstituutnederland.nl/werkagenda/kanker/veelbelovende-zorg-cd19-car-t-celtherapie#:~:text=CAR%20T%2Dceltherapie%20wordt%20sinds,stelt%20kankercellen%20onschadelijk%20te%20maken.
75. zorg Ve. Kanker | Zorguitgaven VZinfo2019 [Available from: https://www.vzinfo.nl/kanker/zorguitgaven.
76. Dekker HM, Stroomberg GJ, Van der Molen AJ, Prokop M. Review of strategies to reduce the contamination of the water environment by gadolinium-based contrast agents. Insights into Imaging. 2024;15(1):62.

Appendix A: Detailed search strategy

Search performed 13-06-2024

Pubmed – 229 articles

Phosphorus-31 – 38 articles

((Neoplasms, Neuroepithelial[MeSH] OR Glioma[tiab] OR brain tumo*[tiab] OR brain cancer[tiab] OR brain metastasis[tiab]) AND (P MRS[tiab] OR P MR spectroscopy[tiab] OR P Magnetic Resonance spectroscopy[tiab] OR P MRSI[tiab] OR 31 P spectroscopy[tiab] OR Phosphorus 31 MR Spectroscopy[tiab] OR 31P Magnetic Resonance Spectroscopy[tiab] OR 31P MR Spectroscopy[tiab] OR 31p/1H MRSI [tiab] OR 31p-1H MRSI [tiab]) AND Humans[Mesh])

Amide Proton Transfer chemical exchange saturation -- after filtering from 2018, 191 articles

(Neoplasms, Neuroepithelial[MeSH] OR Glioma[tiab] OR brain tumo*[tiab] OR brain cancer[tiab] OR brain metastasis[tiab]) AND ((magnetic resonance imaging[MeSH Terms] AND CEST[tiab]) OR chemical exchange saturation transfer[tiab] OR APT[tiab] OR amide proton transfer[tiab] OR magnetization transfer[tiab] OR z-spectrum[tiab] OR chemical exchange[tiab] OR exchange transfer[tiab] OR saturation transfer[tiab]) AND Humans[Mesh]

Scopus – 400 articles

Phosphorus-31 – 69 articles

Article title, Abstract, Keywords ((neuroepithelial AND neoplasms) OR glioma OR "brain tumo*" OR "brain cancer" OR "brain metastasis")

AND

Article title, Abstract, Keywords ("31P-MRS" OR "P MR spectroscopy" OR "P Magnetic Resonance spectroscopy" OR "31P MRSI" OR "31P spectroscopy" OR "Phosphorus-31 MR Spectroscopy" OR "31P Magnetic Resonance Spectroscopy" OR "31P-MR Spectroscopy" OR "31p/1H MRSI" OR "31p-1H MRSI")

AND

All fields (humans)

Amide Proton Transfer chemical exchange saturation – 331 articles

Article title, Abstract, Keywords ((neuroepithelial AND neoplasms) OR glioma OR "brain tumo*" OR "brain cancer" OR "brain metastasis")

AND

Article title, Abstract, Keywords (("magnetic resonance imaging" AND cest) OR "chemical exchange saturation transfer" OR apt OR "amide proton transfer" OR "magnetization transfer" OR "z-spectrum" OR "chemical exchange" OR "exchange transfer" OR "saturation transfer")

AND

All fields (humans)

Filter: Limit 2018-2024

Embase – 240 articles

1. 'neuroepithelial neoplasm'/exp OR glioma:ti,ab OR 'brain tumor*':ti,ab OR 'brain cancer':ti,ab OR 'brain metastasis':ti,ab
2. 'p-mrs':ti,ab OR 'p mr spectroscopy':ti,ab OR 'p magnetic resonance spectroscopy':ti,ab OR 'p-mrsi':ti,ab OR 'p-spectroscopy':ti,ab OR 'phosphorus-31 mr spectroscopy':ti,ab OR '31p magnetic resonance spectroscopy':ti,ab OR '31p-mr spectroscopy':ti,ab OR ‘31p/1H MRSI’:ti,ab OR ‘31p-1H MRSI’:ti,ab)
3. 'magnetic resonance imaging'/exp AND CEST:ti,ab
4. 'chemical exchange saturation transfer':ti,ab OR APT:ti,ab OR 'amide proton transfer':ti,ab OR 'magnetization transfer':ti,ab OR 'z-spectrum':ti,ab OR 'chemical exchange':ti,ab OR 'exchange transfer':ti,ab OR 'saturation transfer':ti,ab

31P MRSI – 35 articles

5. 1 AND 2
6. Limit 5 to human

APT CEST – 205

5. 1 AND (3 OR 4)
6. Limit 5 to human AND Date 2018-2024

Appendix B: Detailed information for all included studies

Table 1: Detailed information on the included Amide Proton Transfer (APT) Chemical Exchange Saturation Transfer (CEST) studies.

Article	Goals	Country	Patients	Median age in years (range)	Scan interval & therapy	ROI	Tumor histologic features	Parameters	Response assessment
Chan, 2021	Assess CEST feasibility in GBM at 1.5T; compare early vs. late progression.	Canada	51 (22 female)	56 (19-68)	Pre-radiation, fractions 10 & 20, 1-month post-radiation; in combination with temozolomide.	Tumor GTV, CTV(=GTV+ 1,5cm), cNAWM	Glioblastoma (51)	MT, MTRasym, MTRamide	Early (<7m) progression vs. late progression (>7m) progression by RANO.
Chan 2021-2	Implement CEST on 1.5T MR-Linac; assess signal changes vs. tumor grade.	Canada	54 (25 female)	54 (26-81)	Pre-radiation, weekly during radiation (6, 3, or 1 time(s)); in combination with chemotherapy.	Tumor GTV, NAWM	Glioblastoma (28), Astrocytoma (10), brain metastasis (7), Oligodendroglioma (3), Ependymoma (1), Schwannoma (1)	MTRasym, MTRamide, MTRNOE	-
Lee, 2020	Assess the repeatability of APTw MRI in the brain across conditions and locations.	South Korea	15 (10 female)	54.6 ± 11.3	Two scans per session, one week apart.	T2 enhancing tumor, cNAWM	Low-grade glioma (6), High-grade glioma (9)	MTRasym	-
Mehrabian, 2018	Monitor CEST changes during chemoradiation; identify earliest response time.	Canada	19 (6 female)	55	Pre-radiation, at 2 and 4 weeks, 1-month post-treatment; in combination with temozolomide.	GD-enhanced tumor, initial GTV, cNAWM	Glioblastoma (19)	MTRamide, MTRnoe, APT, direct effect	Progression/non-progression 3-8m post-therapy assessed with RANO
Meissner, 2019	Assess if CEST MRI enables early chemoradiation response evaluation in glioma.	Germany	12 (5 female)	56± 18	Pre-radiation, 1-week post-radiation, 6 weeks post-radiation; in combination with temozolomide.	Not described	Glioblastoma WHO IV (10), oligodendroglioma WHO II (1), Astrocytoma WHO II (1)	rNOE, dnsAPT, Cho/NAA	Response/progression by MRI, neuro evaluation at 1 & 3 months.
Park, 2020	Predict response and evaluate changes to antiangiogenic treatment in recurrent glioblastoma.	Korea	54 (30 female)	56 (49-64)	Baseline, 6 weeks post-bevacizumab.	FLAIR enhanced tumor, cNAWM	Glioblastoma (54), IDH wildtype (49), IDH mutation (5)	ADC (from DWI), APTw, nCBV (from DSC)	Progression at 12m; PFS until progression/death.

Wamelink, 2023	Test reproducibility of APT-CEST with a clinically feasible scan time in healthy tissue and glioma at 3T.	Netherlands	6 (3 female)	50 ± 17	Two scans in one session, repositioning between scans.	Gd or FLAIR enhanced tumor, cNAWM	Glioblastoma (4), oligodendroglioma (1)	MTRasym	-
Wu, 2023	Evaluate APT-weighted CEST reproducibility across sessions and scanners.	Netherlands	7 (1 female)	69 (57-73)	Two scans in one session, one after 4 days.	Gd enhancing tumor, cNAWM	Glioblastoma (4), lung metastasis (2), oligodendroglioma	MTRasym, MTRrex, Lorentzian difference	-
Yao, 2019	Assess treatment response in recurrent glioblastoma with bevacizumab and pH-weighted APT-CEST.	United States	11 (2 female)	55 (29-75)	Pre- and post-bevacizumab treatment.	Gd or FLAIR enhancing tumor	Recurrent glioblastoma (11)	MTRasym	PFS from the start of treatment; progression defined as >25% increase/new lesion.

Table 2: Detailed information of the included 31 phosphorous Magnetic Resonance Spectroscopic Imaging (MRSI). RANO = Response assessment in neuro-oncology, NAWM=Normal appearing white matter, CE= Contrast-enhanced, FWHM= Full width at half maximum, SNR= Signal-to-noise ratio, SD= Standard deviation, PME= Phospho-mono ester, PDE= Phospho-di ester, ATP= Adenosine triphosphate, PCr= Phosphocreatine, Pi= Inorganic phosphate, PCho= Phosphocholine, GPC= Glycerophosphocholine, GPE= Glycerophosphoethanolamine, PEth= Phosphatidylethanols,

Article	**Goals**	**Country**	**Patients**	**Median age in years (range)**	**Scan interval and therapy**	**ROI**	**Tumor histology**	**Parameters**	**Response assessment**
Alcicek, 2024	Feasibility, reliability, and repeatability of a multi-voxel, multi-nuclei (1 H/31 P) MRSI protocol	Germany	13 (6 female)	61	Baseline, +72h fasting	CE tumor, NAWM	WHO grade II-IV adult type diffuse gliomas	FWHM, SNR, SD, pHi, PME/PDE, ATP/PCr	Biopsy or resection
Grams, 2021	Investigate energy and membrane metabolism with bevacizumab for glioblastomas	Austria	20 (7 female)	63 (36-77)	Baseline, +4m temozolomide	CE tumor, adjacent tumor, NAWM (ipsilateral and contralateral)	Glioblastoma	PCr/ATP, PCr/Pi, Pi/ATP, PME/PDE, PME/PCr, PDE/ATP	Neuroradiologist according to RANO
Hattingen, 2011	Energy metabolism after bevacizumab treatment	Germany	16 (5 female)	50 (30-68)	Baseline, +2m bevacizumab	CE tumor, NAWM	Recurrent glioblastoma	Pi/PCr, Pi/ATP, PCho/GPC, PEth/GPE, pHi, Pi, ATP, PCr, GPE, PEth, GPC, PCho	Neuroradiologist according to RANO
Wenger, 2017	Detect pH changes before structural changes in brain tumors	Germany	14 (3 female)	51(31-67)	Baseline, +2m bevacizumab until further progression	CE tumor, NAWM	Glioblastoma (not methylated(9) methylated(5))	pHi	Neuroradiologist according to RANO

B

^{31}P-MRSI Pipeline

The ^{31}P-MRSI Pipeline with bellow the Matlab code for Phase correction and interpolation

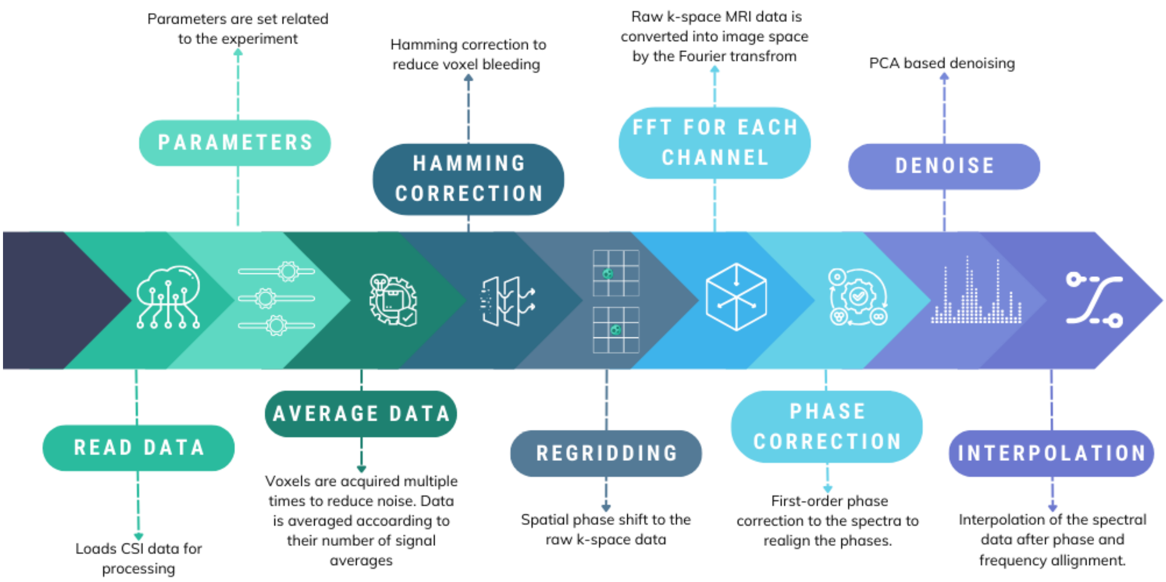

Figure B.1: ^{31}P-MRSI Pipeline for Chemical Shift Imaging (CSI) experiments with multichannel acquisition made in a Philips scanner (7T). In the process of analyzing ^{31}P-MRSI data, either phase correction or interpolation was applied, but not both. PCA = Principal Component Analysis.

```
function [spectrum_voxelshift_kspace] = VoxelShiftKSpace(k_space_data,voxel_shift_RL,
    voxel_shift_AP, voxel_shift_FH)
    %% This function applies a voxel shift in k-space by introducing a phase shift.
    % The shift is applied along three spatial directions:
    % - Right-Left (RL)
    % - Anterior-Posterior (AP)
    % - Feet-Head (FH)
    %
    % Author: Hilde Roording
    %
    % Inputs:
    % - k_space_data: 4D complex array of k-space data (spectral dimension x spatial
        dimensions)
    % - voxel_shift_RL: Shift in voxel units along the Right-Left direction
    % - voxel_shift_AP: Shift in voxel units along the Anterior-Posterior direction
    % - voxel_shift_FH: Shift in voxel units along the Feet-Head direction
    %
    % Output:
    % - spectrum_voxelshift_kspace: 4D complex array with voxel shift applied in k-space

    [dimx, dimy, dimz] = size(k_space_data, [2, 3, 4]);
    [x, y, z] = meshgrid(1:dimy, 1:dimx, 1:dimz);  % Grids for x, y, z voxel dimensions

    %Compute phase shifts based on voxel shifts
    % Phase shift formula: exp(-i * delta_r * k), where:
    % - delta_r = voxel shift * 2 * pi

    RL_new = x * (voxel_shift_RL * 2 * pi) / dimx;
    AP_new = y *(voxel_shift_AP*2*pi)/dimy;
    FH_new = z *(voxel_shift_FH*2*pi)/dimz;

    % Create complex array e^-ix=cos(x)-isin(x)
    phase_shift_complex_RL = complex(cos(RL_new), -sin(RL_new));
    phase_shift_complex_AP = complex(cos(AP_new), -sin(AP_new));
    phase_shift_complex_FH = complex(cos(FH_new), -sin(FH_new));

    % Add the spectrum dimension to enable multiplying
    phase_shift_complex_RL = reshape(phase_shift_complex_RL, [1, dimx, dimy, dimz]);
    phase_shift_complex_AP = reshape(phase_shift_complex_AP, [1, dimx, dimy, dimz]);
    phase_shift_complex_FH = reshape(phase_shift_complex_FH, [1, dimx, dimy, dimz]);

    % Multiply with the k-space data
    k_space_data_shifted = k_space_data .*...
        phase_shift_complex_RL .* phase_shift_complex_AP .* phase_shift_complex_FH;

    spectrum_voxelshift_kspace = k_space_data_shifted;
end
```

```
function [spectrum_voxelshift_interpolation] = VoxelShiftInterpolation(spectral_data,
    voxel_shift_RL, voxel_shift_AP, voxel_shift_FH, interpolation_technique)
   %% VoxelShiftInterpolation - Apply voxel shift using interpolation
    % This function applies a voxel shift to spectral data using interpolation.
    % The shift is applied along three spatial directions:
    % - Right-Left (RL)
    % - Anterior-Posterior (AP)
    % - Feet-Head (FH)
    %
    % Author: Hilde Roording
    %
    % Inputs:
    % - spectral_data: 4D array of spectral data (spectral dimension x spatial dimensions)
    % - voxel_shift_RL: Shift in voxel units along the Right-Left direction
    % - voxel_shift_AP: Shift in voxel units along the Anterior-Posterior direction
    % - voxel_shift_FH: Shift in voxel units along the Feet-Head direction
    % - interpolation_technique: Interpolation method (e.g., 'linear', 'nearest', 'cubic')
    %
    % Output:
    % - spectrum_voxelshift_interpolation: 4D array with voxel shift applied using
        interpolation

    % Pad data with repeating edge values along each spatial dimension
```

```
    spectral_data = padarray(spectral_data, [0, 1, 1, 1], 'replicate', 'both');  % pad only
        spatial dimensions

    [dimx, dimy, dimz] = size(spectral_data, [2, 3, 4]);

    % Create original voxel position grids
    [RL, AP, FH] = meshgrid( 1:dimy,1:dimx, 1:dimz);  % Grids for x, y, z voxel dimensions


    % Compute new voxel positions after shifting
    RL_new = RL + voxel_shift_RL;
    AP_new = AP + voxel_shift_AP;
    FH_new = FH + voxel_shift_FH;


    shifted_data = zeros(size(spectral_data));

    % Perform interpolation for each spectral point independently
    for i = 1:size(spectral_data, 1)
%          Interpolate for each spectral point
        shifted_data(i, :, :, :) = interp3(RL, AP, FH, double(squeeze(spectral_data(i, :, :,
            :))), RL_new, AP_new, FH_new, interpolation_technique, 0);

    end
    % Remove padding to return to original shape
    shifted_data = shifted_data(:, 2:end-1, 2:end-1, 2:end-1);  % crop padded dimensions

    spectrum_voxelshift_interpolation = shifted_data;

end
```

C

Heatmaps

Heatmaps for the 0.3 voxel shift in Anterior-Posterior (AP), Left-Right (LR), and Feet-Head (FH) direction

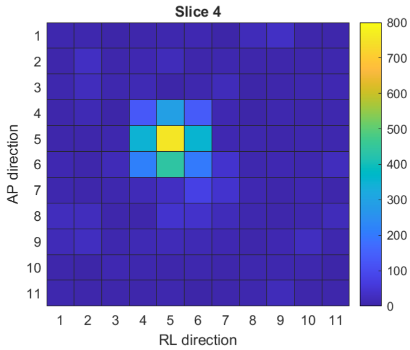

(a) $\mathrm{MRSI}_{\mathrm{ref}}$

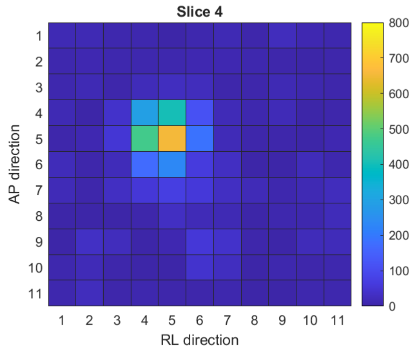

(b) $\mathrm{MRSI}_{\mathrm{Shifted}}$

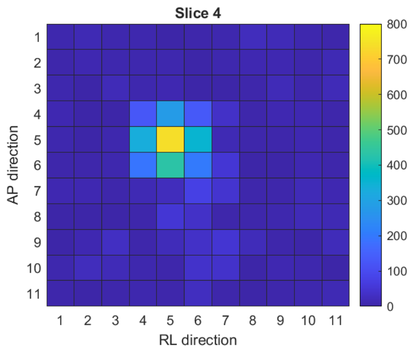

(c) $\mathrm{MRSI}_{\mathrm{Phase\ Shift}}$(-0.3 voxels AP, RL, and FH)

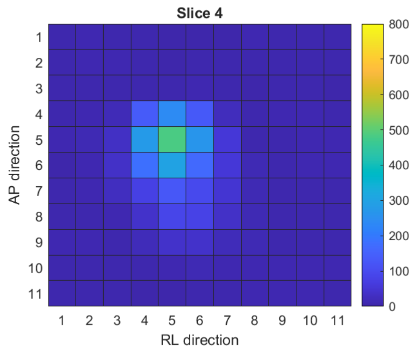

(d) $\mathrm{MRSI}_{\mathrm{interpolated}}$(-0.3 voxels AP, RL, and FH)

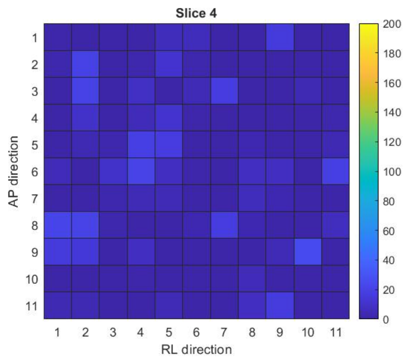

(e) $\mathrm{MRSI}_{\mathrm{Ref}}$ - $\mathrm{MRSI}_{\mathrm{PhaseShift}}$

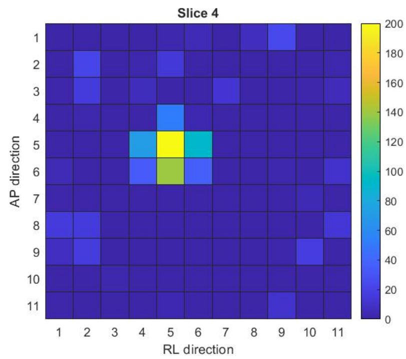

(f) $\mathrm{MRSI}_{\mathrm{Ref}}$ - $\mathrm{MRSI}_{\mathrm{interpolated}}$

Figure C.1: Heatmaps of the area under the curve (AUC) of the signal of inorganic phosphate (Pi) in the phantom experiment. Where C.1a shows the AUC of $\mathrm{MRSI}_{\mathrm{Ref}}$, C.1b shows the AUC of $\mathrm{MRSI}_{\mathrm{Shifted}}$, C.1c shows the AUC of $\mathrm{MRSI}_{\mathrm{Shifted}}$ after phase adjustment in k-space by -0.3 voxels in the Anterior-Posterior (AP), Right-Left (RL), and Feet-Head (FH) directions ($\mathrm{MRSI}_{\mathrm{PhaseShift}}$), C.1d shows the AUC of $\mathrm{MRSI}_{\mathrm{Shifted}}$ after spatially based interpolation by -0.3 in AP, RL, and FH direction ($\mathrm{MRSI}_{\mathrm{interpolated}}$), C.1e and C.1f depict the differences between the shifted AUCs and the $\mathrm{MRSI}_{\mathrm{Ref}}$ for k-space phase adjustment and spatial based interpolation, respectively.

Heatmaps for the 0.1 voxel shift in Anterior-Posterior (AP) direction

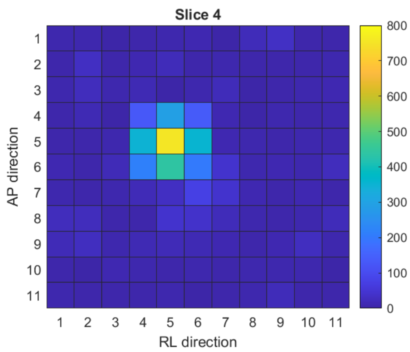

(a) $\mathrm{MRSI_{ref}}$

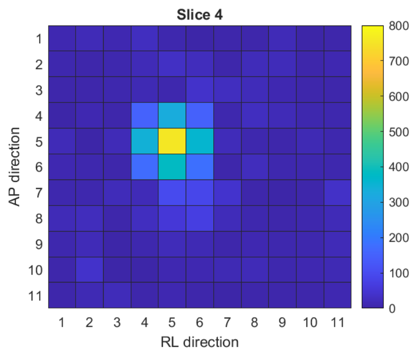

(b) $\mathrm{MRSI_{Shifted}}$

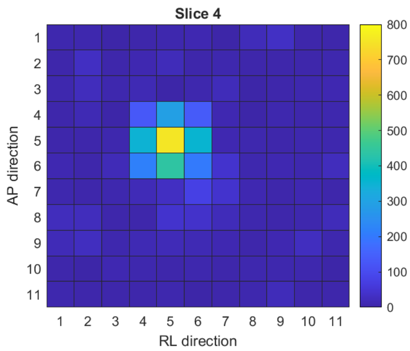

(c) $\mathrm{MRSI_{Phase\ Shift}}$(-0.1 voxels AP)

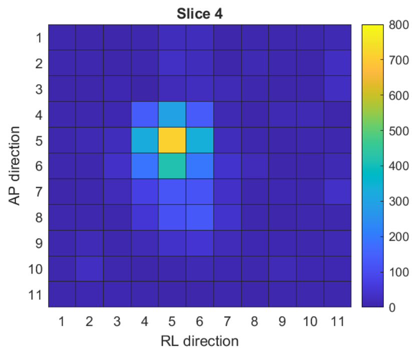

(d) $\mathrm{MRSI_{interpolated}}$(-0.1 voxels AP)

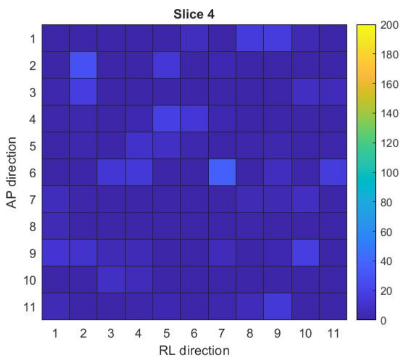

(e) $\mathrm{MRSI_{Ref}}$ - $\mathrm{MRSI_{PhaseShift}}$

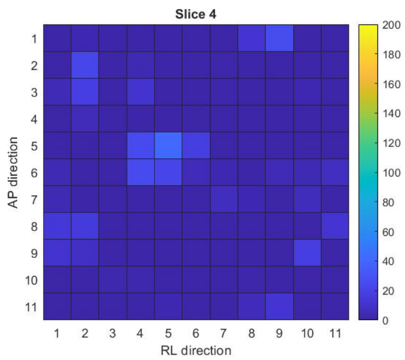

(f) $\mathrm{MRSI_{Ref}}$ - $\mathrm{MRSI_{interpolated}}$

Figure C.2: Heatmaps of the area under the curve (AUC) of the signal of inorganic phosphate (Pi) in the phantom experiment. Where C.2a shows the AUC of $\mathrm{MRSI_{Ref}}$, C.2b shows the AUC of $\mathrm{MRSI_{Shifted}}$, C.2c shows the AUC of $\mathrm{MRSI_{Shifted}}$ after phase adjustment in k-space by -0.1 voxels in the Anterior-Posterior (AP) direction ($\mathrm{MRSI_{PhaseShift}}$), C.2d shows the AUC of $\mathrm{MRSI_{Shifted}}$ after spatially based interpolation by -0.1 in AP direction ($\mathrm{MRSI_{interpolated}}$), C.2e and C.2f depict the differences between the shifted AUCs and the $\mathrm{MRSI_{Ref}}$ for k-space phase adjustment and spatial based interpolation, respectively.

Heatmaps for the 0.3 voxel shift in Left-Right (LR) direction

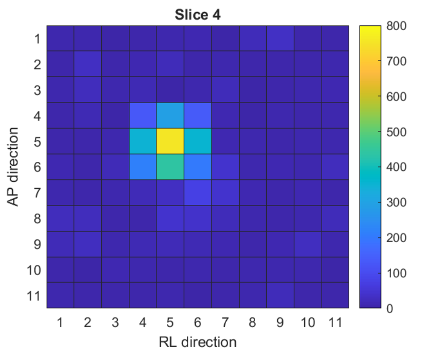

(a) $\mathrm{MRSI}_{\mathrm{ref}}$

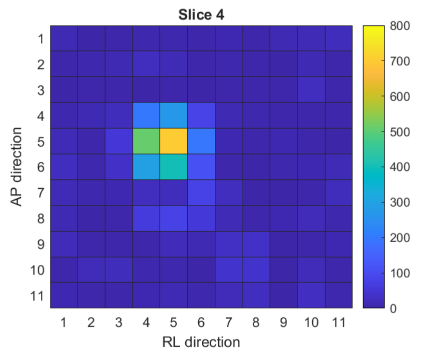

(b) $\mathrm{MRSI}_{\mathrm{Shifted}}$

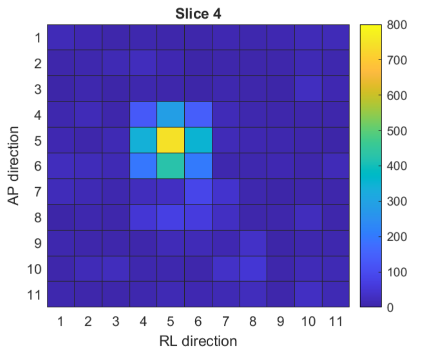

(c) $\mathrm{MRSI}_{\mathrm{Phase\ Shift}}$(-0.3 voxels LR)

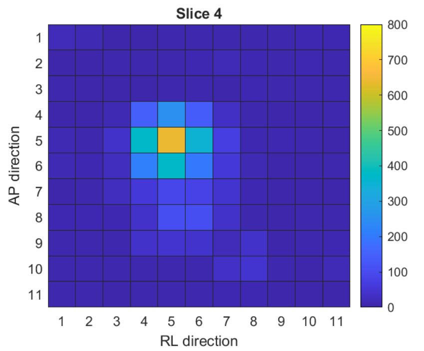

(d) $\mathrm{MRSI}_{\mathrm{interpolated}}$(-0.3 voxels LR)

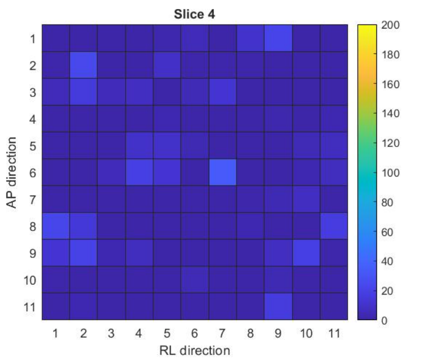

(e) $\mathrm{MRSI}_{\mathrm{Ref}}$ - $\mathrm{MRSI}_{\mathrm{PhaseShift}}$

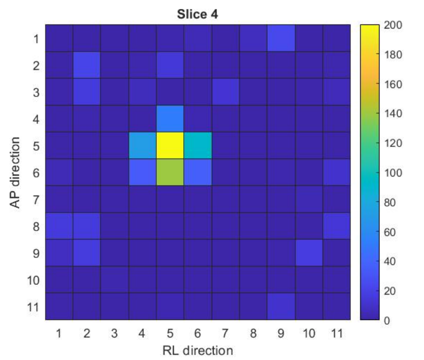

(f) $\mathrm{MRSI}_{\mathrm{Ref}}$ - $\mathrm{MRSI}_{\mathrm{interpolated}}$

Figure C.3: Heatmaps of the area under the curve (AUC) of the signal of inorganic phosphate (Pi) in the phantom experiment. Where C.3a shows the AUC of $\mathrm{MRSI}_{\mathrm{Ref}}$, C.3b shows the AUC of $\mathrm{MRSI}_{\mathrm{Shifted}}$, C.3c shows the AUC of $\mathrm{MRSI}_{\mathrm{Shifted}}$ after phase adjustment in k-space by -0.3 voxels in the Left-Right (LR) direction ($\mathrm{MRSI}_{\mathrm{PhaseShift}}$), C.3d shows the AUC of $\mathrm{MRSI}_{\mathrm{Shifted}}$ after spatially based interpolation by -0.3 in LR direction ($\mathrm{MRSI}_{\mathrm{interpolated}}$), C.3e and C.3f depict the differences between the shifted AUCs and the $\mathrm{MRSI}_{\mathrm{Ref}}$ for k-space phase adjustment and spatial based interpolation, respectively.

Heatmaps for the 0.5 voxel shift in Feet-Head (FH) direction

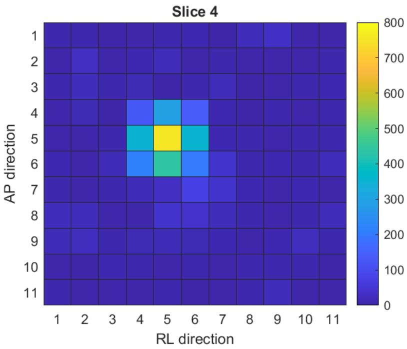

(a) $\mathrm{MRSI_{ref}}$

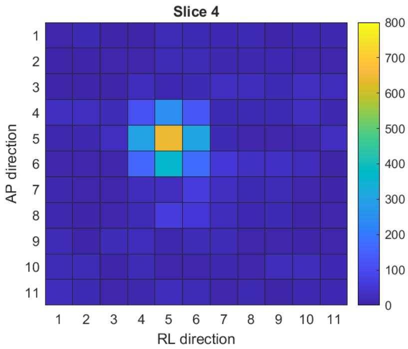

(b) $\mathrm{MRSI_{Shifted}}$

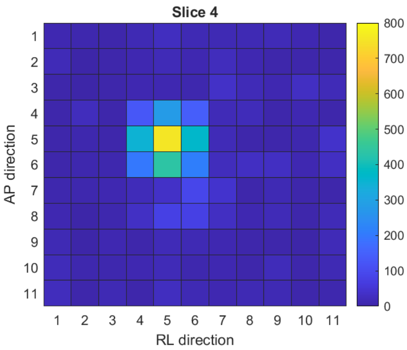

(c) $\mathrm{MRSI_{Phase\ Shift}}$(-0.5 voxels FH)

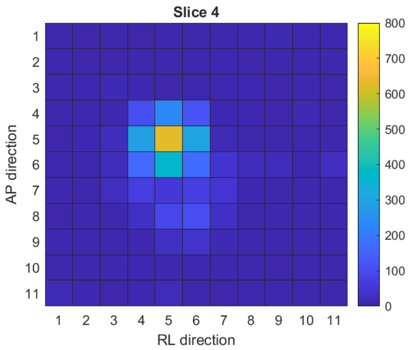

(d) $\mathrm{MRSI_{interpolated}}$(-0.5 voxels FH)

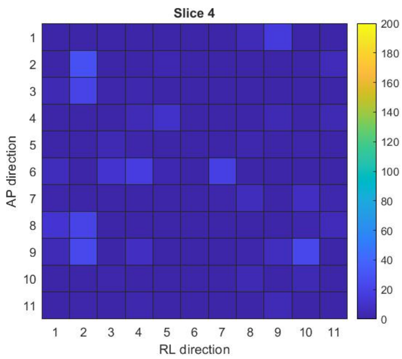

(e) $\mathrm{MRSI_{Ref}}$ - $\mathrm{MRSI_{PhaseShift}}$

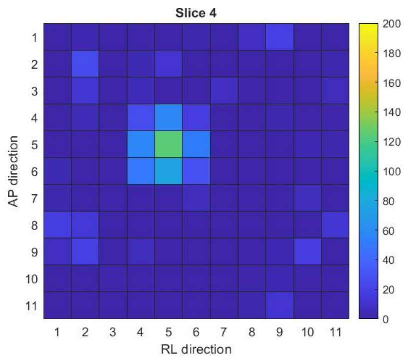

(f) $\mathrm{MRSI_{Ref}}$ - $\mathrm{MRSI_{interpolated}}$

Figure C.4: Heatmaps of the area under the curve (AUC) of the signal of inorganic phosphate (Pi) in the phantom experiment. Where C.4a shows the AUC of $\mathrm{MRSI_{Ref}}$, C.4b shows the AUC of $\mathrm{MRSI_{Shifted}}$, C.4c shows the AUC of $\mathrm{MRSI_{Shifted}}$ after phase adjustment in k-space by -0.5 voxels in the Feet-Head (FH) direction ($\mathrm{MRSI_{PhaseShift}}$), C.4d shows the AUC of $\mathrm{MRSI_{Shifted}}$ after spatially based interpolation by -0.5 in FH direction ($\mathrm{MRSI_{interpolated}}$), C.4e and C.4f depict the differences between the shifted AUCs and the $\mathrm{MRSI_{Ref}}$ for k-space phase adjustment and spatial based interpolation, respectively.

Heatmaps for the 0.3 voxel shift in Anterior-Posterior (AP), Left-Right (LR), and Feet-Head (FH) direction for voxel size $10 \times 10 \times 10$ mm^3

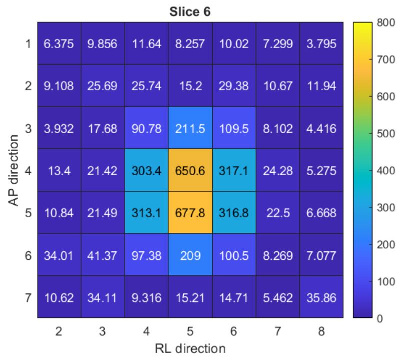

(a) $\mathrm{MRSI}_{\mathrm{ref}}$

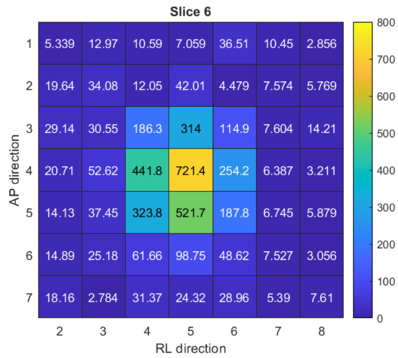

(b) $\mathrm{MRSI}_{\mathrm{Shifted}}$

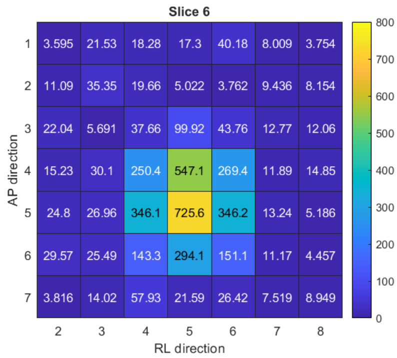

(c) $\mathrm{MRSI}_{\mathrm{Phase\ Shift}}$(-0.3 voxels AP, RL, and FH)

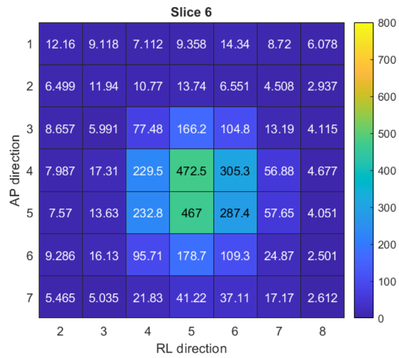

(d) $\mathrm{MRSI}_{\mathrm{interpolated}}$(-0.3 voxels AP, RL, and FH)

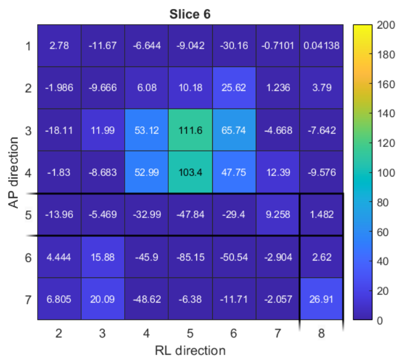

(e) $\mathrm{MRSI}_{\mathrm{Ref}}$ - $\mathrm{MRSI}_{\mathrm{PhaseShift}}$

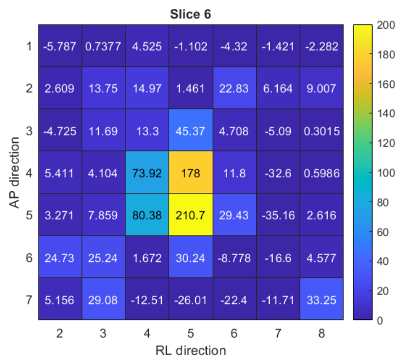

(f) $\mathrm{MRSI}_{\mathrm{Ref}}$ - $\mathrm{MRSI}_{\mathrm{interpolated}}$

Figure C.5: Heatmaps of the area under the curve (AUC) of the signal of inorganic phosphate (Pi) in the phantom experiment with the voxel size $10 \times 10 \times 10$ mm^3. Where C.5a shows the AUC of $\mathrm{MRSI}_{\mathrm{Ref}}$, C.5b shows the AUC of $\mathrm{MRSI}_{\mathrm{Shifted}}$, C.5c shows the AUC of $\mathrm{MRSI}_{\mathrm{Shifted}}$ after phase adjustment in k-space by -0.3 voxels in the Anterior-Posterior (AP), Right-Left (RL), and Feet-Head (FH) directions ($\mathrm{MRSI}_{\mathrm{PhaseShift}}$), C.5d shows the AUC of $\mathrm{MRSI}_{\mathrm{Shifted}}$ after spatially based interpolation by -0.3 in AP, RL, and FH direction ($\mathrm{MRSI}_{\mathrm{interpolated}}$), C.5e and C.5f depict the differences between the shifted AUCs and the $\mathrm{MRSI}_{\mathrm{Ref}}$ for k-space phase adjustment and spatial based interpolation, respectively.

D

^{31}P-MRSI code for grid calculations

```
%% MRI Data Processing and Tumor Volume Analysis
% This script processes MRI and MRSI data for voxel alignment and tumor volume estimation.
% It loads patient data, aligns imaging modalities, visualizes voxel grids, and computes tumor coverage.
%
% Author: Hilde Roording
%
% Key Steps:
% - Load subject-specific MRI and MRSI data from predefined directories.
% - Align FLAIR and SmartBrain images, ensuring correct spatial dimensions.
% - Generate and visualize voxel grids before and after displacement.
% - Determine voxel-wise displacement using manual selection and correction.
% - Compute the percentage of tumor coverage in each voxel before and after alignment.
% - Save results, including displacement values and tumor volume percentages.

close all
clear all
clc
addpath(genpath('H:\MATLAB\FID-A\FID-A-master'))
addpath(genpath('Z:\F_DataAnalysis\ImageRegsitration_Dominique'))
addpath(genpath('H:\MATLAB\MRS_MRI_libs-master'))% FID-A toolbox
addpath(genpath('W:\F_DataAnalysis'))
addpath(genpath('W:\G_Output'))

%% Subject info
% subj ID, timepoint, DICOM smartbrain sagittal, spar file original data, slice with tumor

% subject_info={'MITCH_224', 'Baseline', 'SBsag','RECREATED_DBIEX_7_2_raw_act',5;};

plotdata.subject_info=subject_info;

MITCH_dir = '\\ds\data\BEELD\Wetenschap\MITCH\'
% MITCH_dir = 'H:\';

pp=1; % If only one patient is present in subject_info

% Set paths smart brain, FLAIR registered to smart brain and spar file
dirFLAIR_final=[MITCH_dir subject_info{pp,1} '\' subject_info{pp,2} '\Classic\Results\x.Registration\reg_FLAIR_SB\x.Transformix_FLAIR'];

dirMask_final=[MITCH_dir subject_info{pp,1} '\' subject_info{pp,2} '\Classic\Results\x.Registration\reg_FLAIR_SB\x.Transformix_mask'];
dirMRS=[MITCH_dir, subject_info{pp,1},'\', subject_info{pp,2}, '\Classic\Data'];
path_SB = [dirMRS '\DICOM\' subject_info{pp,3}];
spar_info=mrs_readSPAR([dirMRS '\' subject_info{pp,4}]);
% [spar_name,spar_path] = uigetfile({'*.spar'},'Select a file',dirMRS);
% spar_info=mrs_readSPAR([spar_path '\' spar_name]);

% Directory to save images
```

```
plotdata.save_dir = [MITCH_dir subject_info{pp,1},'\' subject_info{pp,2} '\Plots_Grid\Grid_BeforeShift_HR_202501'];
mkdir(char(plotdata.save_dir));
plotdata.save_dir_afterShift=[MITCH_dir subject_info{pp,1},'\' subject_info{pp,2} '\Plots_Grid\Grid_AfterShift_HR_202501'];
mkdir(char(plotdata.save_dir_afterShift));


% Check if the spar file is the right one it should be-> scan_id : 3D CSI FID FA 11p4 20x20x20 NSA 28_MITCH
if spar_info.averages~=28
    error('Warning!␣This␣is␣not␣correct␣.spar␣file;␣stop')
end

% Load in FLAIR and MASK, if no mask available create a mask of zeros
[rFLAIR, resFLAIR] = ReadRawImage([dirFLAIR_final, '\FLAIR_reg_SB_PV.mhd']);
[mask, mask_res] = ReadRawImage([dirMask_final, '\Tumor_reg_SB_PV.mhd']);
% mask=zeros(size(rFLAIR));


info_SB = dicominfo([dirMRS, '\DICOM\', subject_info{pp,3}]);

if ~isequal(info_SB.PulseSequenceName, 'T1TFE')==1
    error('Warning!␣This␣is␣not␣SmartBrain␣7T;␣stop')
end

disp(['Size␣of␣rFLAIR:␣', mat2str(size(rFLAIR))]);
disp(['Size␣of␣Mask:␣', mat2str(size(mask))]);

if ~isequal(size(rFLAIR), size(mask))
    error('Warning!␣The␣FLAIR␣and␣Mask␣do␣not␣have␣the␣same␣size');
end

% % Visualize all slices
% figure(); subplot(1,2,1); montage(rFLAIR,'DisplayRange',[]);
% subplot(1,2,2); montage(mask,'DisplayRange',[]);

rImage=rFLAIR;
plotdata.resImage=resFLAIR;
% The spar could be either type 1 or 2 the patient data is type 1 the
% phantom data is type 2



%% Code for when everything is read in
% Extract offcenter smart brain
pixelspac_SB = info_SB.PerFrameFunctionalGroupsSequence.Item_1.PixelMeasuresSequence.Item_1.PixelSpacing;
thickness_SB = info_SB.SpacingBetweenSlices;
spacing_SB = [pixelspac_SB(1) thickness_SB pixelspac_SB(2)];

SB_AP_off = info_SB.Private_2001_105f.Item_1.Private_2005_1078;
SB_RL_off = info_SB.Private_2001_105f.Item_1.Private_2005_107a;
SB_FH_off = info_SB.Private_2001_105f.Item_1.Private_2005_1079;

sb_rows=info_SB.Rows;
sb_columns=info_SB.NumberOfFrames;

% Add and remove zeros from the FLAIR to make sure the dimensions are
% correct
if (size(rFLAIR,1) ~= sb_rows) && (size(rFLAIR,2) ~= sb_columns)

    rImage = padarray(rImage,[0 round((sb_columns*spacing_SB(2)/resFLAIR(2)))-size(rImage,2) 0],0,'post');
    plotdata.rImage = rImage(1:(sb_rows*spacing_SB(1)/resFLAIR(1)), :,:);

    rMask = padarray(mask,[0 round((sb_columns*spacing_SB(2)/mask_res(2)))-size(mask,2) 0],0,'post');
    plotdata.mask = rMask(1:(sb_rows*spacing_SB(1)/mask_res(1)), :,:);
    plotdata.rImage = padarray(plotdata.rImage,[20 20 0],0,'both');
    plotdata.mask = padarray(plotdata.mask,[20 20 0],0,'both');
```

```
else
    disp('The FLAIR has the same size as the SmartBrain')
    plotdata.rImage = padarray(rFLAIR,[20 20 0],0,'both');
    plotdata.mask = padarray(mask,[20 20 0],0,'both');
end

%% Add offcenter information !!!!!
% Define the spar info type when loading in the images. Patient data is

    plotdata.offcAP = -round(SB_AP_off - spar_info.offcentre(2));
    plotdata.APpix = plotdata.offcAP/plotdata.resImage(1);


    plotdata.offcRL = -round(SB_RL_off - spar_info.offcentre(1));
    plotdata.RLpix = plotdata.offcRL/plotdata.resImage(2);

    plotdata.offcFH = round(SB_FH_off - spar_info.offcentre(3));
    plotdata.FHpix = plotdata.offcFH/plotdata.resImage(3);


%% Calculate size of the grid
plotdata.inputCSI = [11 11 9];
[plotdata.AP, plotdata.RL, plotdata.FH] = size(plotdata.rImage);

% The grid is centered on the image and has dimentions 20mm*resolution
% of the image. The image field of view (FOV) is larger than the grid FOV.
% The Halfdif is the distance to the grid as seen from the image.
% Halfdif=(FOV-FOV_GRID)/2
plotdata.APhalfdif = round((plotdata.AP-((plotdata.inputCSI(1)*20)/plotdata.resImage(1)))/2);
plotdata.RLhalfdif = round((plotdata.RL-((plotdata.inputCSI(2)*20)/plotdata.resImage(2)))/2);
plotdata.FHhalfdif = round((plotdata.FH-((plotdata.inputCSI(3)*20)/plotdata.resImage(3)))/2);

% Z halfdif important for what slices of the MRI are displayed for grid slices
plotdata.VoxFH = round(plotdata.FHhalfdif-plotdata.FHpix:((plotdata.FH-(2*plotdata.FHhalfdif))/plotdata.inputCSI(3)):plotdata.FH(end)-plotdata.FHhalfdif-plotdata.FHpix);
plotdata.VoxRL = round(plotdata.RLhalfdif-plotdata.RLpix:((plotdata.RL-(2*plotdata.RLhalfdif))/plotdata.inputCSI(2)):plotdata.RL(end)-plotdata.RLhalfdif-plotdata.RLpix);

% Initialize with no diplacement
Displacement.AP_relative=0;
Displacement.RL_relative=0;
Displacement.FH_relative=0;

% Make the sagittal image and mask by permuting, rotating and flipping
sag_trans_new=permute(plotdata.rImage, [3, 1, 2]);
sag_intermediate = rot90(sag_trans_new, 2);
plotdata.rImageSag = flip(sag_intermediate, 2);

mask_trans_new= permute(plotdata.mask, [3, 1, 2]);
mask_intermediate = rot90(mask_trans_new, 2);
plotdata.maskSag = flip(mask_intermediate, 2);

mydlg = warndlg('press "CTRL+C" in command window, do the visualization manually', 'A Warning Dialog');
waitfor(mydlg);

disp('press "CTRL+C" keys in the Command Window');
pause

%% Visualization
% Define before shift as 1 and after shift as 2 to make sure the images are
% saved in the right folder
no_saving= 0;
before_shift=1;
after_shift=2;

% Choose before_shift to save images in the folder defined at the beginning
saving_choice=no_saving;

% Plot middle slice of the FLAIR for each CSI slice
k_full_cor=1:plotdata.inputCSI(3);
```

```
plot79=PlotGridHR(plotdata,Displacement, k_full_cor,saving_choice);
k_full_sag=1:plotdata.inputCSI(2);
plot167=PlotGridSagHR(plotdata,Displacement, k_full_sag,saving_choice);

% Choose an RL slice on the sagittal image where you want to shift in AP-FH direction
RL_slice=6;
plot300=PlotGridSagHR(plotdata,Displacement, RL_slice,no_saving);

%Choose an FH slice where you want to shift the coronal image in AP-RL direction.
FH_slice=4;
plot7=PlotGridHR(plotdata,Displacement, FH_slice,no_saving);

% Choose a slice where you want to shift in AP-FH direction
q=1:9;
plot489=PlotGridAllSlicesHR(plotdata,Displacement,q,saving_choice);
close all

%% FH-AP displacement !!First select appropriate RL-slice!!
Displacement = FindDisplacementSagHR(plotdata,Displacement,RL_slice);
plot300=PlotGridSagHR(plotdata,Displacement, RL_slice,no_saving);


%% AP-RL displacement !!First select appropriate FH-slice!!
% First plot all slices of the coronal plane of the slices with tumor as
% visualized with the images made above:
Displacement = FindDisplacementHR(plotdata,Displacement,FH_slice);
plot796=PlotGridHR(plotdata,Displacement, FH_slice,no_saving);

%% Check the allignment and if neccesary repeat code
t=5;
plot156=PlotGridAllSlicesHR(plotdata,Displacement,t,no_saving);


%% Calculate the percentage tumor in a voxel
Displacement_zeros.AP_relative=0;
Displacement_zeros.RL_relative=0;
Displacement_zeros.FH_relative=0;

PercentageTumor_noDisplacement=PercentageTumorInVoxel(plotdata,Displacement_zeros, FH_slice);
PercentageTumor=PercentageTumorInVoxel(plotdata,Displacement, FH_slice);

Results=Displacement;
Results.PercentageTumor_noDisplacement=PercentageTumor_noDisplacement;
Results.PercentageTumor=PercentageTumor;

%% Saving all the shifted images, displacement and tumor volume
cd([plotdata.save_dir_afterShift]);
save('Results.mat','Results')

saving_choice=after_shift;
plot79=PlotGridHR(plotdata,Displacement, k_full_cor,saving_choice);
plot167=PlotGridSagHR(plotdata,Displacement, k_full_sag,saving_choice);
plot156=PlotGridAllSlicesHR(plotdata,Displacement,q,saving_choice);
close all
```